

AIX-MARSEILLE UNIVERSITÉ

Ecole doctorale de physique et sciences de la matière

THÈSE

Présentée pour l'obtention du grade de

DOCTEUR D'AIX-MARSEILLE UNIVERSITÉ

Spécialité: Matière condensée et Nanoscience

**Synthèse de nouveaux nanomatériaux par ablation
laser ultra-brève en milieu liquide pour des applications
biomédicales**

Ksenia MAXIMOVA

Soutenue le 15 décembre 2014 à Marseille devant le jury composé de

Dr. Tatiana ITINA, Université Jean Monnet, Rapporteur
Dr. Vladimir LYSENKO, Université Claude Bernard Lyon I, Rapporteur
Dr. Mireille BLANCHARD-DESCE, Université Bordeaux I, Examineur
Prof. Diane BRAGUER, Aix-Marseille Université, Examineur
Dr. Marc SENTIS, Aix-Marseille Université, Examineur
Dr. Michel VAULTIER, Université Bordeaux I, Examineur
Dr. Andrei KABASHIN, Aix-Marseille Université, Directeur de thèse

Résumé

Grâce aux nombreuses propriétés optiques, chimiques, et aussi magnétiques, les nanoparticules inorganiques sont récemment devenues extraordinairement populaires pour une grande variété d'applications. En particulier, en raison des effets associés à l'excitation d'oscillation d'électrons libres (plasmons), les nanostructures d'or sont à présent largement utilisées pour l'imagerie biologique et la thérapie, les biosensors ultra-sensibles, la diffusion Raman exaltée par effet de surface (SERS), la nanoélectronique, le photovoltaïque, et beaucoup d'autres applications. Malgré le fait que l'or massif ne possède pas de propriétés catalytiques, les nanoparticules d'or se révèlent être d'efficace catalyseurs d'oxydation de monoxyde de carbone à basse température.

D'autres nanostructures telles que les nanoparticules de silicium (Si) possèdent de remarquables propriétés. Ces particules de semi-conducteurs, ayant la taille inférieure à 10 nm, montrent d'important effets quantiques, ce qui leur valurent le nom de boîtes quantiques. En particulier, la fluorescence de ces nanoparticules est liée à ces effets. Les nanoparticules de Si possèdent les mêmes propriétés optiques que les boîtes quantiques « classiques » (notamment CdSe, CdTe, ZnS), mais en plus grâce à l'absence de métaux lourds dans leur composition elles sont biocompatibles. Elles ont la capacité de se décomposer dans les organismes vivants jusqu'à l'acide orthosilicique ($\text{Si}(\text{OH})_4$) qui peut être facilement excrété du corps. Ainsi les nanomatériaux à base de Si sont très prometteurs pour la bioimagerie, l'administration de médicaments et les thérapies photo-induites (thérapie photodynamique et photothermique).

Le problème majeur de l'utilisation de nanoparticules inorganiques est leur pureté. Les méthodes de synthèse chimiques généralement utilisées laissent une contamination des nanoparticules avec des produits de départ n'ayant pas réagi, de sous-produits, d'ions et d'agents tensioactifs, compliquant leurs utilisation leurs application. A titre d'exemple, les agents tensioactifs et les ions peuvent induire une toxicité secondaire de matériaux à la base non-toxiques. La présence d'une contamination sur la surface des nanoparticules d'or risque de réduire leur activité catalytique et d'affecter les signaux Raman par de forts signaux de bruit.

Dans ce contexte l'objectif de notre travail est le développement d'une procédure de synthèse pures de nanoparticules d'or et de silicium par ablation laser ultra-brève. L'ablation laser dans le

milieu liquide émerge comme une alternative « écologique » aux moyens de synthèses chimiques, permettant la fabrication de nanomatériaux dans un environnement pure et contrôlé. Cette technique est basée sur l'irradiation avec un laser impulsif d'une cible immergée dans un liquide. Le matériau est ablaté sous forme de clusters qui en fondant forment des nanoparticules. Généralement l'irradiation avec des impulsions lasers « longues » (nanoseconde, microseconde) mène à la génération de nanoparticules partiellement agrégées, dont les tailles sont largement dispersées et difficiles à contrôler sans usage additionnel de ligands. L'utilisation d'impulsions « ultra-courtes » (femtoseconde) permet de réduire la dispersion de taille et de proposer un contrôle des caractéristiques des particules produites.

Pour perfectionner la distribution des tailles et obtenir un contrôle plus ample des propriétés des nanoparticules, la fragmentation laser de colloïdes déjà formés a été proposée. Cette méthode implique l'irradiation laser de micro- et nanoparticules suspendues dans une solution. Elle profite de la géométrie d'ablation dans le volume, qui permet d'avoir des conditions de formation de particules plus homogènes par rapport à l'ablation d'une cible solide.

Dans ce travail nous combinons les avantages de l'utilisation d'impulsions ultra-courtes avec la fragmentation laser. De plus, l'interaction entre les impulsions femtosecondes et le liquide provoque des effets non-linéaires, notamment la génération d'un supercontinuum de lumière blanche. Par conséquent, le spectre de l'impulsion se retrouve considérablement élargi et assure l'efficacité de l'absorption de l'énergie de l'impulsion par les particules. La lumière blanche n'est alors pas localisée dans le point focal ce qui crée des conditions plus uniformes pour la fragmentation des particules.

Les processus de génération des nanoparticules par ablation et de fragmentation laser dans le liquide sont très complexes et beaucoup de paramètres expérimentaux peuvent influencer la formation des particules et leur caractéristiques. Dans ce travail nous étudions l'effet de certains d'entre eux afin de permettre le contrôle de la taille et de la composition des nanoparticules.

Pour la synthèse des nanoparticules d'or, nous étudions une approche composée de deux étapes : l'ablation préliminaire d'une cible solide suivie par la fragmentation des colloïdes obtenus. En contrôlant l'énergie de l'impulsion à l'étape de la fragmentation, nous pouvons obtenir des nanoparticules d'or avec une taille moyenne variable entre 7 et 50 nm et une distribution des tailles étroite. De plus, cette méthode nous permet de fabriquer des nanoparticules d'alliages bimétalliques et générer des complexes d'or avec des polymères et des oligosaccharides.

Nous développons une nouvelle méthode de synthèse de nanoparticules à base de Si constituée de la fragmentation par laser femtoseconde des microparticules de Si préalablement broyées mécaniquement et dispersées dans l'eau. En variant différents paramètres, nous pouvons contrôler

la taille et la composition de nanoparticules obtenues. Notamment l'alternance de la concentration de microparticules initiale nous permet de maîtriser la taille des nanoparticules et de la varier entre 1–2 et 20–25 nm. Le changement de pH des solutions nous permet aussi de contrôler finement la taille de celles-ci. En outre, en effectuant la fragmentation en conditions ambiantes ou désaérées, nous pouvons modifier l'épaisseur et la composition de la couche d'oxyde sur la surface des nanoparticules.

Pour finir, nous démontrons le potentiel des nanoparticules synthétisées selon les méthodes établies au cours de ce travail pour les applications optiques, catalytiques et biomédicales. En particulier, grâce à la propreté des nanoparticules d'or et d'alliage or-palladium fabriquées par l'ablation laser, leur activités catalytiques sont augmentées par rapport aux nanoparticules produites par voie chimique. Le SERS et l'extinction de fluorescence sur la surface des nanoparticules d'or sont améliorés grâce à leur non-contamination. De plus, la surface propre des nanoparticules fabriquées par laser permet de les modifier facilement et de former des complexes avec les agents tensioactifs photosensibles menant à la création de structures plasmoniques contrôlable par la lumière. Nous montrons que les nanoparticules d'or et de silicium synthétisées par l'ablation laser sont non-toxiques pour les cellules humaines et peuvent être utilisées pour des applications biomédicales, telles que les vecteurs de médicaments et les sensibilisants pour la thérapie hyperthermique induite par les fréquences radio.

Contents

Introduction	1
1 Main mechanisms of nanoparticles generation by laser ablation	9
1.1 Introduction	10
1.2 Laser ablation from a solid target	10
1.2.1 Laser beam propagation through the liquid	11
1.2.2 Laser pulse absorption and energy deposition	11
1.2.3 Ejection of ablated material	14
1.2.4 Expansion and quenching of the plasma plume, nucleation and cavitation bubble formation	18
1.2.5 Expansion and collapse of the cavitation bubble	19
1.2.6 Growth and agglomeration of the nanoparticles	20
1.3 Laser irradiation of colloidal solutions	20
1.3.1 Propagation of the laser pulse in a liquid medium	20
1.3.1.1 Optical breakdown	21
1.3.1.2 Filamentation and supercontinuum generation	22
1.3.2 Interaction of femtosecond laser radiation with colloidal particles	24
1.3.2.1 Photothermal mechanism	24
1.3.2.2 Coulomb explosion	25
1.3.2.3 Near-field ablation	28
1.3.2.4 Other processes	29
1.4 Conclusion	30
2 Synthesis of the gold nanoparticles by laser ablation	31
2.1 Introduction	32
2.2 Context	32
2.2.1 Influence of physical parameters	32
2.2.1.1 Pumping laser wavelength	32
2.2.1.2 Laser energy	33
2.2.1.3 Pulse duration	34
2.2.1.4 Spot size and focusing conditions	36
2.2.1.5 Repetition rate and number of pulses	37
2.2.1.6 External temperature and pressure	38
2.2.2 Influence of chemical parameters	38
2.2.2.1 Solvent	38
2.2.2.2 Presence of the solutes	39
2.2.3 Laser fragmentation	42
2.3 Materials and methods	46
2.3.1 Materials	46
2.3.2 Ablation from the bulk target	46
2.3.3 Laser fragmentation and alloying	47

2.3.4	Measurements	47
2.4	Laser synthesis of gold nanoparticles	48
2.4.1	Ablation from a bulk target	48
2.4.2	Laser fragmentation	49
2.4.2.1	Size and structure of the nanoparticles prepared after the laser fragmentation	49
2.4.2.2	Effects accompanying the fragmentation	52
2.4.2.3	Possible mechanisms of femtosecond laser fragmentation	56
2.4.3	Capped gold nanoparticles	59
2.4.3.1	PEG- and dextran-covered gold nanoparticles	59
2.4.3.2	Cyclodextrin-covered gold nanoparticles	61
2.4.4	Alloy nanoparticles	65
2.4.5	Optical properties	67
2.5	Conclusion	70
3	Laser synthesis of Si nanoparticles	71
3.1	Introduction	72
3.2	Context	72
3.3	Materials and methods	74
3.3.1	Synthesis of Si nanoparticles	74
3.3.2	Measurements	75
3.4	Synthesis of Si-based nanoparticles by the fragmentation of Si colloids	75
3.4.1	Fragmentation of Si colloids. Influence of the initial particles concentration	75
3.4.2	Influence of the pH	78
3.4.3	Effect of the dissolved oxygen	81
3.4.4	Optical properties	84
3.5	Conclusion	84
4	Applications of the laser-produced nanoparticles	87
4.1	Introduction	88
4.2	Gold nanoparticles for fluorescence quenching and surface-enhanced Raman spectroscopy	88
4.3	Light controlled surface plasmon properties of gold nanoparticles	91
4.4	Gold nanoparticles for biomedical applications	97
4.5	Si nanoparticles for radio-frequency radiation-induced hyperthermia	100
4.6	Au and AuPd nanoparticles as electro-catalyst	104
4.7	Conclusion	108
	Conclusion	111
	Appendix A Plasmonic properties of Au nanoparticles	115
	Bibliography	118
	List of abbreviations	143
	Publications	145

Introduction

The past few decades are marked with a real boom of the nanotechnologies. In general it deals with the creation and exploitation of the materials with structural features between those of atoms and bulk materials, with dimensions typically spanning from sub-nanometer to several hundreds of nanometers. A fascinating aspect of the nanomaterials consists in the size effects. Indeed, materials at the micrometer scale mostly exhibit the same properties as the bulk form; while at the nanometer scale the materials can possess completely different structural, thermodynamic, electronic, spectroscopic, electromagnetic and chemical features. Besides, high surface-to-volume ratio enhances all surface processes. For example, crystals at the nanometer scale have a low melting point (the difference can be as high as 1000 K) and reduced lattice constants, since the number of surface atoms becomes a significant fraction of the total atom number, and the surface energy plays a considerable role in thermal stability [1]. Bulk semiconductors become insulators when the characteristic dimensions are sufficiently small (a couple of nanometers) [2]. Although the bulk gold does not exhibit catalytic activity, Au nanoparticles appear to be an excellent low temperature catalyst [3–5]. Despite the attractive properties of the nanomaterials, their fabrication meets a number of challenges [1], such as:

- Overcoming the large surface energy, a result of enormous surface area and large surface-to-volume ratio;
- Ensuring that all nanomaterials have desired size, narrow size distribution, morphology, crystallinity, chemical composition and microstructure, that altogether result in desired physical properties;
- Making stable nanomaterials and preventing them from coarsening and agglomeration in time.

There are two approaches to the synthesis of the nanomaterials: top-down and bottom-up. Generally, a top-down approach corresponds to the creation of nanoscaled structures with the desired shapes and characteristics starting from larger dimensions and reducing them to the

required values. On the other hand, bottom-up approach seeks to have molecular or atomic components built up into more complex nanoscaled assemblies [6]. Both approaches play an important role in the nanotechnology, but both of them have their own advantages and disadvantages.

One of the well-known and well-studied examples of nanomaterials is the gold nanoparticles. The ancient Chinese and Romans used Au nanoparticles as an inorganic dye to introduce red color into their porcelain and glass thousand years ago. The famous Lycurgus Cup, 4th-century Roman glass cup, which shows a different color depending on how the light is passing through it (Figure 1), contains small fractions of Au and Ag nanoparticles dispersed in the glass that are responsible for this optic effect. The modern scientific evaluation of Au nanoparticles began with Michael Faraday's works in 1850s [7]. The colloidal dispersion, which he has prepared in 1857, was stable for almost a century before it was destroyed during the World War II. The colloidal gold is widely used for medical applications [8]. It was, and is still used for the treatment of arthritis. A number of diseases were diagnosed by the interaction of colloidal gold with spinal fluids obtained from the patient [9].



Figure 1: Lycurgus Cup lit from in front (left) and from behind (right), showing different colors depending on the position of the viewer and the light source. This effect owes its appearance to the presence of the small amount of Au and Ag nanoparticles in the composition of glass. Now exposed in British Museum, London.

Gold nanoparticles owe their unique properties due to the quantum size effect. This effect manifests itself when the de Broglie wavelength of the valence electrons is of the same order than the size of a nanoparticle itself. Free mobile electrons are trapped in “metal boxes” and show characteristic collective oscillations of the electron gas at the surface of the nanoparticles, giving rise to so-called plasmon resonance band near 530 nm for 5–50 nm Au nanoparticles.

The plasmonic properties of Au nanoparticles give rise to their multiple applications. For example, the surface plasmons can offer attractive applications in nano-optics and nano-electronics, *e.g.* as optical circuits below the diffraction limit [10, 11]. Due to their strong light-absorption properties and excellent biocompatibility, Au nanoparticles are important for biomedical applications as contrast agents in diagnostic imaging [12, 13], nanoscale heat sources and sensitizers of light-induced hyperthermia to trigger cancer cell death and tumor remission [14, 15]. Gold nanostructures can also serve as nanoscale devices for improved therapy and diagnostics [16] and as drug-carriers to improve the biodistribution of drugs to diseased organs [17, 18]. Plasmonic nanoparticles are known to drastically enhance local electric field that is used for the surface-enhanced Raman scattering (SERS) spectroscopy, which makes possible ultra-sensitive analysis of various molecules down to single molecule level [19, 20]. Biosensing that exploits the detection of changes of the refractive index around Au nanoparticles is another area of development [21, 22]. Au nanoparticles can also be employed for photovoltaic applications, which imply the conversion of sunlight into electricity. Au nanoparticles can improve the absorption of photovoltaic devices [23] or behave as plasmon-assisted optical antennas [24, 25], where light is concentrated into a subwavelength volume to convert the incident light to amplified electric fields. Finally, gold nanoparticles can be an excellent catalyst for the heterogeneous low-temperature CO and CH₃OH oxidation resulting in the formation of CO₂ [26].

Silicon nanoparticles present another prominent example of an extremely important nanomaterial. Small semiconductor nanoparticles, also called quantum dots, show large size-dependent changes in their fluorescent properties below a radius of a few nm [2]. While molecules have discrete energy level spectra and solids have continuous bands of energy levels, nanoparticles occupy the intermediate position and can be considered either as large molecules or small pieces of solids. Absorption of light in semiconductors promotes an electron to a higher energy level and creates an unoccupied orbital at lower energy (a “hole”), which behaves as a mobile positive charge. When the radius of a wavefunction describing the electron-hole pair (exciton) is larger than the particle size, strong confinement effects can take place. Thus, Si nanoparticles can demonstrate similar behavior as “classical” semiconductor quantum dots (ZnS, CdSe, CdTe) as emitters or photocatalysis agents, but Si nanoparticles have a number of advantages. First of all, they are free of highly toxic heavy metal ions, and are naturally biocompatible [27]. Second, Si and its oxides SiO_x are biodegradable as in biological tissues they are normally decomposed to orthosilicic acid (Si(OH)₄) that is extracted from the body with the urine [28]. Finally, the robust surface chemistry of Si nanoparticles gives a lot of possibilities for their further modification and conjugation [29]. Excellent biocompatibility and biodegradability combined with optical proper-

ties enables the application of Si-based nanomaterials as luminescent labels for bioimaging [30,31] or as carriers in drug vectoring [31,32]. Moreover, Si nanoparticles can act as photosensitizers in photodynamic therapy of cancer [33,34]: electrons and holes created under illumination can react with oxygen on the particle surface and generate reactive oxygen species and/or free radicals yielding the cell apoptosis. Finally, photothermal therapy based on Si nanoparticles relies on the light-induced heating of the nanoparticles that can also induce the cancer cell kill [35,36].

One of the main issues in applications of the nanoparticles is related to their purity. Indeed, conventional chemical methods of synthesis of Au nanoparticles include the reduction of gold precursors in the presence of capping ligands [37,38], but this procedure often leads to a contamination of nanoparticles surface by non-reacted starting reagents, by-products, ions and surfactants [39,40]. Alternative chemical pathways such as template growth [41], electrochemical routes [42], seed-mediated growth [43], *etc.* are also not capable to provide the required purity. In the case of Si nanoparticles, the most popular methods of synthesis include chemical reduction [44] or electrochemical etching [28,34,35,45–47], which also lead to a contamination by by-products. The presence of residual organic and non-organic contaminants complicates many application prospects of chemically synthesized Au and Si nanoparticles. As an example, some products (mostly surfactants [48] and ions [40]) can cause so-called secondary toxicity of *a priori* non-toxic materials, which complicates their biomedical applications. In addition, efficient Si nanoparticles fabrication strategies normally imply a mechanical milling of a porous silicon skeleton, which leads to a wide dispersion of both size and shape of the formed elements, with the mean size reaching several μm [28]. In general, such structural characteristics are not consistent with tasks of delivery *in vivo*. Another prominent example is catalysis using Au nanoparticles: as the catalytic activity critically depends on surface states [49], it can be strongly affected by the presence of surface contaminants. Finally, the surface contamination of plasmonic nanoparticles can strongly decrease the efficiency of SERS: as its signals from target molecules are strongly affected by amplified noise signals from residual contaminants [50].

Laser ablation in liquid ambience has recently emerged as a physical alternative to conventional chemical synthesis [51–57]. This method is based on direct radiation-induced removal (ablation) of material from bulk target yielding the formation of nanoclusters that are released to water and coalesce to form a nanoparticle solution [58]. From the point of view of the nanofabrication, pulsed laser ablation in liquids can be considered as a hybrid technique between the top-down and bottom-up synthetic approaches [59]. This method has a number of advantages:

- Laser ablation can be performed in ultrapure environment, excluding any residual contamination of the nanomaterials [56,57,60]. Such “bare” surface of the nanoparticles can exhibit

different surface chemistry and reactivity compared to conventional colloid material [61];

- It is compatible with 12 principles of “green chemistry” [62], because it does not necessarily require chemicals and does not necessarily produce waste;
- It makes possible one-step coating of the inorganic nanoparticles with organic molecules, either *in situ* (*i.e.* during the synthesis) [63,64] or *ex situ* (*i.e.* after the synthesis) [65,66];
- It is a relatively low cost method, because manual operation and the experimental set-up are minimal, while bulk materials replace chemical precursors and other expensive reagents;
- Laser ablation in liquids is one of the fastest and cleanest routes to produce colloidal solutions of nanomaterials with sizes below 100 nm on the milligram scale [67].

However, the control of the size distribution during laser ablation synthesis is much more complicated, compared to the state of the art wet chemistry methods. First of all, it concerns the control of the nanoparticles size characteristics during the laser-ablative fabrication in the absence of reactive species. Conventional “long pulse” ablation (nanosecond, microsecond, continuous wave) in aqueous or organic environment, which was employed in a large majority of studies, usually leads to the formation of widely size-dispersed, partially agglomerated nanoparticles with the mean size varying from few tens to hundreds of nm [51–55, 68–74]. Size properties of laser-produced nanomaterials can be significantly improved by the employment of ultrashort laser radiation [56, 57, 60, 75–79]. Indeed, due to the minimal laser-plasma plume interaction and the reduction of the heat-affected zone, ultrashort laser irradiation can narrow down the size dispersion and offer an efficient control of the nanoparticle mean size [56, 60].

Laser fragmentation of already formed colloidal solutions offers another opportunity to improve the size distribution of the nanoparticles [80–82]. This approach implies pulsed laser irradiation of the solutions containing preliminary prepared particles. This technique benefits from 3D “volume” geometry, which enables more homogeneous conditions of ablation and particles formation, compared to conventional “planar” geometry of the laser ablation from the bulk target. As a result, more precise size tuning and narrow size distributions can be achieved [82, 83].

The objective of this work is to develop techniques of the controlled laser ablation synthesis of Au- and Si-based nanoparticles. Our approach is based on the ultrafast (femtosecond) pulsed laser ablation of materials. Here we consider both direct geometry of femtosecond laser ablation from a solid target and the “volume” geometry of femtosecond laser fragmentation. The latter configuration implies a preliminary formation of initial particles either by the laser ablation from a solid target (in the case of Au nanoparticles) or mechanical milling (for Si-based nanoparticles), followed by the femtosecond laser fragmentation of the obtained colloids. This method

profits from “fine” ultrashort laser ablation, characterized by a much lower deposited energy and reduced cavitation phenomena, and a broad spectrum of pumping light used for ablation. The later property is due to the generation of white light supercontinuum, which arises in water as a result of non-linear fs laser – liquid interaction. We explore the opportunities of the control of the nanoparticles size characteristics by varying the experimental parameters of the synthesis, namely the pulse energy, the initial particles concentration, the focusing conditions, *etc.* Besides, we introduce a femtosecond laser ablation-based technique of the generation of the bimetallic nanoparticles and complexes of the nanoparticles with polymers and oligosaccharides. We elucidate the influence of the conditions of fragmentation, on the nanoparticles structure and composition. Finally, we consider a series of applications of laser-synthesized Au and Si-based nanomaterials in biomedical and catalysis tasks.

This manuscript is composed of four chapters. First, in order to gain a better insight of the influence of the experimental parameters on the nanoparticles generation and formation, we overview the main physical processes, that occur during the laser ablation of the solid target and colloidal solutions. Here we pay a particular attention to the employment of ultrashort laser pulses, which provide quite different physics of laser-matter interaction compared to “long pulse” ablation. Then we turn to the experimental results on the laser generation of the nanoparticles in liquids. Chapter 2 is devoted to the synthesis of gold nanoparticles. After a brief discussion of the previous studies on the laser-based fabrication of Au nanoparticles and the influence of the experimental parameters on nanoparticles growth we present our results on the synthesis of Au nanoparticles by femtosecond laser ablation and fragmentation. In particular, we demonstrate the efficient size tuning between a few nm and some tens of nm and we discuss the possible mechanisms of the size control. We also show the potential of the two-step femtosecond ablation-fragmentation technique for the synthesis of capped and bimetallic nanoparticles. In Chapter 3 we introduce a laser-ablative methodology for the synthesis of Si-based nanoparticles based on the employment of ultrashort laser ablation from preliminary prepared Si microparticles. We investigate the influence of the conditions of the laser fragmentation on the size and structural characteristics of the formed nanoparticles. In Chapter 4 we demonstrate the potential of the nanoparticles, designed and synthesized according to the techniques developed in this study, for the biomedical, catalytic and optical applications. Finally, a general conclusion of this thesis and the perspectives of the future work are summarized.

Chapter 1

Main mechanisms of nanoparticles generation by laser ablation

Contents

1.1	Introduction	10
1.2	Laser ablation from a solid target	10
1.2.1	Laser beam propagation through the liquid	11
1.2.2	Laser pulse absorption and energy deposition	11
1.2.3	Ejection of ablated material	14
1.2.4	Expansion and quenching of the plasma plume, nucleation and cavitation bubble formation	18
1.2.5	Expansion and collapse of the cavitation bubble	19
1.2.6	Growth and agglomeration of the nanoparticles	20
1.3	Laser irradiation of colloidal solutions	20
1.3.1	Propagation of the laser pulse in a liquid medium	20
1.3.2	Interaction of femtosecond laser radiation with colloidal particles	24
1.4	Conclusion	30

1.1 Introduction

Synthesis of nanoparticles by laser ablation in liquid media is a complex process, which includes the absorption of laser energy, cleavage of the chemical bonds leading to the detachment of the part of a material in a form of ions and hot clusters, which further interact with each others and the surrounding medium forming the nanoparticles. The generation of nanoparticles by laser ablation implies at the same time both the disassembling of a bulk material into sub-nanometer structures and the assembling of smaller clusters into nano-objects. That is why we can consider this technique as a combination of both physical top-down and chemical bottom-up synthetic approaches.

For a successful nanoparticles manipulation and size control, it is essential to understand the mechanisms of the nanoparticles generation under different laser and experimental parameters. In this chapter we will discuss the basics of the processes that occur during the fabrication of the nanoparticles in liquids during both the ablation of a solid target and the pulsed laser irradiation of colloidal solutions.

We will pay special attention to the properties of ultrashort (femtosecond) laser ablation, which implies a fast energy transfer (faster than the thermal relaxation time). Therefore, femtosecond laser radiation cannot be considered as a “thermal source”, as in the case of longer pulse durations. In addition, high intensities of the ultrashort laser irradiation yield the appearance of non-linear phenomena, such as white light supercontinuum generation. The processes discussed in this chapter will mainly concern ultrashort laser ablation.

1.2 Laser ablation from a solid target

Laser ablation from a bulk target in liquid medium includes several consecutive stages. After the absorption of laser radiation by a bulk target, the plasma plume containing the ablated species expands into the surrounding liquid and this process is accompanied by the generation of a shockwave. Then, the expanding plasma plume cools down and releases the energy to the surrounding medium, leading to the formation of a cavitation bubble. The cavitation bubble expands in the liquid and then collapses on the timescale of the order of hundreds of microseconds releasing a huge amount of mechanical energy.

We will review main processes taking place during the laser ablation as a temporal evolution of physicochemical phenomena when a single pulse hits the target. The time $t = 0$ corresponds to the moment when the laser pulse hits the target.

1.2.1 $t < 0$: penetration in the liquid

For effective laser ablation, the energy of a pulse should be delivered to the target and not to the surrounding liquid. The optical breakdown of the liquid should be avoided to reduce losses of the radiation energy [84–86]. Additionally, in the case of femtosecond laser pulses non-linear effects, like self-focusing can be observed at relatively low laser fluences [87, 88]. Besides, certain threshold fluence should not be exceeded in order to avoid the triggering of multiphoton absorption in the liquid [89].

Ideally, the surrounding medium must be transparent for the laser wavelength, which is not always feasible. For instance, water has certain absorption at 1025 nm, but the energy absorbed by the solvent is several orders of magnitude weaker compared to the energy delivered to the target. When already formed nanoparticles and some solutes are present, the absorption and scattering of the surrounding medium can be significant, and the energy delivered to the target can be significantly reduced [59].

1.2.2 From $t = 0$ to 10^{-12} s: laser pulse absorption and energy deposition

Electromagnetic radiation can interact only with electrons of the material, because much heavier nuclei cannot respond to high light frequencies. Core electrons have too high binding energy compared to energies provided by visible and near-infrared light (NIR). Therefore, core electrons interact weakly with the electromagnetic wave below the resonance, and only free electrons can be responsible for the absorption of laser energy. When a laser beam hits the surface of a target, the charge carriers absorb laser energy through the inverse Bremsstrahlung effect. While the metals have free electrons (Fermi electron gas) naturally at ambient conditions, semiconductors have them only in the valence band (under normal conditions). Therefore, the origin of charge carriers responsible for the absorption of the laser energy is different for semiconductors and metals, and the scenario of light absorption is different as well.

In the non-excited state, semiconductors have electrons only in the valence band (where the electrons are “bond”) and the conduction band (where electrons are free as in metals) is empty. The absorption of laser energy induces the transition of an electron from the valence to the conductive band. Besides, depending on the resonant frequency of the electromagnetic irradiation, this transition can occur within one band (intraband) or within different bands (interband). The interband transitions can also be of two types: direct and indirect. When an incident photon with an energy equal or higher than the material band gap (3.4 eV for Si that corresponds to wavelengths of ~ 360 nm and shorter) excites an electron and transfers it directly to conduction band, this process is known as the direct transition. At non-zero temperature

there is a number of phonons that can mediate the interaction between a photon and an electron, lowering the energy required for the electron transition (down to 1.1 eV for Si corresponding to wavelengths of ~ 1130 nm). This process is referred as the indirect transition. As the indirect transition in crystalline silicon requires a simultaneous annihilation of a photon and a phonon, its probability is much lower than for the direct transition. Therefore, the absorption of the photons with energies below the direct band gap is low at normal conditions.

However, in the case of ultrashort laser pulses, the absorption at visible and NIR ranges is significant due to multiple effects. Here, depending on the peak laser intensity the pulse energy can be absorbed by one-, two- or multiphoton ionization. Avalanche ionization is another possible process, in which a conduction band electron directly absorbs additional photons and then collides with a valence electron resulting in two electrons at the bottom of the conduction band, which start the process once again [90]. It was demonstrated that the two-photon absorption was a dominant mechanism for 620-nm 100-fs laser pulses [91], while for 800-nm 100-fs pulses the absorption was governed by the avalanche ionization [90]. These phenomena become relevant at high intensities of laser radiation, which is characteristic for ultrashort laser-matter interactions. Upon the ionization of semiconductors free charge carriers are created consisting of a pair of an electron and a corresponding hole. The holes tend to be mobile and behave like free electrons with an opposite charge contributing to the absorption process. It should be noted that the ionization and band transitions occur within few femtoseconds [92–94], and then the electrons and holes behave like free electrons in metals.

The energy transfer from a femtosecond laser radiation to a solid target can be divided into three steps. First, the absorption of the laser pulse energy by free charge carriers leads to the thermalization of the electronic subsystem. Then, the electron relaxation occurs and the electronic subsystem reaches the equilibrium, The electron equilibration time is of the order of magnitude of the inverse plasma frequency, *i.e.* $\sim 10^{-2}$ fs, which is much faster than the pulse duration. However, at this moment hot electrons or electron-hole plasma still co-exist with “cold” ions. The thermal diffusion is the last step, which transfers energy from electrons to ions. The electrons and the ions reach a thermal equilibrium through electron-ions collisions. However, this process takes much longer time than the pulse duration (usually at the order of picoseconds).

A two-temperature model is applied to describe such processes as heating, melting and material ablation. This model was first proposed by Landau and Kaganov [95] and then applied by Anisimov to laser-matter interactions [96]. The model is valid under the assumption that the thermalization within the electron subsystem is fast and the pulse duration exceeds electrons equilibration time. Electron and lattice subsystems can be characterized by their temperatures

(T_e and T_i), and the energy transport can be described by the following equations:

$$C_e \frac{\partial T_e}{\partial t} = -\frac{\partial Q(z)}{\partial z} - \gamma(T_e - T_i) + S \quad (1.1)$$

$$C_i \frac{\partial T_i}{\partial t} = \gamma(T_e - T_i) \quad (1.2)$$

$$Q(z) = -k_e \frac{\partial T_e}{\partial z} \quad (1.3)$$

$$S = I(t)A\alpha e^{\alpha z} \quad (1.4)$$

Here, C_e and C_i are the heat capacities of the electron and lattice subsystems, z is the direction perpendicular to the target surface, γ is the parameter characterizing the electron-lattice coupling, k_e is the electron thermal conductivity, A and α are the surface absorptivity and the material absorption coefficients. Q is the heat flux. S is the laser energy term absorbed by the material. Generally, a Beer-Lambert law is applicable to describe the energy absorption in the material. $I(t)$ represents temporal evolution of laser pulse. The temporal shape of the pulse can be described as an increasing exponential function $I(t) = I_0 e^{t/\tau_p}$ for the $t < 0$, where τ_p is the pulse duration. At the moment $t = 0$, the laser pulse is switched off.

Thermodynamic parameters C_e and k_e depend on the electrons and lattice temperatures. When the electron energy remains smaller than the Fermi energy $C_e = C'_e T_e$ (where C'_e is constant) and $k_e = k_0(T_i) T_e/T_i$ (where $k_0(T_i)$ is the conventional equilibrium thermal conductivity). At electron temperatures higher than the Fermi temperature, C_e is determined as $C_e = 3N_e k_B/2$ (N_e is the electron density and k_B is the Boltzmann constant), k_e can be described as $k_e \sim T_e^{5/2}$.

Equations (1.1–1.3) have three characteristic time scales: t_e , t_i and τ_p , where $t_e = C_e/\gamma$ is the electron cooling time, $t_i = C_i/\gamma$ is the lattice heating time ($t_i \gg t_e$) and τ_p is the duration of the laser pulse. In the femtosecond regime, the condition $t_i \gg t_e \gg \tau_p$ is fulfilled.

Nolte *et al.* [97] provided an analytical solution of this system in the case of ultrashort laser pulses. They neglected the first stage of the laser heating where the electrons are out of equilibrium. The heat capacity, the electron thermal conductivity and the electron thermal diffusivity $D = k_e/C_e$ were assumed constant. To solve the equations, they used initial temperature and the continuity of electronic temperature as boundary conditions:

$$T_e(z, t = -\infty) = T_i(z, t = -\infty) = T_0 \approx 0 \quad (1.5)$$

$$\left. \frac{\partial T_e}{\partial z} \right|_{z=0} = \left. \frac{\partial T_e}{\partial z} \right|_{z=\infty} = 0 \quad (1.6)$$

According to the solution of the equations proposed by Nolte *et al.* [97], the spatial profile of the lattice temperature after the reaching the equilibrium is described as follows:

$$T_i(z) = \frac{F_a}{C_i} \frac{1}{l^2 - \delta^2} \left(l e^{-z/l} - \delta e^{-z/\delta} \right), \quad (1.7)$$

where $F_a = I_0 A \tau_p$ is the laser fluence absorbed by the target, $\delta = 1/\alpha$ and l are optical and heat penetration depths. Here, it is implied that the electronic and lattice temperatures evolve linearly.

It is worth noting that the two-temperature model for the description of the pulse absorption properties is rather simplified and cannot be used for precise simulations. However, it can explain some experimental tendencies. For more accurate description, the solution of the system should be completed by the equation of state for the ablation of material. Another problem is that properties of the material strongly depend on its temperature. During the laser irradiation, the increase of electronic temperature causes variations of the absorption coefficient and of surface absorptivity [98].

Despite its simplicity, the two-temperature model is frequently used as a basis for more complex modeling for studies of molecular dynamics [99–102] or hydrodynamic [103, 104] modeling of material ablation. Some studies [105] propose a solution of the problem taking into account temperature dependences of thermodynamic parameters. This model is in good agreement with ablation threshold values found experimentally. The two-temperature model is also used as a starting point for models describing precisely the thermodynamic evolution of material, including phase transitions, structure transformations and non-equilibrium processes [99–101]. In addition, this model was applied for an interpretation of pump-probe measurements and determination of thermal conductivity and electron-phonon coupling coefficient [105–108]. Finally, it was used to predict the threshold fluence for damage or fusion [97, 105, 109], to describe the species desorption from a metal surface [110] or ions ejection dynamics during the laser ablation [111].

1.2.3 $t = 10^{-12}$ to 10^{-10} s: ejection of ablated material

After laser energy absorption followed by the ionization (in the case of the semiconductors and insulators), free carriers thermalization, and the transfer of the energy to the lattice, the material ablation occurs. The mechanisms that govern the material ablation under the femtosecond regime are still under discussion. We can list several possibilities:

- Thermal mechanisms: fast heating of material results in the vaporization or thermodynamically instable liquid phase explosion, and leads to the ejection of a vapor-liquid mixture [99, 101, 112, 113].

- Electrostatic mechanism: electric field of laser radiation induces the ejection of electrons from the material, leading to the formation electric field on the surface of the target. Under the action of this field, ions are accelerated and ejected from the target [114,115].
- Coulomb explosion: electric field of laser radiation induces the ejection of electrons from the material, leading to its charging. Repulsion forces between ions of the lattice increase and lead to bond ruptures and the explosion of the lattice [116,117].
- Photomechanical mechanisms: the shock wave propagation in material induces an expansion wave that can lead to the ejection of material in the form of nanometric or bigger fragments [112,113,118]

A concrete scenario for ablation mechanism strongly depends on the nature of material and laser parameters. Numerical simulations take into account several possible ablation mechanisms and use different methods such as: molecular dynamics [99,102,112,119], hydrodynamic methods [103,104,120] and direct simulation Monte Carlo [113].

In the frame of the thermodynamic approach, three types of processes are typically considered for the description of material ejection: evaporation, normal boiling and “explosive boiling” [121]. Explosive boiling, also called “phase explosion”, occurs when a solid target is rapidly superheated up to the critical temperature, leading to its spinoidal decomposition in liquid and vapor phases by homogeneous nucleation [121]. However, when the energy is deposited to the target by ultrashort laser radiation, molecular dynamics simulations demonstrate that the material ejection is too fast and far from the thermodynamic equilibrium to be described as the explosive boiling [119,122–124]. In this case, the ablation mechanism is referred as “fragmentation”^{*} and involves the ejection of hot atoms, vapors and liquid droplets under non-equilibrium conditions [124]. Snapshots of the fragmentation process obtained by molecular dynamics simulations are presented in Figure 1.1.

In contrast to the atomistic approach of molecular dynamic simulations where each atom or particle is considered separately, hydrodynamic calculations are based on the complete equation of state considering the system in general. Numerical studies of the femtosecond ablation of metals demonstrated three possible ablation mechanisms: (i) direct atomization; (ii) thermal decomposition through the phase explosion and (iii) mechanical decomposition through the fragmentation of the metastable liquid. The third mechanism was found to be dominant at laser

^{*}In the literature there is some confusion in the employment of the term “fragmentation”. Some authors refer to it as a process of non-equilibrium material ejection. In other papers the fragmentation is related to the transformation, in particular size reduction, of the colloidal nanoparticles under the laser irradiation. Except current section devoted to the ablation mechanisms, in this thesis we will follow the second definition of the fragmentation.

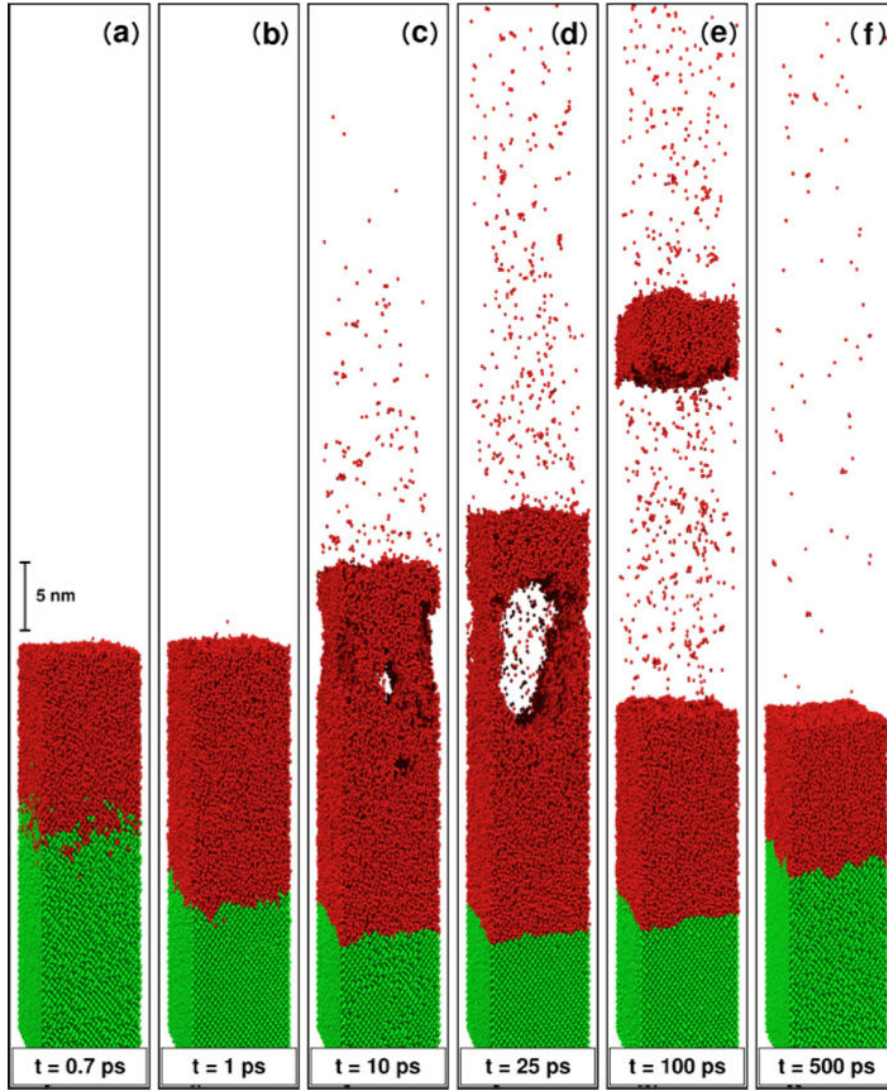


Figure 1.1: Molecular dynamics simulations of the ablation of the Si by 500 fs laser pulses. Green: crystalline semiconducting Si, red: liquid metallic Si. From Ref. [124].

fluences from 0.1 to 5 J/cm² [104].

We can apply the two-temperature model to get an estimation of the quantity of the ablated material and minimal fluences values that are needed to trigger the ablation. In the work of Nolte *et al.* [97] it was assumed that the ablation occurs through the thermal mechanism. Based on this supposition they considered two separate cases when the optical penetration depth is much smaller or much larger than the heat penetration depth, yielding the following expressions for the ablation depth L :

$$L \simeq \delta \ln \left(F_a / F_{th}^\delta \right) \quad (\delta \gg l) \quad (1.8)$$

$$L \simeq l \ln \left(F_a / F_{th}^l \right) \quad (\delta \ll l) \quad (1.9)$$

The optical regime of ablation takes place at low laser fluences. Here, due to relatively low electron temperature, a thermal diffusion is less significant. In contrast, at high fluences heat penetration process becomes dominant. Indeed, at higher fluences the electronic diffusion is more significant, and the quantity of the ablated material is larger. Under some conditions, the absorbed laser fluence can be higher than the threshold fluence. Expressions for the fluence thresholds in “optical” and “heat” regimes are determined as:

$$F_{th}^{\delta} = \frac{\rho\Omega\delta}{A} \quad (1.10)$$

$$F_{th}^l = \frac{\rho\Omega l}{A} \quad (1.11)$$

Here, ρ is the density of the material, and Ω is the specific heat of the evaporation per mass unit. We can apply formulae (1.10) and (1.11) to estimate the ablation thresholds for gold. Ω and ρ of gold are 19.3×10^3 g/m³ and 1698 kJ/kg, respectively [125]. The optical penetration depth is $\delta = 13$ nm [125], electronic heat penetration depth was estimated as $l \approx 80$ nm [97]. We fixed the absorptivity A at 20%, that is significantly higher than tabulated value of 1.9% at 1000 nm [126] or $A = 0.6\%$ estimated according to the Drude model [127]. Here, we assumed that electron temperature significantly affects the material properties, and the value of the absorptivity can considerably increase during the action of the laser pulse [98]. Thus, the calculations give us the threshold values of $F_{th}^{\delta} = 0.21$ J/cm² for the “optical” regime of ablation and $F_{th}^l = 1.3$ J/cm² for the “heat” regime.

The model proposed by Nolte *et al.* [97] is based on the hypothesis of thermal evaporation, without taking into account other possible mechanisms of ablation. Gamaly *et al.* [114, 115] proposed that femtosecond ablation can occur through the electrostatic mechanism, which is based on the supposition that the ions are triggered out of the target by energetic electrons. Thus, we have the following ablation conditions: by the end of the laser pulse the electron energy (ϵ_e) must reach the value equal to the sum of the atomic binding energy (ϵ_b) and the energy that electron needs to escape the solid, namely the work function (ϵ_{esc}):

$$\epsilon_e = \epsilon_b + \epsilon_{esc} = \frac{2 AI_0 \tau_p}{3 \delta N_e} \quad (1.12)$$

The threshold fluence for the electrostatic ablation can be described as:

$$F_{th}^{es} \equiv I_0 \tau_p \approx \frac{3}{8} (\epsilon_b + \epsilon_{esc}) \frac{\lambda N_e}{2\pi} \quad (1.13)$$

This formula explains the experimentally observed dependence of the threshold fluence on the laser wavelength λ . Thus, the estimation of the ablation threshold according to the model proposed by Gamaly *et al.* [114,115] gives the value of 0.5 J/cm^2 for 1053 nm ultrashort pulses, which is rather close to the experimental value of $0.45 \pm 0.1 \text{ J/cm}^2$ [128].

These models are rather precise for the estimation of the ablation threshold for metals. However, in the case of the semiconductors, the energy required for the ionization and creation of charge carriers should also be taken into account. Experimental thresholds for the femtosecond ablation of silicon are in the range of $0.2\text{--}0.3 \text{ J/cm}^2$ for $5\text{--}500 \text{ fs}$ pulses at 800 nm [129,130].

The role of the photoionization during the material ejection seems to be insignificant. Indeed, a high carrier mobility in metals and semiconductors inhibits the charging of the material necessary to the charge-related material detachment through the Coulomb explosion or electrostatic ablation [116]. Simultaneously to the ablation process two shock waves are formed: one propagates into the target and the another goes into the liquid solution with a supersonic velocity. Shockwave propagation can heat the liquid and the target, which can provide the detachment of material from the target [131–133]. The ablated material is composed of ionized species due to high temperature and photoionization [131]. A fraction of the material is atomized, while another one is ejected in the form of clusters and particles, as demonstrated by molecular dynamics simulations [124]. Besides, the plasma plume can also contain molten drops and solid fragments [112,134]. When the pulse duration is of the order of tens of picoseconds or longer, laser pulse can overlap with the plasma plume, reducing the amount of energy delivered to the target. This effect is called “plasma shielding”. However, in femtosecond regime the plasma is formed after the end of the pulse and plasma shielding effect is negligible.

1.2.4 $t = 10^{-10}$ to 10^{-6} s: expansion and quenching of the plasma plume, nucleation, cavitation bubble formation

After 10^{-10} s the plasma plume expands adiabatically behind the shockwave and it cools down in the solution by releasing its energy to the liquid and the solid target. The liquid is heated to temperatures of the plasma plume, *i.e.* $\sim 1000 \text{ K}$, that can induce the pyrolysis, degradation and ionization of the solution and solvent molecules (if any) [135]. If the pulse intensity is high enough, a cavitation bubble is formed in the liquid, while the plasma expands inside it [136,137].

At the stage of the plume expansion, the plasma number density is high, and temperature is low, especially in the case of short and ultrashort laser pulses. These conditions are favorable for the nucleation and formation of small primary nanoparticles. The size of the nanoparticles is controlled by the free energy:

$$\Delta G(n, c) = -nkT \ln \frac{c}{c_0} + 4\pi r^2 n^{2/3} \sigma, \quad (1.14)$$

where n is the number of monomers in the nucleus, k is the Boltzmann constant, r is the effective radius of the plume species (gold or Si atoms), c is the concentration of the species, c_0 is the equilibrium concentration, and σ is the effective surface tension. The nuclei can evaporate or grow due to the addition of monomers or clusters. These clusters are seeds for the following longer nucleation and growth when the plasma plume starts to cool down and the ablation species mix with the solution species [133].

As demonstrated by hydrodynamic calculations [103], in the case of the ultrafast ablation the major part of the primary nanoparticles originates from the ejection and fragmentation of a liquid layer during the material removal stage, while a smaller fraction of nanoparticles comes from the condensation inside the cavitation bubble. Therefore, the nuclei are produced directly during the material ejection, and the particle growth and coalescence occur during the further stages of the extension of the plasma plume and mixing of the plasma species with ones from the solution. However, the ionization state of the solution species during the stage of the plume expansion is still unclear. The relative contribution of the liquid droplets present in the plasma plume also needs to be clarified. For example, it is not clear if the molten material solidifies or it is further vaporized with subsequent nucleation and particles growth. It is also not clear if the liquid nuclei undergo the coalescence and aggregation if the number of the produced nuclei is high enough for collisions between them.

The polycrystallinity of nanoparticles obtained by laser ablation indicates the coalescence of the nuclei [71,74]. The regular spherical shape of the nanoparticles (especially for those produced by the femtosecond laser ablation [56,60]) reveals that the nuclei coalesce when they are still in the liquid phase, or when their temperature is high enough to allow the rearrangement of the surface atoms.

1.2.5 $t = 10^{-6} - 10^{-4}$ s: expansion and collapse of the cavitation bubble

Perturbations of the pressure during the expansion and quenching of the plasma plume lead to the formation of a cavitation bubble. We consider this effect as a separate event because the expansion and collapse of the bubble occur after the disappearance of the laser plume. The bubble arises at the time scale of $10^{-7} - 10^{-6}$ s [138,139] and expands up to the times of order of 10^{-4} s. During the expansion of the bubble, the inner temperature drops and the pressure decreases to values lower than the surrounding liquid. This leads to the collapse of the bubble and the generation of a second shock wave.

A fraction of nanoparticles is formed inside the cavitation bubble during its expansion, as it was demonstrated in several works [123, 133, 136, 140]. However, it was also found that the nanoparticles could also traverse the borders of the expanding cavitation bubble [141]. The concentration of the solution species inside the cavitation bubble is much lower than in surrounding liquid, and they are in higher energetic states. Moreover, temperature inside the bubble is higher, and the thermal conductivity of the gas is lower than that of the liquid. All these facts tend to prove that if nanoclusters are released from the plasma plume and trapped inside the bubble, they remain “hot” for a long time and can continue to undergo the nucleation and condensation [59]. It should be noted that for the moment of the formation and expansion of the bubble the majority of the nanoparticles are already formed and dispersed inside the solution volume.

The second shockwave generated after the bubble collapse can have drastic impact on the nanoparticles formation [142]. For example, it can cause the mechanical detachment of the material from the solid target [139, 143] yielding a secondary formation of nanoparticles.

1.2.6 $t > 10^{-4}$ s: growth and agglomeration of the nanoparticles

After the second shock wave, the system returns to a stable physical and chemical state. Only slight modifications of the nanoparticles can occur due to the remaining ablated atoms and clusters. Further processes such as aggregation in the case of unstable systems, are governed by chemical kinetics and usually occur on a timescale of several minutes. Surface oxidation of the nanoparticles is also possible at this stage [59].

1.3 Laser irradiation of colloidal solutions

1.3.1 Propagation of the laser pulse in a liquid medium

When a focused femtosecond laser beam propagates through a condensed medium, two non-linear effects occur: the optical breakdown of the liquid and the filamentation [86, 144]. The optical breakdown is related to the absorption of the pulse energy by the liquid and plasma generation. The plasma energy is transmitted to the surrounding liquid inducing the vaporization and the formation of a cavitation bubble and a shockwave. The filamentation results from the balance between self-focusing of a laser pulse and the defocusing effect of the plasma generated at high intensities [87]. The filamentation is accompanied by the broadening of the spectrum of the laser radiation, leading to its extension from ultraviolet (UV) to NIR, which is also called the supercontinuum generation [88].

1.3.1.1 Optical breakdown

The optical breakdown starts from the multiphoton ionization or excitation, followed by the inverse Bremsstrahlung and a cascade ionization resulting in the generation of a strongly ionized plasma [145]. The number of free electrons increases during the avalanche ionization according to the exponential law:

$$N_e(t) = N_{e,0} e^{t\nu_i}, \quad (1.15)$$

where $N_{e,0}$ is the background initial density and ν_i is the ionization frequency. The ionization frequency can be found as:

$$\nu_i = \frac{1}{W_g} \frac{e^2 E^2}{2m (\omega_0^2 + \nu_c^2)} \nu_c, \quad (1.16)$$

where W_g is the material band gap, E is the electric field amplitude, ω_0 is the laser central frequency, m and e are the electron mass and charge. ν_c is the electron collision frequency, which is proportional to the square root of the laser intensity. Since laser intensity can be expressed through the electric field amplitude as $I = 0.5c\epsilon_0 n |E|^2$ (where c is the speed of light in the vacuum, n is the refractive index and ϵ_0 is the vacuum permittivity), the avalanche ionization frequency is proportional to the laser intensity: $\nu_i \sim I^{3/2}$. Consequently, the threshold of the optical breakdown depends on the laser intensity.

Different definitions of the electron density threshold for optical breakdown generation can be found:

- “bubble” endpoint: the appearance of the vapor bubbles in water [146];
- “flash” endpoint: the appearance of visible emission [146];
- critical density of plasma $N_{cr} = \pi m c^2 / (e^2 \lambda_w^2)$, where λ_w is the laser wavelength [147].

The “bubble” threshold is often used for the ultrashort pulses, while the “flash” one is normally applied in cases of long (nanosecond) pulse durations. The choice of the threshold depends on experimental technique employed for the breakdown detection. In our work, we detected the optical breakdown by the acoustic signal accompanying the bubble collapse, in accordance with the first definition. The threshold breakdown electron density found by Kennedy *et al.* [146] is equal to $N_{e,th} \approx 10^{18} \text{ cm}^{-3}$. Liu *et al.* [86] estimated the threshold breakdown intensity for 810-nm, 45 fs pulses $I_{th} = 8.8 \times 10^{12} \text{ W/cm}^2$. In the work [145] the calculated threshold intensity for 580-nm 400 fs pulses was equal to $I_{th} = 2.7 \times 10^{12} \text{ W/cm}^2$.

According to Ref. [148], we have the following evolution of process. During the absorption of the laser pulse, the ionization occurs and the electron plasma is formed at the timescale of the laser pulse (in the range of few hundreds of fs). After a small delay of about 20 ps, necessary for the electron-ion energy transfer the plasma plume starts to expand. The expansion of the plasma occurs on the timescale of 30–200 ps, and it expands with a supersonic velocity of 30 $\mu\text{m}/\text{ns}$. Effects such as light scattering and reflection, heating of the surrounding liquid, plasma radiation and the formation of a pressure wave are associated with the formation and expansion of the plasma plume. After 800 ps, the pressure wave separates from the initial bubble and travels at the speed of sound in water. At the timescale of 10 ns the initial bubble starts to expand as a cavitation bubble. The cavitation bubble reaches its maximum at 5 μs and collapses by 11 μs . The collapse is accompanied by shock wave emission, that can be detected as acoustic signals. However, the conversion efficiency of the transformation of the laser pulse energy into the mechanical energy (via the cavitation bubble formation and shock wave generation) does not exceed 25% and remains low compared to the conversion efficiency obtained for longer pulses [149].

1.3.1.2 Filamentation and supercontinuum generation

Two main mechanisms are responsible for the generation of the femtosecond continuum: self-phase modulation and self-focusing [88]. These effects are associated with the Kerr nonlinearity that consists in the change of the refraction index in response to the applied strong electric field. In a Kerr medium the refraction index is determined as:

$$n = n_0 + n_2 I, \quad (1.17)$$

where n_0 is the linear index of refraction, n_2 is the nonlinear index of refraction and I is the field intensity. In the same manner the temporal distribution of the non-linear phase of the laser beam leads to the self-phase modulation. During the propagation through the medium with refraction index of $n = n_0 + n_2 I$ by a distance L , a laser pulse with intensity distribution $I(z, t)$ gains nonlinear phase distribution:

$$\phi_{NL}(t) = \int_0^L n_2 I(z, t) \frac{\omega_0}{c} dz, \quad (1.18)$$

where ω_0 is the laser frequency and c is the speed of light in vacuum. The spectrum covers frequencies in the range from maximum Stokes extent to the minimum one with a width of each side:

$$\Delta\omega^{\text{SPM}} = -kz \frac{\partial n_2}{\partial t}, \quad (1.19)$$

where z is the propagation coordinate and k is the wave number. According to this model, the spectral broadening is symmetric relatively to the peak of the pulse. Self-phase modulation is extremely strong in the femtosecond regime, because the Stokes and anti-Stokes broadening are inversely proportional to the pulse duration. Free-electron generation arising due to the multi-photon ionization of the surrounding medium contributes greatly to the spectral transformation. The frequency deviation (Eq. (1.19)) is positive due to a negative contribution of n_2 from free electrons. Therefore, the spectral broadening is asymmetric and blue shifted relatively to the laser peak.

Simple self-phase modulation cannot explain the frequency deviation up to hundreds of nm observed in the experiments. It is accepted that the self-focusing also contributes to the spectral broadening. It occurs when the power exceeds the critical power [88]:

$$P_{\text{crit}} = \frac{3.77\lambda_0^2}{8\pi n_0 n_2}, \quad (1.20)$$

where λ_0 is the laser wavelength. Without external focusing a Gaussian beam with a power P focuses at the distance:

$$z_f(P) = \frac{0.367ka_0^2}{\left[\left(\sqrt{P/P_{\text{crit}}} - 0.852\right)^2 - 0.0219\right]^{1/2}}, \quad (1.21)$$

where $k = 2\pi/\lambda_0$ is the wave number and a_0 is the beam radius at the $1/e$ level of the beam profile. When a lens with a focal length f is used for external focusing, the position of the self-focus changes to:

$$z'_f = \frac{z_f f}{z_f + f} \quad (1.22)$$

With a positive focusing, $z'_f < f$, and self-focusing occurs before the geometrical focus. Free electrons arising from multi-photon and avalanche ionization can also influence the self-focusing in condensed media. Free electrons induce a negative change in refraction index. At electron densities at the level of $10^{17} - 10^{18} \text{ cm}^{-3}$ the Kerr index $n_2 I$ is canceled and the self-focusing stops [88]. The critical power P_{crit} for the self-focusing during the propagation of the 140-fs laser pulse at $\lambda_0 = 796 \text{ nm}$ in water was found to be equal to 4.2 MW, which roughly corresponds to the critical power for the generation of the supercontinuum [150].

The femtosecond continuum has several characteristic features [87]: (i) the spectral width

of the supercontinuum depends on the medium in which it is generated; (ii) this spectrum is modulated; (iii) the continuum is polarized in the same direction as the input laser pulse. When the femtosecond continuum is generated in water, the effect of the conical emission is observed, which manifests itself as a white spot surrounded by the rainbow circles when projected on a screen.

The supercontinuum generation and optical breakdown usually coexist during the propagation of the femtosecond laser pulse in water. However, the threshold for the optical breakdown is determined by the intensity, while the supercontinuum generation is defined by the laser power. This means that the competition between these two effects depends on the focusing geometry. Tight focusing facilitates the intensity increase and favors the optical breakdown. In the case of weak focusing, the threshold power for the optical breakdown increases, and under some conditions it can overcome the threshold for the supercontinuum generation. Therefore, by changing the focusing geometry and pulse energy, we can foster one or another mechanism [86].

1.3.2 Interaction of femtosecond laser radiation with colloidal particles

Numerous works demonstrated that the pulsed laser irradiation of a colloidal solution can affect nanoparticle growth [54, 80–82, 151–154]. The size of the nanoparticles is often reduced [80, 83, 151] and the size distribution is narrowed, leading to an increased stability of nanoparticle solutions [81, 82]. The laser post-irradiation can also induce shape changes, similarly to how it was observed in the case of gold nanorods transforming into spherical nanoparticles [152, 155, 156]. The mechanism of the interaction of the nanoparticles with the laser pulse is not the same as for the bulk material, first of all because of the small size of the nanoparticles, and the new properties of the material arising at the nanometric scale. Three mechanisms of the interaction between gold nanoparticles and pulsed laser irradiation were proposed: photothermal mechanism, Coulomb explosion and near-field ablation [160].

1.3.2.1 Photothermal mechanism

Koda *et al.* [151] proposed a photothermal concept in order to explain the observed size reduction of chemically prepared gold nanoparticles under laser irradiation. This model is based on the assumption that the laser pulse energy absorbed by a nanoparticle is consumed via the heating-melting-evaporation process. The energy absorbed by a nanoparticle can be determined as:

$$E_{abs} = JC_{abs}^{\lambda}, \quad (1.23)$$

where J is the laser fluence and C_{abs}^{λ} is the particle absorption cross section. It should

be noticed that the absorption cross section depends strongly on the laser wavelength and the particle size. Depending on the amount of the laser energy absorbed, different processes can occur. At very low laser fluences only particles heating is expected, while when more energy is absorbed, the melting occurs, and finally at high energies, the particle reaches the boiling temperature and evaporates. Roughly this process can be described as:

$$JC_{\text{abs}}^{\lambda} = m_p [(H_{T_m} - H_0) + \Delta H_m + (H_{T_b} - H_{T_m}) + \Delta H_{\text{evap}}], \quad (1.24)$$

where m_p is the mass of one particle, ΔH_m and ΔH_{ev} are melting and boiling enthalpies, respectively. $(H_{T_m} - H_0)$ is the enthalpy change during the heating from the initial temperature to the melting point, and $(H_{T_b} - H_{T_m})$ is the enthalpy change during the heating from melting to the boiling point. Apart from particles phase transitions the absorbed laser energy can be dissipated to heat losses. Usually two effects are responsible for that: radiative cooling and heat transfer between a particle and the liquid medium.

Further investigations revealed that the photothermal size reduction happens through the layer-by-layer mechanism [157]. In addition, it was demonstrated that the pumping wavelength plays an important role in the efficiency of this process. Pyatenko *et al.* [154, 158] supposed that the excitation by 532-nm wavelength (that is close to the plasmonic absorption band of gold nanoparticles) is more effective than one for 1064 or 355-nm wavelengths. On the other hand, Werner *et al.* [159] found that the interband excitation is more effective than the excitation at local surface plasmon resonance.

The scenario of the photothermal size reduction mechanism can be described by a scheme presented in Figure 1.2 [160]. During laser-induced heating of a nanoparticle, thermal energy is transferred to the surrounding liquid. Under fast heating, water undergoes explosive evaporation, and a “hot” high-pressure bubble rapidly expands. If the laser intensity is high enough to heat up thermally insulated nanoparticles to the boiling point, surface evaporation and consequently size reduction of initial Au nanoparticles occur. The generated fragments may form aggregates due to a low permittivity inside the bubble. Finally, after the collapse of the bubble the nanoparticles cool down to the ambient temperature. Therefore, “nanonetwork” and “snake-like” structures often coexist after the laser irradiation of gold colloids [54, 161].

1.3.2.2 Coulomb explosion

In the Section 1.2.3 we discussed the Coulomb explosion mechanism in terms of laser ablation from a bulk target. We mentioned that due to high carriers mobility the probability and efficiency of this mechanism is low for metal or semiconductor targets. These limitations are less restrictive

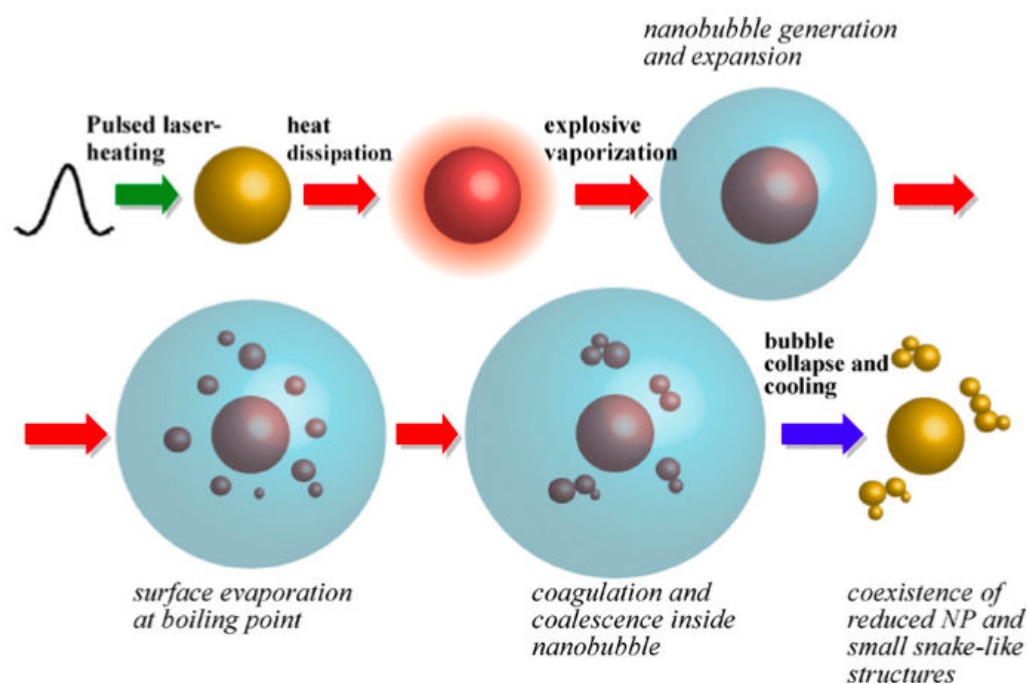


Figure 1.2: Scheme of the nanoparticles size reduction based on the photothermal mechanism. From Ref. [160].

when the nanoparticles interact with a laser pulse, due to their small size. Indeed, there is no source of free electrons from the bulk material to compensate the electrons removal, and therefore the particle charging can occur, followed by the lattice explosion.

The Coulomb explosion mechanism involves the excitation and ejection of the free electrons from the nanoparticle. This leads to the formation of multiple ionized nanoparticles that undergo spontaneous fission due to the charge repulsion. Kamat *et al.* [162] provided an experimental evidence of this mechanism, namely they detected hydrated electrons during 355-nm picosecond irradiation of gold nanoparticles. Yamada *et al.* [163,164] also observed the hydrated electrons under intense nanosecond irradiation of gold colloids. They also detected positively charged Au ions with the help of the mass-spectroscopy.

Werner and Hashimoto [165] provided temperature calculations to elucidate the precise mechanism of laser-nanoparticle interactions and its dependence on the pulse duration, laser energy and the excitation wavelength. They applied a two-temperature model to describe the electron-lattice heating and the liquid-droplet model to describe the fragmentation. Three temperatures were considered: the electron temperature (T_e), the lattice temperature (T_l) and the temperature of the medium surrounding the nanoparticle (T_m). Here, one should take into account that a fraction of energy F is transferred between the particle and its surroundings. Therefore, the following system describes the evolution of electron and lattice temperatures:

$$C_e \frac{\partial T_e}{\partial t} = -\gamma(T_e - T_i) + S \quad (1.25)$$

$$C_i \frac{\partial T_i}{\partial t} = \gamma(T_e - T_i) - F \quad (1.26)$$

$$C_m \frac{\partial T_m}{\partial t} = \frac{1}{r^2} \frac{\partial}{\partial r} \left(k_m r^2 \frac{\partial T_m}{\partial r} \right) + F \quad (1.27)$$

The equation (1.27) describes temperature on an external spherical surface dependent on time and the distance from the particle center, where C_m , and k_m are the heat capacity and the thermal conductivity of the medium, respectively. The heat transfer from the lattice to the surrounding medium F is described as:

$$F = \frac{hA_p}{V_p} [T_i - T_m(R)], \quad (1.28)$$

where h is the interface thermal conductivity, A_p and V_p are the particle surface area and the volume respectively. $T_m(R)$ is the maximum water temperature at the nanoparticle-water interface, where R is the radius of the nanoparticle.

The Coulomb explosion mechanism is possible when the electron temperature exceeds a certain threshold value. At the electronic temperature as high as 5000 K, the energetic electrons have enough energy to escape from the surface. To cause the Coulomb explosion, charge repulsion forces should overcome the surface tension, so that the droplet undergoes the explosion. This effect is known as the Rayleigh instability. Werner *et al.* [165] estimated the threshold, after which the electron temperature is high enough for the emission of a sufficient number of electrons and the production of the Rayleigh instability. For example, the electron temperature threshold for the fragmentation of 60-nm gold nanoparticles is 7300 K in the liquid state and 8200 K in the solid state. It is worth noting that the Coulomb explosion occurs more easily when a nanoparticle is in the liquid phase, *i.e.* when it is present in the form of a liquid droplet. There are two reasons for this effect. First, in liquids the charge carriers are less mobile that facilitates a strong localized charging of the material. Second, the liquid droplet is less stable than the solid matter because of the reduced surface energy; therefore the Rayleigh instability is more easily achieved.

Werner *et al.* [166] described the evolution of processes during nanoparticles fragmentation through the Coulomb explosion. This time evolution of the process is shown schematically in Figure 1.3. At the fluences higher than the fragmentation threshold (6 mJ/cm² for the fragmentation of 60-nm nanoparticles by irradiation with a 400-nm laser wavelength) laser energy is absorbed by electrons and the electronic temperature rises over 7300 K that is high enough to induce the thermionic electron emission. The lattice temperature increases up to 1337 K (the

melting point for gold) and a phase transformation from solid to liquid occurs within 3–10 ps. When the charge repulsion energy exceeds the Rayleigh instability threshold, the liquid droplet divides into smaller ones that separate into individual clusters at the timescale of 100 ps.

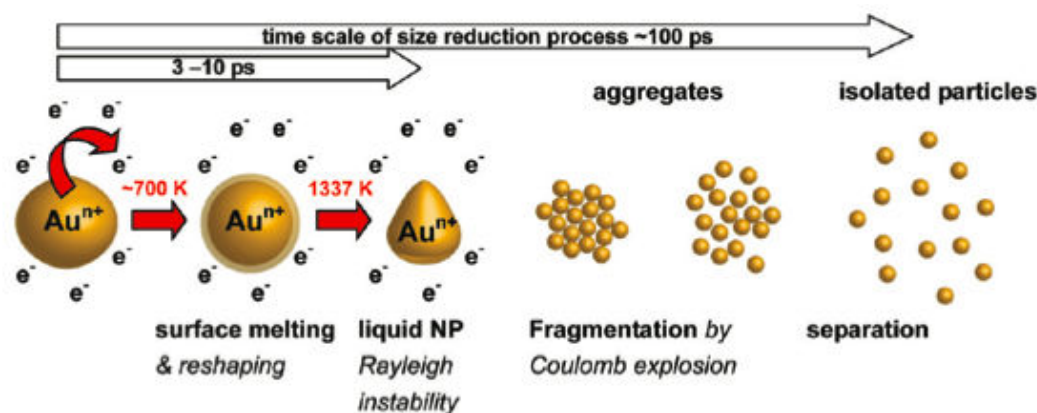


Figure 1.3: Scheme of the Coulomb explosion mechanism of the nanoparticles fragmentation. From Ref. [166].

Photothermal and Coulomb explosion mechanisms are often investigated individually, and there is no established concept to separate them. The model calculations presented in Ref. [165] demonstrated that the fragmentation mechanism depends on the pulse duration. The Coulomb explosion mechanism prevailed for the femtosecond fragmentation at 400 nm, while for 355 nm nanosecond excitation the photothermal evaporation mechanism was considered as the dominant one. At picosecond regime both mechanisms are possible depending on the laser fluence.

1.3.2.3 Near-field ablation

The third fragmentation mechanism was proposed for the femtosecond laser fragmentation at extremely high laser intensities (over 90 GW/cm^2 of the peak power). Near-field ablation of the gold nanoparticles is based on the fact that due to collective surface plasmon oscillations gold nanoparticles enhance dramatically the local electric field [167]. Plech *et al.* [168] analyzed time-resolved Bragg reflection intensity during the irradiation of gold colloids with 100-fs laser pulses and 400-nm excitation wavelength. They observed a mass removal from the poles of spherical nanoparticles when they were still at the solid state. They supposed that this shape change could be caused by the surface ablation from the particles through the near-field enhancement of the incident laser light.

However, this mechanism is still under discussion. First, it contradicts to results of Link [169] and Zijlstra [156], who considered the melting and shape transformations of gold nanorods under laser irradiation. Gold nanorods provide much stronger local-field enhancement effect than gold nanoparticles. However, in these experiments the nanorods could undergo direct melting and

transformation into spherical nanoparticles without any fragmentation. The calculations of the field intensity on the surface of 60-nm gold nanoparticles demonstrated that the field magnitude was not high enough to initiate sufficient ion emission [166].

1.3.2.4 Other processes

Apart the fragmentation of nanoparticles, other processes can take place under the pulsed laser irradiation of colloidal solutions. First, we cannot neglect the heat transfer from the excited nanoparticles to the surrounding liquid. This process is described by the equation (1.28). If we take into account that for a sphere with a radius R , the surface area is $A_p = 4\pi R^2$ and the volume V_p equals $4/3\pi R^3$, we can simplify the equation to:

$$F = \frac{3h}{R}[T_i - T_m(R)] \quad (1.29)$$

One can see that the temperature loss is proportional to the temperature gradient between the lattice and the surrounding medium. F is also inversely proportional to the particle radius. It means that smaller nanoparticles dissipate more energy to the surrounding water. In the case of femtosecond laser heating, the thermal equilibrium between the lattice and the medium is achieved after 600 ps. Also it is worth noting that the heat dissipation in femtosecond regime is much smaller than the one during the nanosecond-laser heating.

Heat transfer from the laser-heated nanoparticles to the surrounding medium leads to the formation of cavitation bubbles. Plech *et al.* [170, 171] experimentally studied the growth of the cavitation bubble upon the irradiation of the nanoparticles with 100-fs laser pulses. The bubble reaches its maximum size at the delay of 250 ps and collapses after 600 ps. The pressure increase caused by the bubble collapse initiates the formation of a smaller secondary bubble, which collapses at the nanosecond timescale.

Several groups observed the formation of larger nanoparticles under the nano- and picosecond laser irradiation [172–177]. In these studies, the irradiation of capped nanoparticles leads to the formation of larger nanoparticles up to a sub-micron size. The effect of the nanoparticles growth was explained by the phenomenon of a laser-induced fusion (melting) of the nanoparticles. However, the nanosecond irradiation of uncapped nanoparticles results in the agglomeration of the nanoparticles, yielding the destabilization of nanoparticles and their immediate precipitation [176]. As we will describe in Chapter 2, in our work we managed to increase the size of bare uncapped nanoparticles up to 40 nm under the femtosecond laser irradiation.

Si nanoparticles undergo the fragmentation under the laser irradiation as well as Au nanoparticles [73, 178]. However, the interaction of Si particles with a laser pulse has not been enough

studied, and there is no appropriate model for such interaction in the literature. We suppose that main mechanisms of the fragmentation of Au nanoparticles such as photothermal mechanism and Coulomb explosion are also applicable in the case of Si-based colloids.

1.4 Conclusion

Pulsed laser ablation involves complex physical and chemical processes, including heating, melting, ejection of species, vaporization, shock wave formation and propagation, plasma creation and expansion, and finally chemical reactions. Parameters of the produced nanoparticles are determined primarily by the mechanism of the ablation, which depends on pulse characteristics, such as the pulse duration and pulse energy. Ultrashort laser ablation has a number of specific features, that distinguish it from “long” pulse ablation. When pulse duration is shorter than lattice heating time, we can consider the femtosecond ablation as a non-thermal phenomenon. Thus, this regime has several practical advantages for the generation of nanoparticles in liquids:

- Reduction of the pulse energy that is required to induce ablation at fixed laser wavelength and focusing conditions;
- Minimization the laser-plume interaction and elimination of the heat affected zone;
- Separation in time of laser energy absorption and ablation;
- As the peak intensity of the femtosecond laser ($> 10^{12}$ W/cm²) at the focal point is much higher than that of the nanosecond laser ($< 10^{10}$ W/cm²), the femtosecond laser can create extreme conditions;
- Femtosecond laser induces non-linear phenomena (supercontinuum generation) and multi-photon absorption that can be beneficial for the interaction with particles dispersed in the solution.

However, the common model and a detailed mechanism of the pulsed laser-induced generation of the nanoparticles in liquids, especially in the case of ultrashort laser pulses, is still under discussion.

Chapter 2

Synthesis of the gold nanoparticles by laser ablation

Contents

2.1	Introduction	32
2.2	Context	32
2.2.1	Influence of physical parameters	32
2.2.2	Influence of chemical parameters	38
2.2.3	Laser fragmentation	42
2.3	Materials and methods	46
2.3.1	Materials	46
2.3.2	Ablation from the bulk target	46
2.3.3	Laser fragmentation and alloying	47
2.3.4	Measurements	47
2.4	Laser synthesis of gold nanoparticles	48
2.4.1	Ablation from a bulk target	48
2.4.2	Laser fragmentation	49
2.4.3	Capped gold nanoparticles	59
2.4.4	Alloy nanoparticles	65
2.4.5	Optical properties	67
2.5	Conclusion	70

2.1 Introduction

Metal nanoparticles are in the very focus of research related to the development of laser ablative synthesis. The interest to the fabrication of these nanoparticles is due to their potential applications in biomedicine, catalysis, nano-optics and nano-electronics, *etc.* In addition, a relative simplicity of control of parameters of metal nanoparticles (*e.g.* Au, Ag) by means of electronic microscopy or optical methods facilitates the optimization of the laser synthesis procedure.

In this Chapter, we will first overview previous works on the generation of Au nanoparticles in liquid media. Here, we will pay a particular attention to the influence of various experimental parameters on characteristics of synthesized nanoparticles. In the second part of this Chapter we will present our results on the development of femtosecond laser ablation and fragmentation methods for the synthesis of Au-based colloids. We will demonstrate the potential of ultra-short pulsed laser ablation for the controlled synthesis of bare gold nanoparticles and gold alloy nanoparticles, as well as gold-polymer complexes.

2.2 Context

Laser-ablative synthesis is characterized by a variety of factors, which can influence size characteristics of produced nanoparticles. Therefore, numerous approaches to tune nanoparticles size and composition are considered. One can divide the methods for the control of the nanoparticles parameters into two groups: physical and chemical. The physical methods imply size control by a variation of purely physical parameters (laser energy, focusing in liquid ambience), while the chemical methods involve various chemically active species, which interact with laser produced nanoclusters and thus affect their growth [59,183].

We can separately identify a method of the laser irradiation of preliminary produced colloids (laser fragmentation), as laser interaction with nanoscale objects differs from the interaction with a bulk material. Despite the difference, similar physical and chemical methods for the control of nanoparticles size characteristics are applicable in this case.

In this chapter, we will review previous works on the size reduction and shape transformation of Au nanoparticles under laser ablation and fragmentation.

2.2.1 Influence of physical parameters

2.2.1.1 Pumping laser wavelength

For the laser ablation from the bulk target, the choice of the wavelength is important due to several reasons. The absorption coefficient of the target depends strongly on the laser wave-

length. UV radiation is typically easily absorbed by interband transitions in metals [123]. More reactive species are produced by the UV ablation, and consequently more reactions between the target and solvent species occur. On the other hand, NIR pulses are absorbed by the defects and impurities on the metal target, and the absorption coefficient at longer wavelength is smaller [123]. At high intensities provided by ultrashort laser pulses, the multiphoton absorption and photoionization become the primary mechanisms of light absorption, even for NIR-range wavelengths [179]. Conventional laser systems used for ablation experiments operate at the visible (532 nm, second harmonic of the neodymium-doped yttrium aluminium garnet (Nd:YAG) laser) [53, 153, 180, 181] or NIR (1064 nm, fundamental wavelength of Nd:YAG laser or 800 nm of Ti:sapphire laser) [56, 60, 66, 135, 161, 182–184] wavelengths.

As soon as the nanoparticles absorb energy of laser irradiation, they can undergo further modifications [183, 185, 186]. If the concentration of the produced nanoparticles is relatively high, a significant part of the laser energy can also be absorbed by the nanoparticles in the solution before the laser pulse hits the target. For example, as 532 and 355 nm radiation interacts easily with gold nanoparticles, the photofragmentation of colloids takes place simultaneously with the laser ablation process [183]. The overlapping of two processes often results in the broadening of size distribution, lower ablation yields and the decrease of the nanoparticles average size [183, 185, 186].

2.2.1.2 Laser energy

The amount of deposited laser energy critically affects the efficiency of ablation process and ablation mechanisms [104, 124]. The ablation yield increases linearly with the increase of the pulse energy [187], but this phenomenon also leads to the increase of the particles size and the broadening of size dispersion. This is a complementary effect of the larger amount of ablated material yielding higher concentration of nanoclusters in the plasma plume, which favors their further growth. At high fluences multiple mechanisms of material ablation are possible simultaneously, which can result in appearance of different populations of nanoparticles (*e.g.* bimodal distribution) [56, 57]. Meanwhile monomodal size distribution can be achieved at low fluences when the only mechanism of the nanoparticles formation is possible, as numerical simulations confirm [103].

From the thermodynamic point of view during the femtosecond laser ablation at low fluences (near the threshold) the system undergoes isochoric heating forming a metastable metallic liquid. The liquid is adiabatically cooled down to the liquid-vapor phase where it is subjected to the phase explosion. The nanoparticles result from the liquid layer fragmentation and ejection from

the metastable liquid below the critical point. At higher fluences the front layers appear at near-critical or supercritical states, and the mass fraction of the liquid-gas mixture increases. The ablation involves both the fragmentation of the supercritical liquid, resulting in bigger nanoparticles, and formation of smaller nanoparticles from the liquid-gas mixture [103,124].

At high fluences, an additional mechanism related to the formation of plasma can take place, yielding the appearance of a separate population of nanoparticles having a relatively large mean size and a strong size dispersion. Energy from the hot plasma is transferred to the liquid yielding its local vaporization. The vapors then combine to a big cavitation bubble, which releases a huge amount of energy during its collapse (100–150 μ s) which can lead to secondary ablation and the appearance of additional population of nanoparticles.

2.2.1.3 Pulse duration

The pulse duration has a significant effect on the nanoparticles size, the size distribution and nanoparticles structure. Different ablation mechanisms are responsible for the material ablation at “long” (nanosecond) and “short” (pico- and femtosecond) pulse durations. While increasing the pulse length, thermal mechanisms are prevailing over the photoionization mechanisms [119, 122, 124, 179].

Nanosecond laser ablation can be considered as the heating ablation regime. Absorbed laser energy first heats the target surface up to the melting point, and then up to the vaporization temperature [123, 188]. As during nanosecond ablation there is enough time for heat conduction into the target to create a large layer of the melted material, the evaporation occurs from the liquid metal [121]. As an evidence of thermal nature of nanosecond ablation regime, craters left after the ablation (Figure 2.1(A)) typically have rough borders, carrying the marks of the ejected metallic liquid [189].

Nanosecond pulse is long enough to be temporally overlapped with the plasma plume, resulting in increased temperature, pressure and lifetime of the plasma. Thus, the extended plasma lifetime leads to the interaction of the ablated material with plasma, leading to, for example, the vaporization of melted droplets [112, 134]. Moreover, the shock wave induced by the laser can cause a “secondary” mechanical ablation leading to the formation of big fragments of irregular shape [139, 143]. Table 2.1 summarizes the results on the ablation of a gold target in pure water. Nanosecond ablation often results in 10–30 nm nanoparticles, but without additional stabilizing molecules or subsequent particles reshaping, the nanoparticles have broad size distribution and demonstrate poor stability. An example of the nanoparticles produced by the nanosecond laser ablation is shown in Figure 2.2.

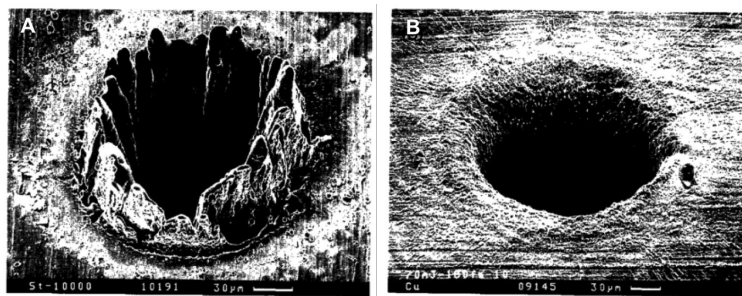


Figure 2.1: Scanning electron microscope pictures of the craters on metal target after laser ablation in gas with (A) 3.3 ns, 780 nm, 1 mJ and (B) 180 fs, 780 nm, 70 mJ pulses. From Ref. [189].

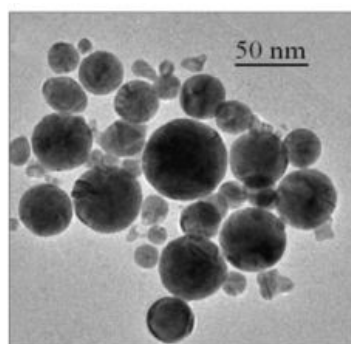


Figure 2.2: Transmission electron microscope image of the nanoparticles produced by the nanosecond ablation of a gold target (1064 nm, 9 ns, 10–20 J/cm²). From Ref. [65].

On the other hand, due to a short timescale involved, the ablation process at the femtosecond regime can be considered as an ultrafast local heating leading to a direct solid-vapor transition. The heat is conducted to the lattice at the picosecond timescale after the end of the laser pulse. Under these conditions, thermal conduction into the target can be neglected. Smooth shape and borders of craters formed by the femtosecond ablation, with no signs of heat-affected zone (Figure 2.1(B)), indicate that the ablation process is dominated by the direct photoionization [189]. This regime is also called “cold ablation”.

The results of the ablation of a gold target in pure water with femtosecond laser pulses are presented in Table 2.1. In most cases the nanoparticles produced by the femtosecond ablation are relatively small (less than 10 nm) and they are characterized by a narrow size dispersion. The colloids produced by the femtosecond ablation are stable even without any special treatment or addition of stabilizing molecules [56, 57]. However, at high laser fluences (>100 J/cm²) the particles exist in the the form of two populations: small particles with an average size around 5–10 nm and a narrow size distribution and a much larger (10–80 nm) and widely dispersed nanoparticles [56]. An example of a transmission electron microscope image of the two families of the nanoparticles obtained during the femtosecond ablation at 160 J/cm² and a corresponding size diagram demonstrating bimodal size distribution are shown in Figure 2.3. The reason for the

Nanoparticles size	Wavelength, nm	Pulse duration	Fluence, J/cm ²	Reference
<i>Nanosecond ablation</i>				
7–30 nm	1064	9 ns	10–20	[65]
10–30 nm	532	5 ns	0.2–1	[190]
20–40 nm (aggregated, elongated)	510	20 ns	1–2	[68]
2–32 nm (depending on laser fluence and wavelength)	1064/532	10 ns	7–88	[191]
9–23 nm	1064	7 ns	25	[192]
14–27 nm	1064	10 ns	2.5	[161]
12–24 nm	1064	10 ns	36	[194]
<i>Femtosecond ablation</i>				
3–10 nm	527	300 fs	1	[195]
3–5 nm	800	800 fs	60	[56]
two populations of 5–7 and 10–30 nm	800	800 fs	160	[56]
30–300 nm	800	800 fs	1000	[56]
20 nm	1045	700 fs	1	[196]
5–30 nm (depending on laser fluence, repetition rate and focusing conditions)	800	100 fs	25–1000	[186]
two populations of 10–20 and 40–70 nm	800	120 fs	880	[57]

Table 2.1: Table of gold nanoparticles produced by nano- and femtosecond ablation in pure water.

appearance of two different size distributions lies in the coexistence of two different mechanisms of the ablation. Based on the shape of clean craters with no sign of heat-affected zone, Kabashin and Meunier [56] supposed that at low laser fluences the ablation was due to the direct radiation-related photoionization. However, at higher fluences the crater had the traces of the molten material associated with the presence of the plasma-related mechanism of laser ablation (see details in the Section 2.2.1.2). Numerical simulations confirmed that due to the different ablation mechanisms acting during femtosecond ablation at high fluences, a bimodal size distribution was possible [103].

2.2.1.4 Spot size and focusing conditions

When the size of the spot is increased while keeping the same fluence, the ablation yield rises. Moreover, the experiments on the changing the spot size during the nanosecond ablation demonstrated that the bigger spot size leads to larger nanoparticles and broader size distributions [186]. If more energy is delivered to the surface by increasing the spot size, concentration of the ablated species in a unit volume is higher and the formation of larger particles is favorable. Higher energies also lead to multiple ablation mechanisms yielding broad size distributions.

The positioning of the target about 400 μm before the geometrical focus leads to more intense

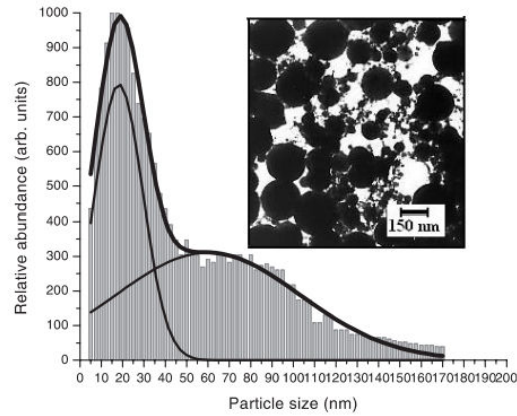


Figure 2.3: Transmission electron microscope image and a corresponding size distribution diagram of the nanoparticles produced by the femtosecond ablation of a gold target (800 nm, 120 fs, 880 J/cm²). From Ref. [57].

plasma and consequently to higher nanoparticles productivity, large particles size and broader size distribution [57]. Under the femtosecond ablation regime one also should take into account the non-linear self-focusing effects (before the geometrical focus), yielding the generation of white-light supercontinuum, which appears as a broad (from UV to NIR) spectrum of the femtosecond length [86]. Further moving of the target from the focal plane decreases the fluence and leads to opposite tendencies for nanoparticles size and size distribution. As a general rule the effects of the spot size and the focusing conditions are tightly related to the incident fluence, and the fluence is of great importance for the plasma intensity, the ablation mechanism, the mean particles size and size dispersion.

2.2.1.5 Repetition rate and number of pulses

It is obvious that higher repetition rates should increase the efficiency of nanoparticles production. However, there is a limitation related to the production of the cavitation bubble. When the interval between two pulses is shorter than the cavitation bubble lifetime, the laser pulse can overlap with it. The bubble causes a strong light scattering and reduces the laser energy reaching the target. Moreover, inside the bubble, there is a low-density gaseous phase. The ablation inside the bubble is similar to the ablation in gaseous phase, for example the plasma confinement effect is limited compared to the ablation in the liquid medium. The cavitation bubble lifetime is about $10^{-4} - 10^{-3}$ s, therefore the maximum repetition rate at which the ablation is not perturbed by a cavitation bubble is 1–5 kHz [143].

The amount of the ablated material increases with the number of laser pulses, but a large number of laser pulses can modify the target (either its morphology or its composition as a result of its interaction with species from a solution) [187]. These two processes are favored by

high temperature and pressure generated during laser ablation process. Therefore, for identical ablation conditions it is essential to continuously move the target in order to avoid the ablation from the same area.

Finally high repetition rates and long ablation time can lead to the increase of local concentration of nanoclusters in a limited volume near the target, which maximizes their coalescence and agglomeration, as well as leads to light scattering and absorption. Typically, these phenomena lead to a broadening of nanoparticles size distribution. However, the problem of the high local concentration of the nanoparticles can be resolved by using a liquid flow cell [184]. At long ablation times formed gold nanoparticles interact with a laser pulses and undergo a laser-induced modification [186]. One can take advantage of the post-ablation laser-induced modification of gold nanoparticles, which often results in smaller nanoparticles with narrow size distribution and enhanced stability.

2.2.1.6 External temperature and pressure

Besides the laser parameters, external factors such as temperature and external pressure have minor influences on the ablation process. Temperature affects the properties of the liquid, such as viscosity, density, refractive index, surface tension and compressibility. In turn, these parameters play an important role in plasma confinement, generation of cavitation bubble and nanoclusters formation. For instance, the variations of the liquid compressibility related to the temperature changes influence the hydrodynamic diameters of gold nanoparticles [197].

2.2.2 Influence of chemical parameters

2.2.2.1 Solvent

Chemical parameters of the system, such as the composition of the surrounding medium, including the nature of the solvent and the presence of solutes, are also of great importance for the manipulation of the nanoparticles properties. In most cases, the ablation is carried out in pure water. The surface of the nanoparticles produced under these conditions is slightly oxidized, containing Au-O⁻ groups and carrying a negative charge that ensures high colloidal stability of the nanoparticles in the absence of other stabilizing molecules [61, 193]. Mafuné *et al.* [193] estimated that 3.3–6.6 % of the surface gold atoms were oxidized in water.

In the case of polar organic solvents, such as ethanol (C₂H₅-OH), tetrahydrofuran (C₄H₈O, THF), dimethylsulfoxide ((CH₃)₂SO, DMSO), acetonitrile (CH₃-CN) and dimethylformamide (HCO-N(CH₃)₂) the produced nanoparticles are usually smaller, while the fraction of the aggregated particles is larger [190, 198]; the stability of the colloids tends to be lower than in the

case of aqueous solutions. Smaller size of the nanoparticles in the case of organic solvents can be explained by the interaction between the growing nucleus and the solvents or by-products, yielding to the inhibition of the nucleus growth and a relatively irregular shape of the nanoparticles. In this case, the irregular shape of the nanoparticles can be due to incomplete coating of nanoclusters, which favors the growth of the nanocrystals only in the direction where the surface remains uncovered.

On the other hand, lower stability of nanoparticles in organic solvents and their lower ζ -potential can be due to the capping of nanoparticles by solvent and by-products molecules. In addition, electrostatic repulsion energy, related to the solvent polarity can influence the growth of the nanocrystals [199]. In particular the mean size of the nanoparticles increased up to 35 nm in polar solvents, such as methanol (CH_3OH) and isopropanol ($(\text{CH}_3)_2\text{CHOH}$), while in less- or non polar solvents like *n*-hexane (C_6H_{14}), toluene (C_7H_8), diethyl ether ($\text{C}_2\text{H}_5\text{OC}_2\text{H}_5$) and acetone the particles size remained unchanged regardless the solvent and did not exceed 10 nm [199].

Giorgetti *et al.* [200] reported that the ablation in the acetone ($(\text{CH}_3)_2\text{CO}$) results in more stable colloids than in other organic solvents, although the process was accompanied by the formation of enolates and amorphous carbon. Such enhanced stability was explained by the complexation of the nanoparticles with enolate anions. On the other hand, ablation of gold target in toluene results in the trapping of the nanoparticles by the by-products of the solvent degradation, if special precautions are not taken [135]. Aromatic solvents are subjected to pyrolysis yielding to graphitic materials when they are heated over 1000 K in the lack of oxygen. Therefore, under the laser irradiation the toluene is decomposed, and produced gold nanoclusters are embedded into a graphitic matrix, resulting in small (around 1 nm) nanoparticles [135]. It is likely that the growth of the nuclei is stopped at the early stages by the rapidly forming graphitic network. When the ablation of the gold target is performed in chloroform (CHCl_3), no metal nanoparticles are formed [190]. Under the high local temperature and pressure induced by the laser irradiation Au reacts with CHCl_3 yielding in AuCl_3 compound.

Nanoparticles generated by the laser ablation in liquid *n*-alkanes, such as *n*-pentane (C_5H_{12}), *n*-hexane (C_6H_{14}), *n*-heptane (C_7H_{16}) and *n*-decane ($\text{C}_{10}\text{H}_{22}$), have a specific elongated form. Besides the shorter carbon chain of the hydrocarbon induces higher aspect ratio compared to longer hydrocarbons [181].

2.2.2.2 Presence of the solutes

Laser ablation in the presence of solutes is another powerful instrument for manipulations of the nanoparticles size. The solutes can influence the nanoparticles formation on different levels. First,

they can change some properties of the liquid, such as viscosity, density and surface tension [201]. Therefore, it can play a role in the formation of the cavitation bubble and in the confinement of plasma near the ablation crater. For example, the enhanced stability of the bubbles can template the formation of the nanoparticles leading to hollow structures [202].

However, the direct interaction of the solutes with the nanoparticles appears to be more important. First attempts to tune the nanoparticles size and properties and improve the stability were based on the employment of surfactants. The classical example used in many works is the sodium dodecyl sulfate (SDS) (see the structure in Figure 2.4) [83, 161, 187, 203]. SDS is an anionic surfactant that coordinates on the surface of the nanoparticles by electrostatic interactions and forms a molecular layer, preventing the coagulation and the growth of the nanoparticles through the adsorption of free atoms or clusters. SDS also improves the stability of the nanoparticles and prevents their agglomeration and precipitation. For example, the addition of SDS at the concentration of 10^{-4} – 10^{-2} M allows one to reduce of the final size of the nanoparticles produced by the ablation from 15–30 to 3–5 nm under a significant decrease of the size dispersion and improved the colloidal stability [187, 203, 204]. Cetyltrimethylammonium bromide (CTAB) is another example of the surfactant used to manipulate the formation of the nanoparticles (Figure 2.4). CTAB belongs to the group of cationic surfactants, but the principle of its interaction with nanoparticles is the same as for SDS. The ablation in 0.1–1 mM aqueous CTAB solutions results in the formation of small (4–6 nm) Au nanoparticles with enhanced stability of their colloidal solutions [205, 206].

The disadvantage of the use of surfactants for the nanoparticles synthesis is their toxicity that restricts the application of the nanoparticles for any biological or biomedical task. To overcome the toxicity issue, Besner *et al.* [63] proposed to perform the synthesis of nanoparticles in the presence of dextran or polyethylene glycol (PEG), which are considered to be completely safe for the living organisms. Interestingly, the presence of the polymers in the solution can influence the size of the nanoparticles. Depending on the concentration of PEG or dextran and its ratio to the amount of gold atoms, the size of the nanoparticles can be tuned between ~ 2 and 80 nm. Similar effect was observed when the ablation of the nanoparticles was performed in the solution of cyclodextrins (Figure 2.4) [64, 207].

The ablation of the bulk gold target in the presence of dendrimers (poly(amidoamine), PAMAM, Figure 2.4) results in the stabilization of sub-nanometer clusters and Au^{3+} ions as a result of their trapping inside the dendrimers cavities [153, 208]. The outer functional groups of the dendrimers allows the formation and stabilization of small 2–5 nm nanoparticles [153, 209].

Laser synthesis of the nanoparticles opens up opportunities for a one-step functionalization

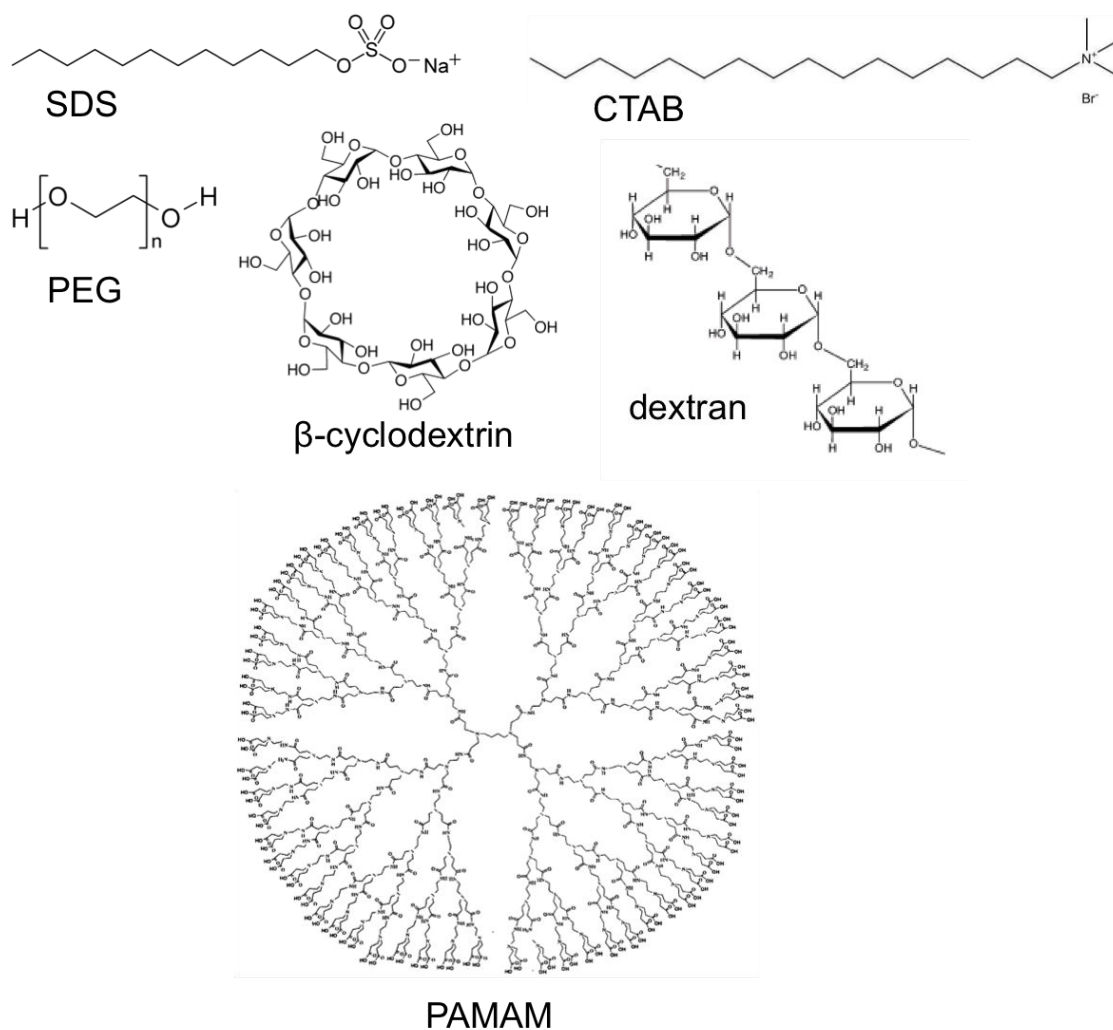


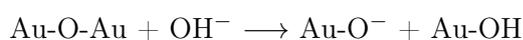
Figure 2.4: Examples of the solutes used for the modification and size control of the gold nanoparticles: sodium dodecyl sulfate (SDS), cetyltrimethylammonium bromide (CTAB), polyethylene glycol (PEG), β -cyclodextrin, dextran, poly(amidoamine) (PAMAM).

and conjugation of the particles with biomolecules. Such approach gives two advantages: first, it enables a direct formation of gold-based bioconjugates, and second, it gives the possibility of the tuning of the particles size and size dispersion due to easy absorption of biomolecules on the surface of the nanoparticles and the inhibition of the seed growth. Thus, small monodispersed Au nanoparticles conjugated with oligonucleotides [210,211] or proteins [65,66,212] were obtained simply by performing the laser ablation of a metallic target in solutions, containing the biomolecules of interest.

Normally the ligands are attached to the nanoparticles surface through the electrostatic interactions. The ligands can also form of chemical bonds with the surface atoms of the nanoparticles. The example of this type of interaction is the nanoparticles capping with thiolated ligands. For instance, the size of the nanoparticles can be reduced down to 2 nm in thiol-alkane solutions [213].

Laser ablation in the presence of the electrolytes offers another possibility for the manip-

ulation of the nanoparticles parameters [61, 66, 183]. The presence of the electrolytes usually destabilizes the nanoparticles solutions, because they screen the nanoparticles charge and break the electrostatic stabilization. However, size reduction and narrow size distributions of the laser-ablated Au nanoparticles were observed at the addition of many electrolytes (Cl^- , Br^- , PO_4^{3-} , $\text{HPO}_4^{2-}/\text{H}_2\text{PO}_4^-$) at low concentrations [66]. Furthermore, at low concentrations, the Cl^- and OH^- can enhance the nanoparticles stability and improve the ablation rate [61]. These results can be explained by a partial oxidation of the surface of gold nanoparticles. Cl^- and OH^- ions react with surface atoms according to the following scheme:



Cl^- and OH^- anions produce a net charge on the surface of the nanoparticles and prevent them from the agglomeration [61]. Moreover, Amendola and Meneghetti [65] used the addition of KCl and THF to aqueous solutions of nanoparticles to induce their controlled agglomeration and thus get larger nanoparticles (up to 50 nm).

2.2.3 Laser fragmentation

Kurita *et al.* [80] first reported the effect of the size reduction of chemically prepared gold nanoparticles after their irradiation with 532-nm nanosecond pulses. The size of the nanoparticles was reduced from 60 to less than 20 nm while the shape of the nanoparticles changed from irregular to almost spherical one [80]. The shape transformation from gold nanorods into spherical nanoparticles was observed under femtosecond [152, 155, 169], picosecond [214] and nanosecond [152, 155, 215] laser irradiation. The dynamics of the shape transformation was studied by Zijlstra *et al.* [156]. They observed a gradual rod-to-sphere metamorphosis from a long and thin rod into shorter and thicker one, which finally collapsed forming a spherical structure. These results demonstrate that under both long and short laser irradiation, and for wavelengths varying from 355 to 1064 nm, gold nanostructures interact with laser pulses while their shape becomes spherical after the fragmentation process.

As it was discussed in Section 2.2.1.3, the nanoparticles obtained by the nanosecond laser ablation of a gold target are often characterized by a limited stability, which is explained by a large size dispersion of the particles. Pulsed laser post-irradiation is a powerful tool to reduce the mean size of the nanoparticles [151, 203] and narrow down the size dispersion in order to improve the stability of the colloids in the absence of any additional reagents [68]. An example of an evolution

of nanoparticles size distribution under laser post-irradiation of colloidal solutions is shown in Figure 2.5. It is important that the size reduction and reshaping laser irradiation take place not only in water, but also in a number of organic solvents, such as DMSO, THF and acetonitrile [198]. The study of Kawasaki and Masuda demonstrated that even micrometric size metallic flakes could be reduced down to 10 nm spherical particles under 532-nm nanosecond irradiation in deaerated conditions, but dissolved oxygen promoted the irreversible coagulation [216].

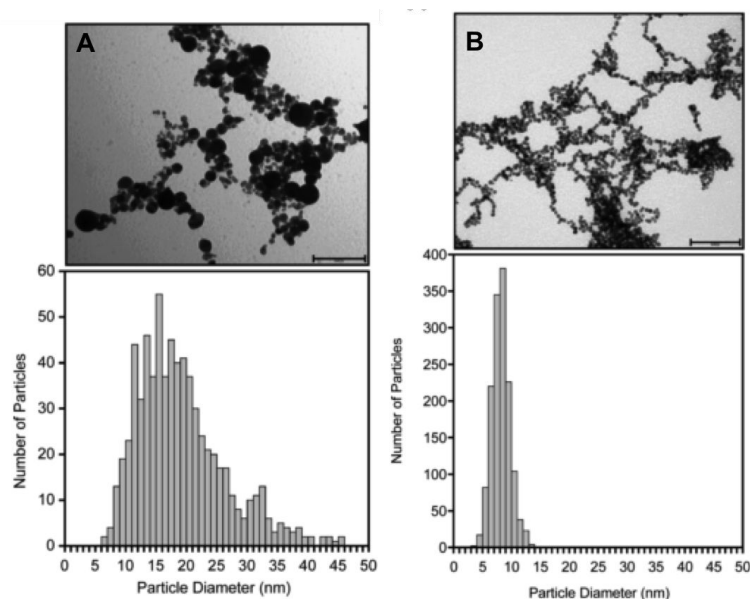


Figure 2.5: Transmission electron microscope images and corresponding size distributions of the gold nanoparticles produced (A) by the nanosecond ablation (1064 nm, 7 ns, 220 J/cm²) in pure water; and (B) the same sample after 120 minutes of 532 nm nanosecond irradiation (532 nm, 7 ns, 24 J/cm²). From Ref. [203].

The choice of the wavelength during the nanosecond fragmentation of the uncapped nanoparticles is of great importance for nanoparticles size manipulations and stability of the resulting nanomaterials. Kim *et al.* [192] demonstrated that the post-irradiation at 355 nm was the most effective to narrow down the size dispersion and hence to improve the stability of the nanoparticles. The post-irradiation at 1064 nm had no visible effect, and the irradiation at 532 nm triggered an aggregation of Au atoms and clusters and significantly decreased the solutions stability [192]. One can see a discrepancy between these results, showing the destabilization of the colloids during the irradiation at 532 nm, and a number of other studies, where a 532 nm second harmonic of a Nd:YAG nanosecond laser is used for efficient size reduction [54, 65, 80, 83, 151, 161, 203]. In reality, second harmonic of the Nd:YAG laser is close to the surface plasmon resonance peak of the Au nanoparticles, and the choice of this wavelength allows the most efficient absorption. Therefore, any variations of radiation parameters (fluence, pulse duration) can have a decisive impact on final size of nanostructures. As an example, Kim *et al.* [192] demonstrated that for

irradiation at 532 nm, the fragmentation process is fluence-dependent, and only the irradiation at the fluence range about 13–20 mJ/cm² induced the aggregation, while at higher and lower fluences no aggregation was observed.

Werner and Hashimoto [217] studied effect of the laser intensity, external pressure and excitation wavelength on the nanosecond fragmentation of 100 nm commercial gold nanoparticles. They tuned the particles size in the range from 30 to 90 nm while keeping them highly monodispersed, with a size variation not higher than 5%. They demonstrated that increase of the laser fluence from 43 to 136 mJ/cm² induced the gradual decrease of the final nanoparticles diameter from 90 to 35 nm. The nanoparticles produced under 355-nm irradiation were slightly smaller compared to ones produced under 532-nm irradiation. For increasing external pressure (from 30 to 100 MPa) higher laser intensities were required to obtain similar particles sizes. The fluence dependence of the nanoparticles size during the fragmentation can be explained by the difference of Au boiling points at different pressures [217].

Surfactants and polymers are often used to tune the nanoparticles size during the fragmentation process. Small (up to 5 nm) nanoparticles with a narrow size distribution could be obtained by the nanosecond fragmentation in SDS solutions. Here, the size control can be achieved by tuning the laser fluence and varying SDS concentration [54, 83, 203]. It was also demonstrated that under certain conditions the SDS-capped gold nanoparticles could aggregate and form wire-like structures and networks after the 532-nm nanosecond irradiation [54, 161, 204].

As we mentioned in the Section 1.3.2.1, the fragmentation under the nanosecond laser irradiation occurs through the photothermal mechanism. It means that after a pulse absorption, nanoparticles gradually pass through the melting and vaporization steps. If “parent” nanoparticles are aggregated, nanosecond laser-induced heating can lead to the annealing and fusion of smaller particles, resulting in the nanoparticles size increase. For example, Amendola and Meneghetti [65] provoked the aggregation of the laser-synthesized Au nanoparticles by the addition of THF and KCl. After consequent nanosecond irradiation (532 nm, 9 ns, 1 mJ/cm²) the mean size of the nanoparticles increased from 18 to 40 nm [65]. Boyer and Meunier [199] demonstrated that the annealing of the laser-generated Au nanoparticles in methanol with an unfocused nanosecond laser beam at 532 nm resulted in nanoparticles growth from 50 to 120 nm. The irradiation with a non-focused 532-nm nanosecond laser beam (532 nm, 8 ns, 40–100 mJ/cm²) of citrate-stabilized gold nanoparticles induces the successive nanoparticles aggregation and fusion, yielding the sub-micron size particles [194]. When capped with thionicotinamide nanoparticles undergo fusion after the first minutes of picosecond 532 nm irradiation, although they get fragmented into smaller particles after 30 minutes [172].

Stable sub-nanometer gold clusters present another family of the nanomaterials that can be generated as a result of laser irradiation of the colloidal solutions. Gold clusters composed of 5–13 atoms possess the properties of the quantum dots and can be strongly fluorescent in blue-green region of the spectrum [218]. Such stable photofragments were detected during the picosecond irradiation (355 nm, 15 ps, 8 mJ/pulse) of dendrimer-capped gold nanoparticles [153,208]. Sub-nanometer particles were also observed after the 532-nm nanosecond irradiation (532 nm, 6 ns, 130 mJ/cm²) of 20-nm chemically prepared Au particles covered with 4-aminothiophenol and dispersed in toluene [153]. Thiolated ligands and inner cavities of the dendrimers are typically required to stabilize such small photofragments.

Laser-induced photothermal melting/vaporization and Coulomb explosion-related fragmentation of metallic particles suspended in water also provide an efficient pathway for alloying of nanoparticles. The irradiation of a mixture of two colloids leads to its instantaneous fragmentation into free atoms and atomic clusters, which can then form alloys during further condensation process. Co-fragmentation of two types of metallic particles can give rise to the formation of alloy nanoparticles of various composition, such as Au-Ag, Au-Pd, Ag-Pd and Au-Pt [180,219–222]. In many cases core-shell structures (Ag@Au, Au@Ag, Fe@Au and Pt@Au) are formed instead of alloys [223–225].

In contrast to nanosecond laser case, the fragmentation with femtosecond pulses is based on the mechanism of Coulomb explosion, which implies an ejection of electrons from the nanoparticles and the formation of a positive charge at the nanoparticle lattice. When the charge repulsion forces exceed the surface tension, the particle explodes into multiple smaller fragments. At the picosecond regime, usually two mechanisms are possible depending on the laser energy. In particular, 355-nm picosecond irradiation (30 ps, 14–43 mJ/cm²) of gold colloids results in a bimodal size distribution with two peaks, one at 6 nm and another at 16–24 nm [157].

Femtosecond laser fragmentation (800 nm, 140 fs, 500 μJ/pulse) induces the reduction of the mean nanoparticles size from 30–120 to 20–30 nm with a narrow size distribution and enhanced stability [81,82]. The size of the nanoparticles after the femtosecond laser treatment depends strongly on the presence of chemical species. The addition of polymers such as dextran or PEG during the femtosecond fragmentation procedure makes possible a precise tuning of the nanoparticles size from 2 to 70 nm [63,81].

Interestingly, the femtosecond laser fragmentation is possible for NIR pumping wavelengths, while 1064-nm irradiation has no effect on gold nanoparticles during the laser treatment with nano- and picosecond pulses [153,192]. It is known that 5-100 nm nanoparticles have a strong absorption in the visible range around 520-560 nm due to the excitation of the surface plasmons,

while their absorption at wavelength longer than 700 nm is negligible. Therefore, the most works the post-irradiation the modification of Au nanoparticles were carried out using the second harmonic of Nd:YAG laser (532 nm) corresponding to the plasmonic absorption band or the third harmonic of Nd:YAG laser (355 nm) corresponding to the interband transition of gold. However, in the case of 800-nm femtosecond irradiation, the phenomenon of supercontinuum can provide white light spectrum, in particular in the region of plasmon-related absorption.

2.3 Materials and methods

2.3.1 Materials

Gold and platinum foils, 99.95% pure, used in our experiments as solid targets were purchased from GoodFellow. Polyethylene glycol (PEG, molar mass 20000), dextran from *Leuconostoc spp.* (molar mass 40000), β -cyclodextrin were purchased from Sigma-Aldrich. All the solutions were prepared with 18 M Ω deionized water.

2.3.2 Ablation from the bulk target

The scheme of an experimental set-up used both for the ablation and fragmentation experiments is presented in Figure 2.6. A target (10×10 mm and 2 mm thick in the case of Au, 10×10 mm and 0.5 mm thick in the case Pd) was placed on the bottom of a vessel filled with deionized water. The level of the liquid above the target was kept about 10 mm. The vessel was placed on a translation stage that performed the movement in XY-direction, perpendicular to the laser beam. The target was moved at a speed of 0.75 mm/s to avoid the ablation from the same area. The position of the target was adjusted with a micrometric screw to find optimal focal conditions. To determine the amount of the ablated material the target was weighted before and after the ablation with a microbalance.

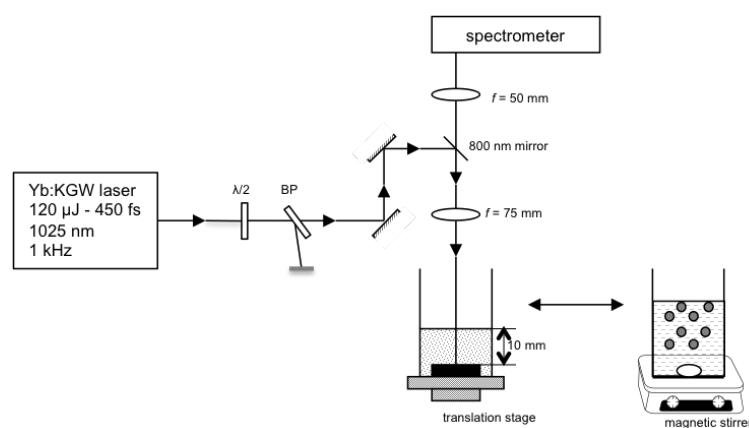


Figure 2.6: Scheme of the experimental set-up. $\lambda/2$ – half-wave plate; BP – Brewster polarizer.

We used an S-Pulse Yb:KGW (ytterbium-doped potassium-gadolinium tungstate) femtosecond laser (Amplitude Systems) to ablate the target. The laser operated at the fundamental wavelength of 1025 nm, the pulse duration was 450 fs, and repetition rate was 1 kHz. The laser beam with an initial diameter 2.3 mm was focused slightly below the target surface with a 75 mm lens. Pulse energy used during the ablation was 120 $\mu\text{J}/\text{pulse}$.

2.3.3 Laser fragmentation and alloying

Colloidal solutions obtained after the ablation from the target were transferred into a quartz cuvette. The same laser beam (450 fs pulse width, 1025 nm, 1 kHz repetition rate) was focused with a 75 mm lens into the center of the cuvette (unless specifically mentioned) filled up with the colloidal solutions, while the solution was stirred with a magnetic stirrer to homogenize the ablation process. The scheme of the set-up used for the fragmentation step is illustrated in Figure 2.6. We varied the laser energy from 5 to 120 $\mu\text{J}/\text{pulse}$ with a half-wave plate.

2.3.4 Measurements

In order to study the phenomena accompanying the laser ablation process, we recorded the supercontinuum spectra with a spectrometer Ocean Optics HR2000+CG-UV-NIR placed above the cuvette, as it shown on the scheme (Figure 2.6). The formation of the cavitation bubble was detected by the acoustic wave generated when the bubble collapses. The acoustic signal was registered with a microphone immersed into the solution.

Transmission electron microscopy (TEM) and high resolution TEM (HRTEM) measurements were performed using JEOL JEM 3010 system operating at 300 kV. A drop of freshly prepared solution was placed onto a carbon-coated copper grid and dried at ambient conditions before the examination by TEM. To calculate size-distribution diagrams for each sample an overall 1000 particles were analyzed with Image-Pro Plus software. Dynamic light scattering (DLS) measurements were additionally performed using a Zetasizer Nano ZS instrument at 25 °C in order to determine nanoparticles size characteristics in the solution. Absorbance spectra was measured with a Varian Cary Win UV-Vis spectrometer. Fluorescence spectra were registered with a Varian Cary Eclipse fluorometer. Fluorescence excitation and emission slits were 5 mm; the measurements were taken in 1 cm path length quartz cells.

2.4 Laser synthesis of gold nanoparticles

2.4.1 Ablation from a bulk target

The formation of the nanoparticles during the ablation process was visible as reddish plume. The visible coloration of the solution occurred within a few minutes. The resulting solution was deep red with yellow metallic tints, as it is presented in Figure 2.7. Yellow tints are usually associated with relatively broad size distribution of nanoparticles. The solutions were stable, but after several days of storage we observed some precipitation.



Figure 2.7: Colloidal solution of the gold nanoparticles obtained after the ablation from a bulk target.

We used a fundamental laser wavelength (1025 nm), which is relatively far from plasmonic absorption band of Au nanoparticles. The production rate in our conditions was 15.6 $\mu\text{g}/\text{min}$ when we used the laser energy of 120 $\mu\text{J}/\text{pulse}$ or 15 J/cm^2 of laser fluence at the focal spot (for a lens with the focal distance of $f = 75$ mm). Such production rate is comparable which was previously reported for 800-nm femtosecond laser ablation (13.2 $\mu\text{g}/\text{min}$ at repetition rate of 1 kHz) [184].

In our experiments we irradiated the target with a femtosecond laser beam having the energy of 120 μJ at 1 kHz repetition rate. Therefore, overall 7.2 J of energy was delivered to the system per minute, which corresponds to the ablation efficiency of 2.17 $\mu\text{g}/\text{J}$. Such efficiency of the femtosecond ablation from a metal target is higher than the one of pico- and nanosecond ablation regimes, which do not exceed 1.5 $\mu\text{g}/\text{J}$ [184] and 0.9 $\mu\text{g}/\text{J}$ [89] respectively. Higher production efficiency is typical for femtosecond laser ablation, which is characterized by a higher intensity compared to nano- and picosecond ablation cases ($10^{12} - 10^{14}$ W/cm^2 vs. $10^9 - 10^{12}$ W/cm^2). In addition, femtosecond laser pulse does not interact with generated plasma, and pulse energy is not absorbed or scattered by this phenomenon. Nevertheless the efficiency of the ablation

in water is 4–20 times lower compared to this parameter in the case of ablation in air [226]. It should be noticed that during the ablation in liquids, plasma confinement effects are more important than in gaseous phase.

A TEM microphotograph and corresponding distribution diagram for the nanoparticles prepared by a direct ablation from a gold target in deionized water are presented in Figure 2.8. One can see that the particles form two populations with a mean size around 7 and 29 nm. A bimodal size distribution is typical for the ultrafast laser ablation at high fluences due to multiple competing ablation mechanisms [56, 60].

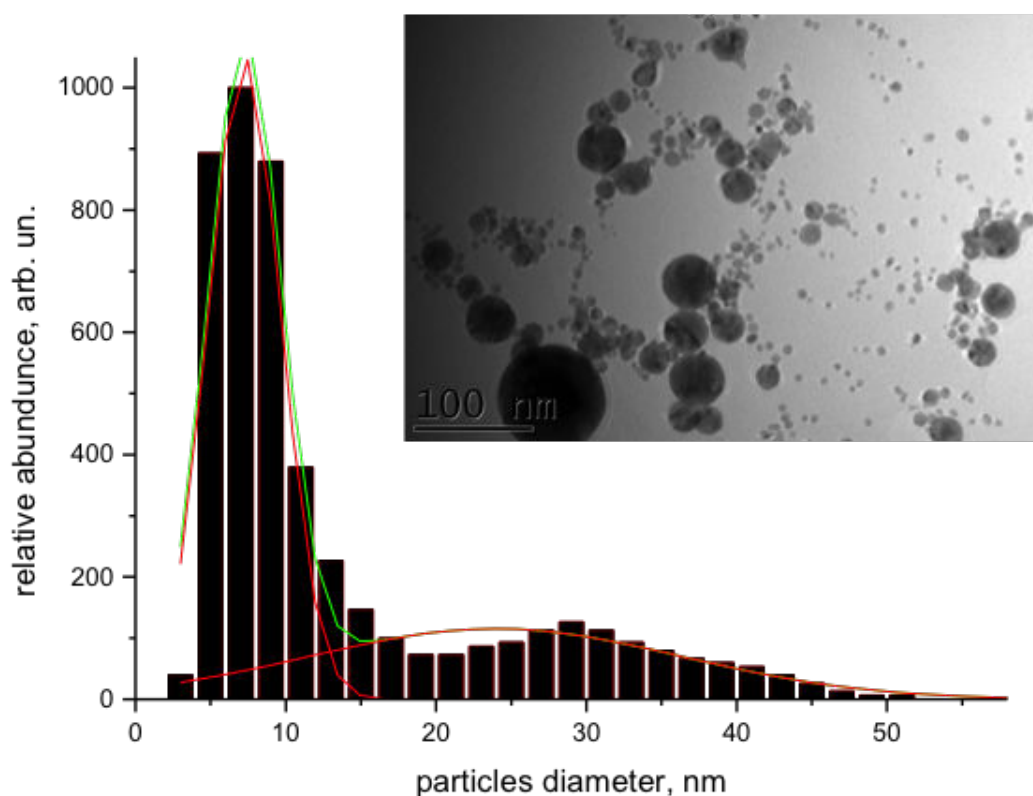


Figure 2.8: TEM microphotograph and a corresponding size distribution diagram for the gold nanoparticles obtained by the ablation from a bulk target.

2.4.2 Laser fragmentation

2.4.2.1 Size and structure of the nanoparticles prepared after the laser fragmentation

We performed the fragmentation of gold nanoparticles at different incident laser energies varying from 5 to 120 $\mu\text{J}/\text{pulse}$ that corresponds to 0.63–15 J/cm^2 of fluence. The typical TEM images and corresponding size distribution diagrams of the nanoparticles after the fragmentation of

various laser energies are presented in Figure 2.9. At low pulse energies (below 65 $\mu\text{J}/\text{pulse}$) the particles diameter was in the range of 7–10 nm, while the standard deviation did not exceed 70% of the mean particles size. As the TEM microphotographs illustrate (Figure 2.9(A) and (B)) the nanoparticles have regular spherical shape. The increase of the pumping energy over 70 μJ led to the increase of the nanoparticles size up to 40–50 nm, while the size dispersion remained at the level of 40–60% (Figure 2.9(C)). After further increase of the incident laser energy above 85 μJ , the particles size decreased down to 20–25 nm, and the size dispersion did not exceed 70% (Figure 2.9(D)). Besides, the fragmentation at high laser energies influenced the morphology of the nanoparticles. The resulting nanoparticles were of irregular shapes; they were linked together through the nanowires, forming gold nanonetworks (Figure 2.9(D)). The resulting solutions were reddish-violet, but they were stable and did not precipitate or agglomerate within several months. Similar structures were previously observed during the fragmentation of the nanoparticles in the nanosecond regime in SDS solutions [161]. In our experiments we obtained stable nanonetworks of bare gold in pure water.

Our experiments also showed that the formation of spherical nanoparticles and nanonetworks was reversible if one properly selected pumping laser energy. As shown in Figure 2.10, after the irradiation of the solution containing gold nano-networks (obtained at 115 μJ) with the laser beam at 55 μJ , the particles were transformed into regular-shaped spheres with mean size 9 ± 3 nm. After the treatment of this solution once again with laser radiation with energy of 115 μJ , the spherical particles were again transformed into nanonetworks. Notice, that even the particles of irregular shape are stable throughout the storage at ambient conditions. The interchanges between spherical nanoparticles and nanowires can be easily made throughout several cycles without affecting the size distribution or stability of the nanoparticles.

Figure 2.11(A, B) summarizes the dependence of nanoparticle size characteristics on energy of laser pulse applied for the fragmentation process. One can see that the values of mean size and size dispersion (in full width at half maximum, FWHM) follow the same tendency, while the size dispersion does not exceed 70% of the mean size for the whole range of laser energies. Such weak size dispersion looks as one of advantages of femtosecond laser fragmentation over most other laser-ablative and chemical synthesis pathways. Based on the analysis of plots depicted in Figure 2.11 and the morphology of the produced nanoparticles, one can distinguish three regimes of laser fragmentation:

- 10-70 $\mu\text{J}/\text{pulse}$: generation of small nanoparticles (less than 10 nm), size is independent from the pumping laser energy;
- 70-90 $\mu\text{J}/\text{pulse}$: ascending growth, size of the particles increases rapidly with the increase

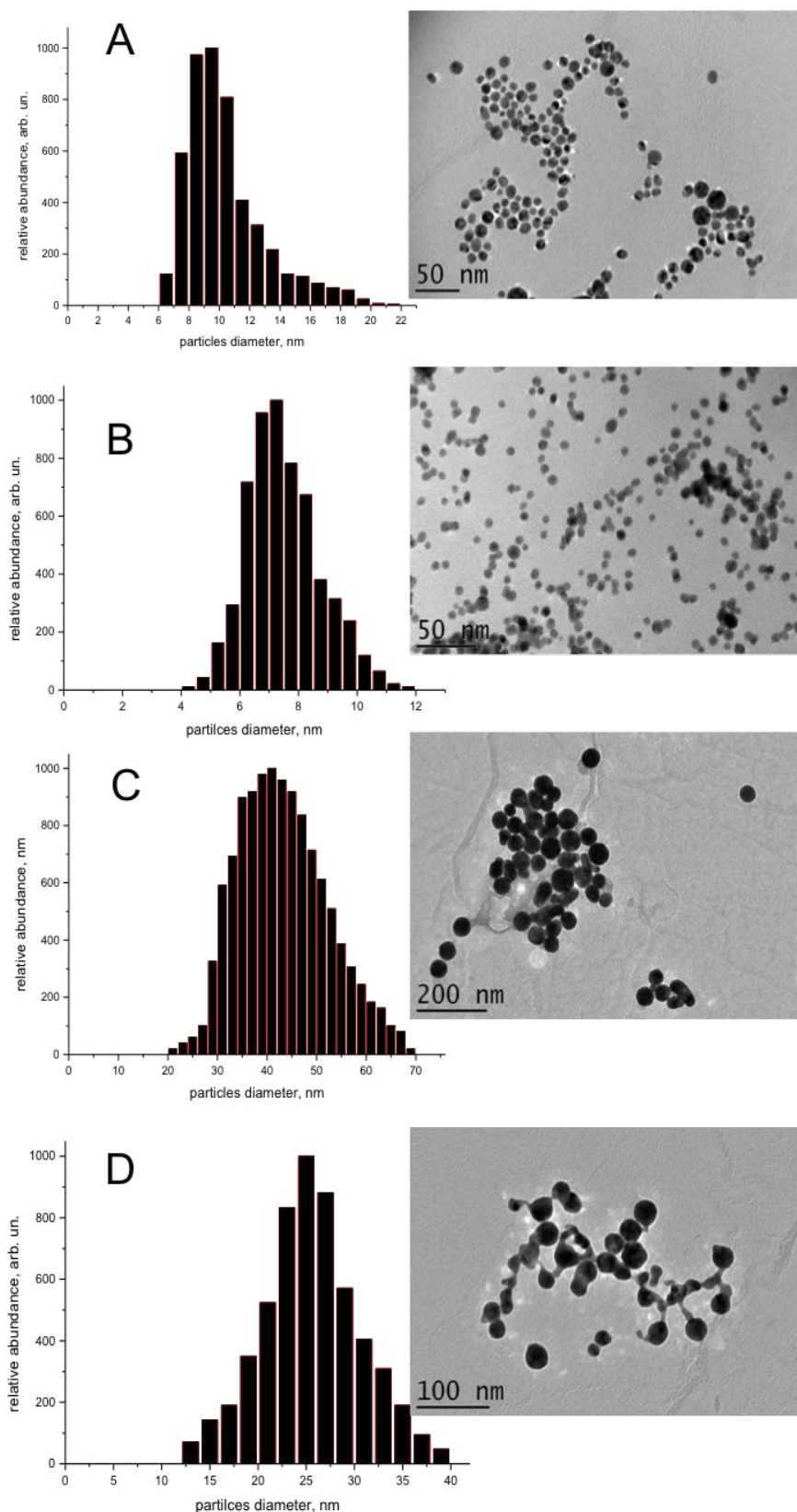


Figure 2.9: Typical TEM images of the nanoparticles and corresponding size distribution diagrams after the fragmentation at 11.5 (A), 55 (B), 85 (C) and 109 (D) μJ of the input laser pulse energy.

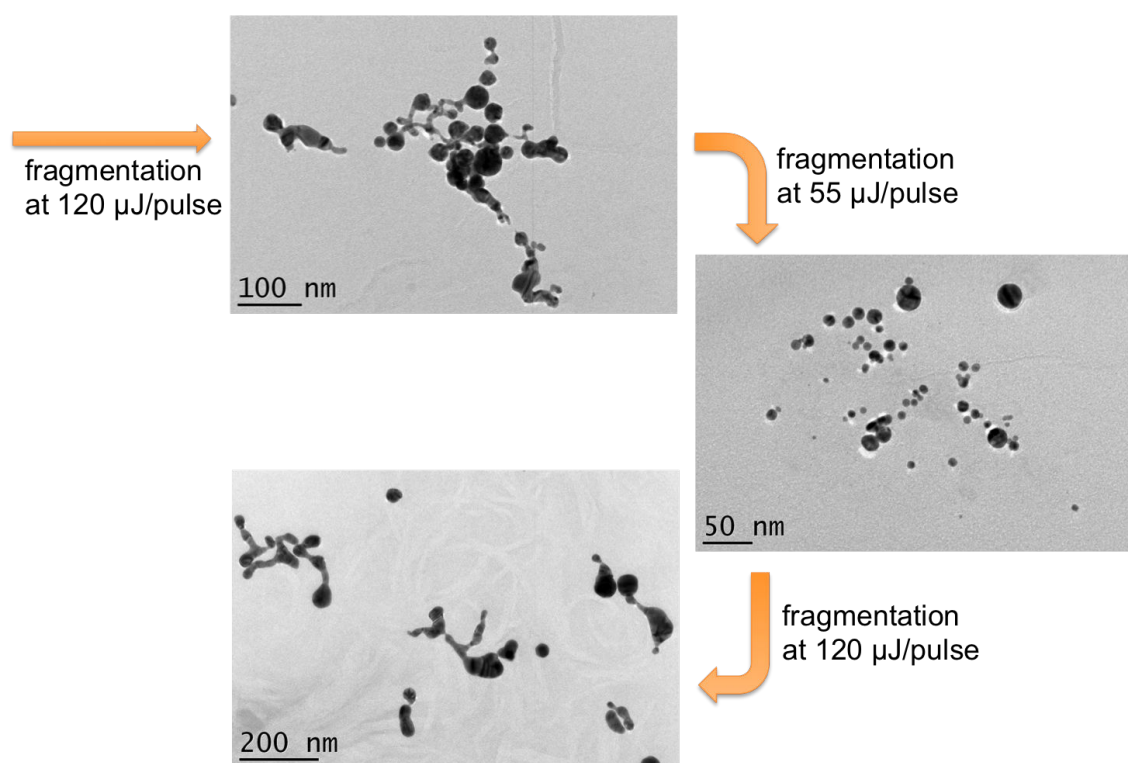


Figure 2.10: TEM microphotographs and the scheme of the reversible changes of the nanoparticles structure after the fragmentation at 120 and 5 $\mu\text{J}/\text{pulse}$.

of the laser energy;

- $>90 \mu\text{J}/\text{pulse}$: descending growth, size of the particles decreases with the increase of the pulse energy. This regime also involves the modification of the morphology of the nanoparticles, suggesting the existence of the additional nanoparticles treatment mechanism.

It is important that despite the existence of different regimes associated with the involvement of different fragmentation mechanisms, we were able to efficiently control nanoparticle size characteristics in the absence of reactive chemical species by varying a purely physical parameter (laser energy).

2.4.2.2 Effects accompanying the fragmentation

To clarify mechanisms responsible for different fragmentation regimes, we examined various phenomena, which accompany the interaction of ultrashort laser radiation with liquids. As we discussed previously (Section 1.3.1), the propagation of the laser pulse in water is often accompanied by two phenomena. The first one is the generation of the supercontinuum. The critical peak power for the generation of the supercontinuum is 4.4 MW [150] that corresponds to 2.1 μJ of the pulse energy for the 450 fs laser pulses. In our experiments we always observed the formation of the supercontinuum even with the naked eye as a white spot with rainbow circles on

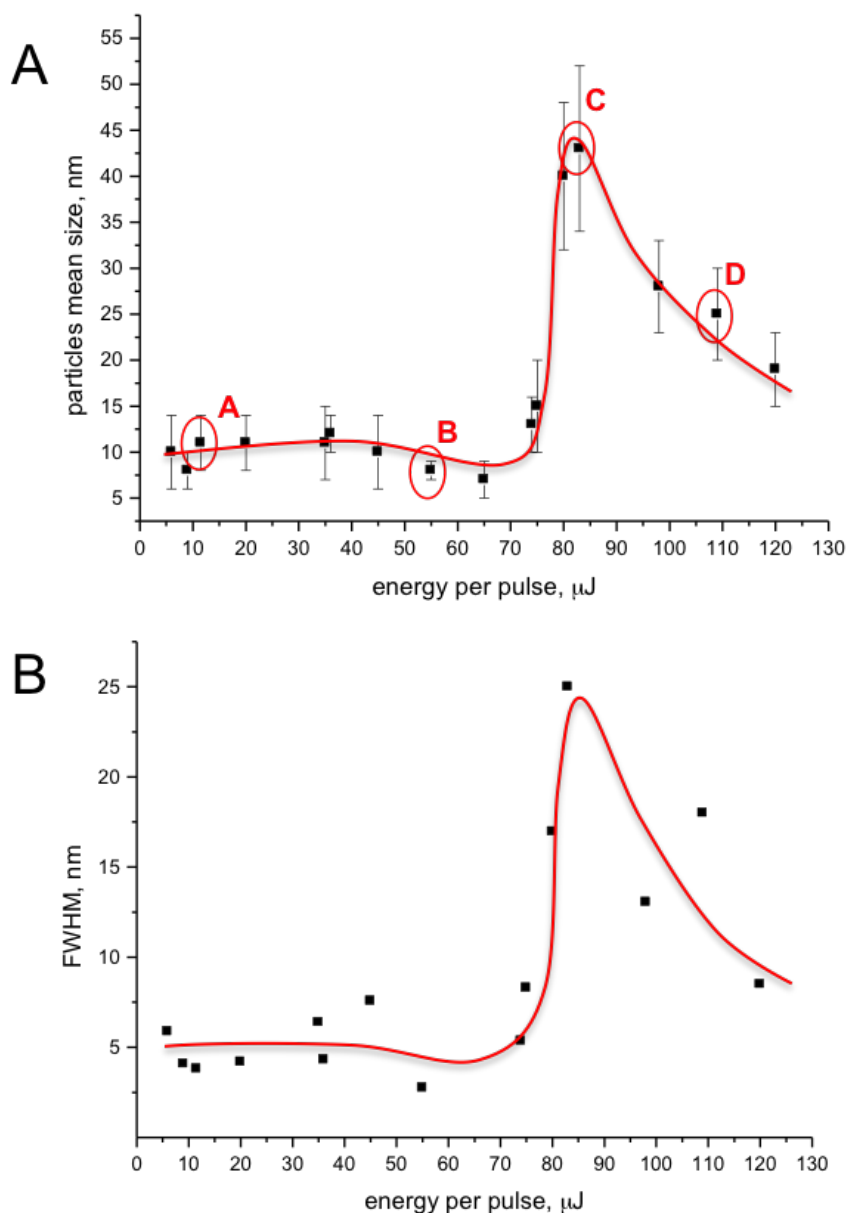


Figure 2.11: (A) The mean size of the nanoparticles after the laser fragmentation as a function of the input laser energy; the error bar corresponds to the standard deviation. The points corresponding to the images and size distribution diagrams in Figure 2.9 are marked with circles. (B) Size dispersion (in FWHM) of the size distribution of the nanoparticles after the fragmentation as a function of the input laser energy.

the black screen behind the vessel. We recorded white light for the whole range of used energies, the total emission increased with the increase of the energy pulse and stabilized for the energies about 65–70 $\mu\text{J}/\text{pulse}$.

As the Figure 2.12(A) demonstrates, the spectrum of the supercontinuum in pure water (black line) has a wide spectral band ranging from 400 to 900 nm. While the plasmon-related absorption of gold nanoparticles is situated at 520–530 nm (red curve) and it is far from the

fundamental wavelength of the laser, it appears to be within the supercontinuum spectrum. As one can see, in the presence of Au nanoparticles the spectra contain a dip ranging from 450 to 630 nm, which gives an evidence of the nanoparticles absorption in this range.

The spectra of the supercontinuum generated in the particles solution, registered in the real time during the fragmentation process, allowed us to calculate the nanoparticles extinction spectra and see its evolution in time. As it is shown in Figure 2.12(B) the fragmentation process leads to a relative increase of absorption at 450 nm (A_{450}) compared to the surface plasmon resonance absorption (A_{SPR}). The increase of the ratio A_{450}/A_{SPR} is typically attributed to the decrease of the mean size of the nanoparticles [227]. Another important feature consists in the shift of the maximum of the absorption from 528 to 515 nm after 30 minutes of the fragmentation. Such a blue shift of a plasmonic peak is also usually attributed to a decrease of the particles size [228]. Our TEM measurements confirmed this tendency evidencing the reduction of the mean nanoparticles size from ~ 30 to 8 nm. Figure 2.13 illustrates how the values of A_{450}/A_{SPR} and A_{528}/A_{515} evolve in time. The most remarkable changes in spectral characteristics of the nanoparticles occur within the first 7 minutes of the fragmentation, and there are practically no changes after 25 minutes of the laser irradiation, thus we can consider that 30 minutes of the irradiation is enough to subject all the nanoparticles to the fragmentation.

As follows from Figure 2.12(A) our experiments with 1025 nm fundamental harmonic were accompanied by the efficient generation of the supercontinuum. Furthermore, supercontinuum spectra are clearly modified when the nanoparticles present in the solution evidencing the absorption process. As it was claimed earlier [81, 82] and then confirmed independently in the Ref. [229], the fragmentation of the nanoparticles under the femtosecond irradiation at 800 nm occurs due to the supercontinuum generation. It was demonstrated that the absorption of the broadband white light could be 24 times more efficient than the absorption of the main harmonic at 800 nm [82]. Taking into account that 1025-nm fundamental harmonic is even further from the plasmonic absorption band of Au nanoparticles than 800-nm wavelength of the Ti:Sapphire laser, we may state that the supercontinuum-based absorption can take place in our experiments.

Optical breakdown is another phenomenon taking place during the propagation of the laser pulse in the liquid. As we discussed in Section 1.3.1 this phenomenon is related to the absorption of light energy by the liquid yielding the plasma generation. The energy of the plasma is then transferred to the liquid leading to its vaporization and the formation of the cavitation bubble [149]. The bubble expands, and when temperature inside the bubble and the inner pressure decrease to the values lower than the surrounding liquid, the bubble collapses at a microsecond timescale (after the laser pulse) [148, 149]. The collapse of the cavitation bubble releases a

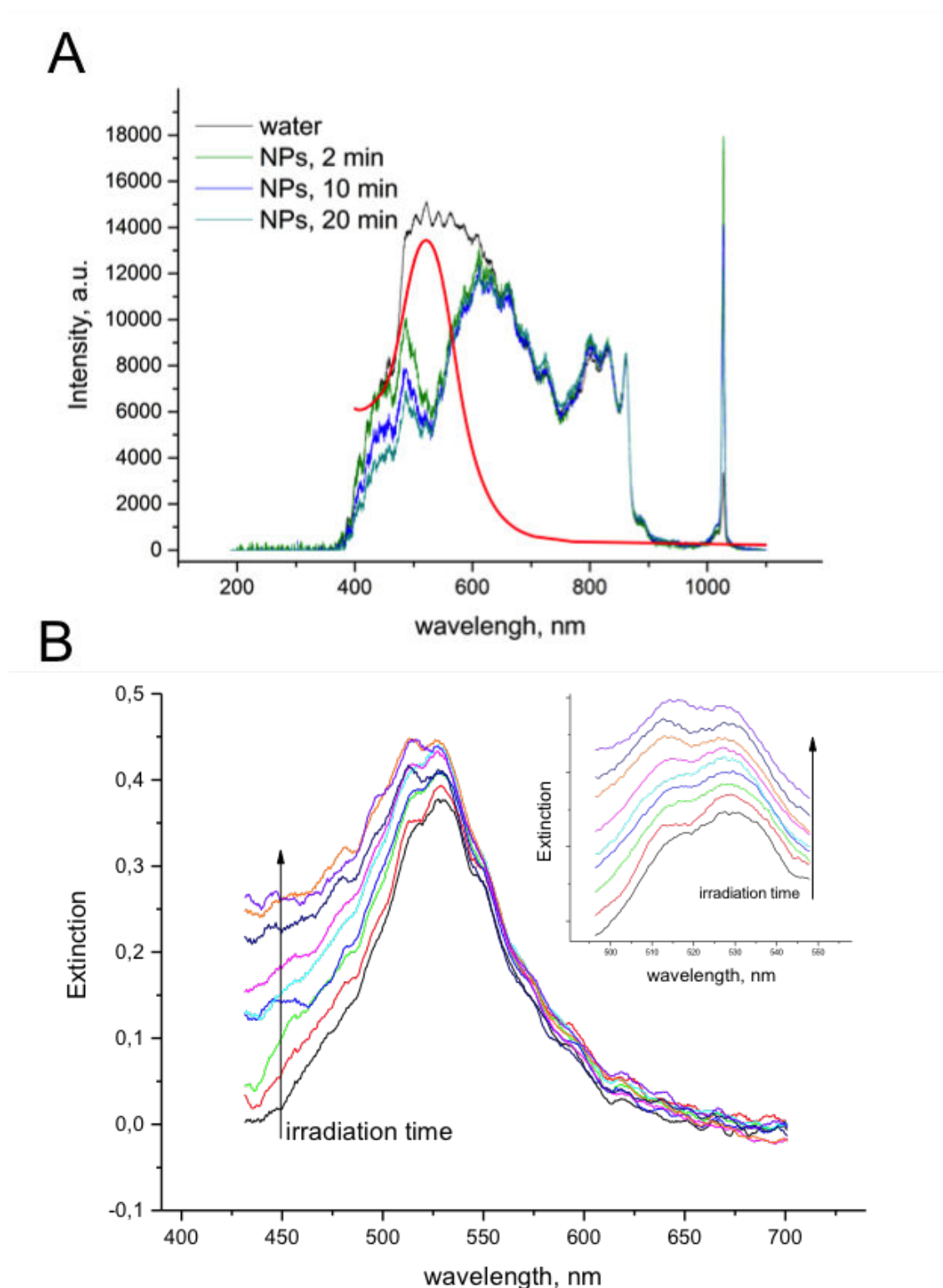


Figure 2.12: A. Spectra of the supercontinuum generated in pure water (black) and in gold colloids, recorded after 2, 10 and 20 min of the laser irradiation; typical absorption spectrum for 20-nm gold nanoparticles is presented in red. B. Extinction spectra of gold colloids calculated from the spectra of supercontinuum recorded after 2, 4, 6, 8, 10, 15, 20, 25 and 30 min of the irradiation. The inset represents a closer look at 500–550 nm region; the spectra in the inset are shifted over the Y-axis for clarity.

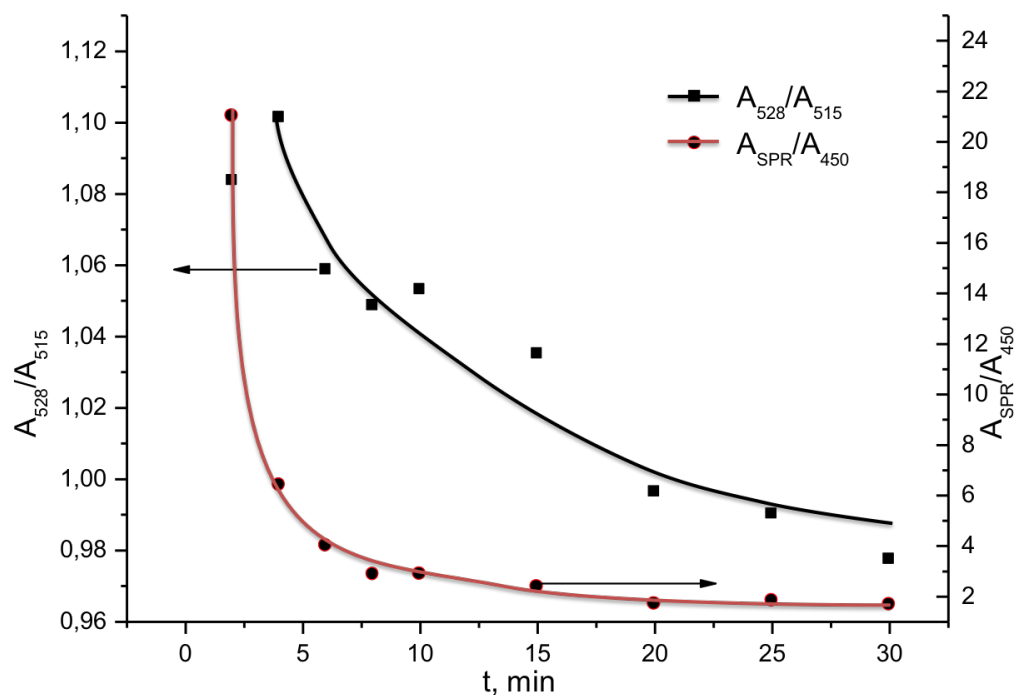


Figure 2.13: Evolution of the absorbance spectra of Au nanoparticles during the fragmentation as a function of irradiation time.

huge amount of energy and thus provides a secondary mechanism of the nanoparticles ablation [56, 57, 60]. The collapse of the cavitation bubble is normally accompanied by the generation of acoustic noise, which can be registered by a microphone [57]. Indeed, we registered with a microphone an acoustic signal, and we detected the signals at high frequencies of 9–20 kHz, that are normally associated with the collapse of the cavitation bubble [230]. The spectrum of the sound registered during the propagation of the laser pulse in water at the pulse energies 5–60 $\mu\text{J}/\text{pulse}$ is presented in Figure 2.14. The acoustic signal was recorded starting from energies of 7 $\mu\text{J}/\text{pulse}$ and then gradually raised and saturated at 85–90 $\mu\text{J}/\text{pulse}$. As far as the effects associated with the optical breakdown were observed throughout the fragmentation process, we can suppose that the plasma- and cavitation-related phenomena might affect the formation and modification of the nanoparticles.

2.4.2.3 Possible mechanisms of femtosecond laser fragmentation

It is known that 5–100 nm Au nanoparticles have a strong absorption in the visible range around 520–560 nm due to the excitation surface plasmons, while the their absorption at longer wavelengths (>650 nm) becomes negligible (see an example of absorption spectrum for 20 nm nanoparticles in Figure 2.12(A)). Since fundamental harmonics of most popular femtosecond

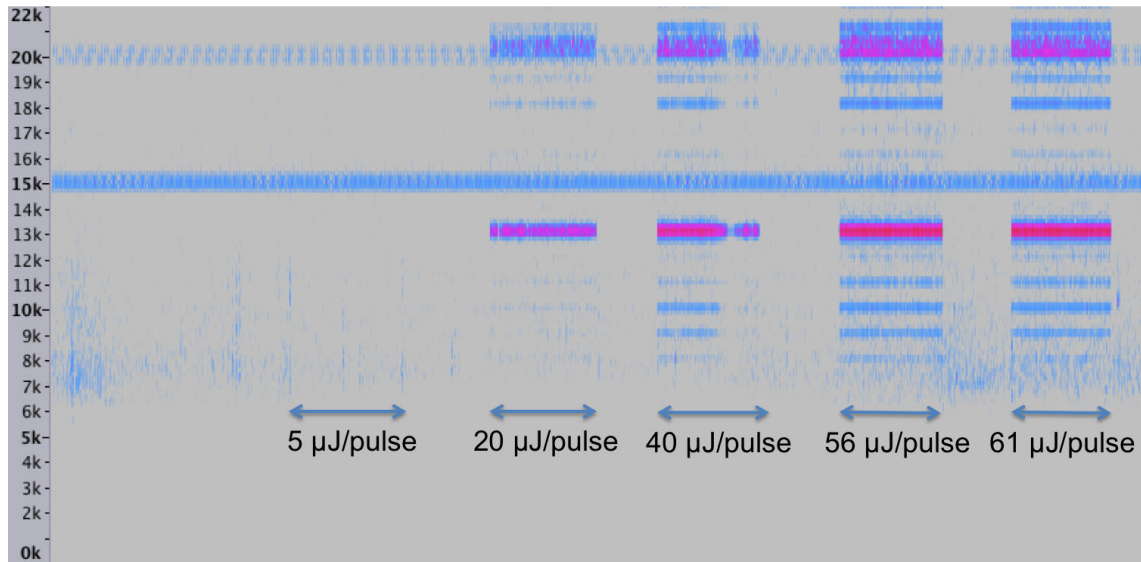


Figure 2.14: Spectrum of the acoustic signal registered during the propagation of the laser pulse in water at different laser pulse energies.

lasers (Ti:Sapphire laser: 800 nm; Yb:KGW: 1025 nm) are far from the plasmon-related absorption, the direct absorption light by the nanoparticles looks hardly probable. The light absorption mechanisms during Ti:Sapphire fragmentation were considered in detail in Refs. [81,82] and then independently verified in Ref. [229]. It was concluded that the absorption at the fundamental harmonic is possible only if the colloids coagulate to form quasi-nanorod structures that often takes place during the first laser ablation step [82]. However, these coagulated structures typically water-disperse after the very first moments of the fragmentation process, while separated nanoparticles cannot absorb radiation at main radiation harmonic (second harmonic and multiphoton absorptions were also found to be negligible [81, 82]). Nevertheless, it was found that the nanoparticles can still efficiently absorb white supercontinuum generated during the propagation of femtosecond laser pulse in water [82,229]. Indeed, depending on the initial laser energy and, focusing geometry up to 10% of the laser energy is transformed in the spectral band of 400–650 nm [81]. Under these conditions, the absorption of the broad-band white light can be 24 times more efficient than the absorption of main harmonic at 800 nm [82]. As follows from Figure 2.12(A), our experiments with 1025 nm fundamental harmonic were also accompanied efficient generation of supercontinuum. Furthermore, we could clearly observe modifications in the supercontinuum spectrum due to the presence of nanoparticles (Figure 2.12(B)), evidencing the absorption process. Taking into account that 1025-nm fundamental laser harmonic is ever further from plasmonic absorption band of Au nanoparticles than the 800-nm wavelength of the Ti:Sapphire laser, we may state that the supercontinuum-based absorption could indeed be one of the main mechanisms.

Optical breakdown is expected to provide another possible mechanism of nanoparticle fragmentation. The breakdown in water may take place under certain laser energy and focusing conditions, yielding to the production of hot laser-induced plasma. Due to a relatively high hydrodynamic pressure, the plasma region generates a shock wave and gradually transmits its energy to the liquid. Such energy transfer leads to a liquid vaporization and the formation of the cavitation bubble, which finally collapses 10–100 μs after the beginning of the laser pulse [149]. Here, one can suppose the fragmentation or modification of nanoparticles by the absorption of thermal energy during the plasma ignition stage or mechanical energy during the collapse of the cavitation bubble. In this case the superheated surface of the nanoparticles can enhance the cavitation effects.

As soon as energy is transferred to nanoparticles, they experience fragmentation and further re-growth. As we discussed in Section 1.3.2, three possible scenarios are typically considered. First is the concept of photothermal melting-evaporation proposed by Koda *et al.* [151]. This mechanism consists in consequent heating, melting and evaporation of the particles when the temperature reaches the boiling point due to photothermal effects. Such mechanism is relevant for long pulse duration (nanosecond) and low pulse energies [158]. Another possible mechanism is near-field ablation; it presumes that plasmonic near-field enhancement causes the nanoparticles fragmentation due to intense electric fields [168]. Third concept is Coulomb explosion of a gold nanoparticle as a result of particle–pulse interaction. This model implies the quick ejection of a large number of electrons and a formation of multiple charged nanoparticles. Charged nanoparticles then undergo fission due to the charge repulsion. This mechanism is typically considered as dominant for the femtosecond fragmentation [166]. The absence of medium-size nanoparticles gives an indirect evidence for the Coulomb explosion mechanism in our experiments.

We can distinguish three regimes of the fragmentation, described in the Section 2.4.2.1. At laser energies below 80 μJ the fragmentation occurs only due to the direct interaction of the nanoparticles with white light supercontinuum. Nanoparticles absorb white light of the supercontinuum and ~ 100 ps after the pulse the fragmentation takes place according to the Coulomb explosion mechanism, followed by the re-nucleation of nanoclusters in the surrounding medium. The fragmentation under this regime is characterized by a small nanoparticles size (< 10 nm) and weak size dispersion. We believe that such “fine” fragmentation is due to supercontinuum-based ablation. In contrast to fundamental radiation harmonics, white light of supercontinuum can irradiate the solution in the whole experimental cuvette, creating uniform conditions for nanoparticle fragmentation in a large volume area and thus offering “fine” fragmentation regime. As the pulse energy increases, the efficiency of the optical breakdown becomes more important. Our tests

showed that at laser energy of $85 \mu\text{J}/\text{pulse}$ the sound intensity reaches its maximum, suggesting the maximization of cavitation-related phenomena. As shown in Ref. [136] for solid target geometry, the cavitation bubble can play an important role in the generation of nanoparticles. The nanoparticles can be trapped inside the bubble to initiate a secondary nucleation, yielding to the formation of large 40–60 nm aggregates [136]. It seems that our fragmentation experiments involve the same mechanism of secondary nucleation inside the bubble. Indeed, the enhancement of cavitation phenomena at energies about $80\text{--}85 \mu\text{J}/\text{pulse}$ leads to a gradual increase of nanoparticle size from 8–10 to 40–45 nm, which roughly corresponds to numbers recorded in Ref. [136]. It should be noted that in contrast to solid target case laser fragmentation uses 3D ablation geometry [178], which should favor the penetration of clusters into the bubble, as well as the release and faster cooling of the formed aggregates. At very high energies ($>90 \mu\text{J}/\text{pulse}$) we evidenced the third fragmentation regime, which was characterized by a decrease of the nanoparticles size and assembling of particles into nanowires and nanonetworks (Figure 2.9(D)). Usually the mechanism of formation of similar structures involves the aggregation of thermally excited nanoparticles and small fragments emitted in the course of the fragmentation, giving evidence for the involvement of thermal phenomena in laser-induced plasma. As the cooling of plasma region can take up to few μs [148], the plasma-trapped nanoparticles can undergo surface melting and sintering [231].

It is important that due to the combination of different phenomena taking place during the propagation of femtosecond pulse in liquid, we can control mean particles size without using any ligands. Since the coexistence of the optical breakdown and supercontinuum generation is conditioned by the focusing geometry, one can have the opportunity for the purely physical size control of the nanoparticle growth.

2.4.3 Capped gold nanoparticles

2.4.3.1 PEG- and dextran-covered gold nanoparticles

The nanoparticles capped with biocompatible polymers demonstrated narrow monomodal size distribution even after the ablation from the solid target in a solution of the polymers, without the fragmentation step. The conditions for the ablations were the same, as for the fabrication of the nanoparticles in pure water. In order to obtain polymer-capped nanoparticles, the ablation was performed in diluted solutions of PEG (M.W. $\sim 20\,000$) and dextran (M.W. $\sim 40\,000$). The solutions after the ablation were deep red, without characteristic yellow metallic tints, which we observed after the ablation in pure water (Figure 2.15). The absence of the yellow tints usually indicates the narrow size distribution. The prepared solutions were stable, and did not show

any signs of the precipitation or agglomeration within several months of storage at the ambient conditions. As it is shown in Figure 2.16 the nanoparticles prepared in the solution of PEG and dextran were spherical, with mean nanoparticles size 4–10 nm for PEG solutions and 15–25 nm for dextran solutions. Notice that nanoparticles prepared in the solutions of the polymers are smaller than those prepared in pure water under identical conditions. Moreover, they exhibit monomodal narrow size distribution even without the fragmentation step. These results can be explained by the interactions between the polymers and nanoparticles that inhibit the seed growth, thus leading to the decreasing of nanoparticles diameter, narrowing the size dispersion and eventually to the improvement of stability of the nanoparticles solutions [63].



Figure 2.15: A photo of gold nanoparticles solution obtained by the ablation of a bulk target in aqueous PEG solution.

The values of the nanoparticles size, determined by the DLS measurements, were 45 ± 5 nm for the Au-PEG complexes and 46 ± 2 nm for Au-dextran nanoparticles. As one can see, the mean size of the polymer-capped nanoparticles are at least twice as big the one obtained from the TEM measurements. In contrast to TEM, which provides the real size of gold particles, DLS measurements give their hydrodynamic size. This value usually indicates the core of the particles and the shell, formed by the absorbed molecules, including the molecules of the solvent attached to the surface. This is the reason why DLS measurements normally give larger sizes of nanoparticles than those observed by TEM. Even the nanoparticles prepared in pure water have characteristic size of 25 nm, and DLS measurements give the value of 27 nm, which is about 10% larger due to the influence of the hydration shell. However, significant difference between the hydrodynamic and microscopic size of the nanoparticles prepared in the solutions of PEG and dextran indicates the adsorption of the large number of polymer molecules on the surface of the nanoparticles and the formation of the gold-polymer complexes. As it was demonstrated previously, laser-synthesized Au nanoparticles have Au-O^- and Au-OH groups on their surface [61]. The presence of these groups facilitates the formation of the hydrogen bonds

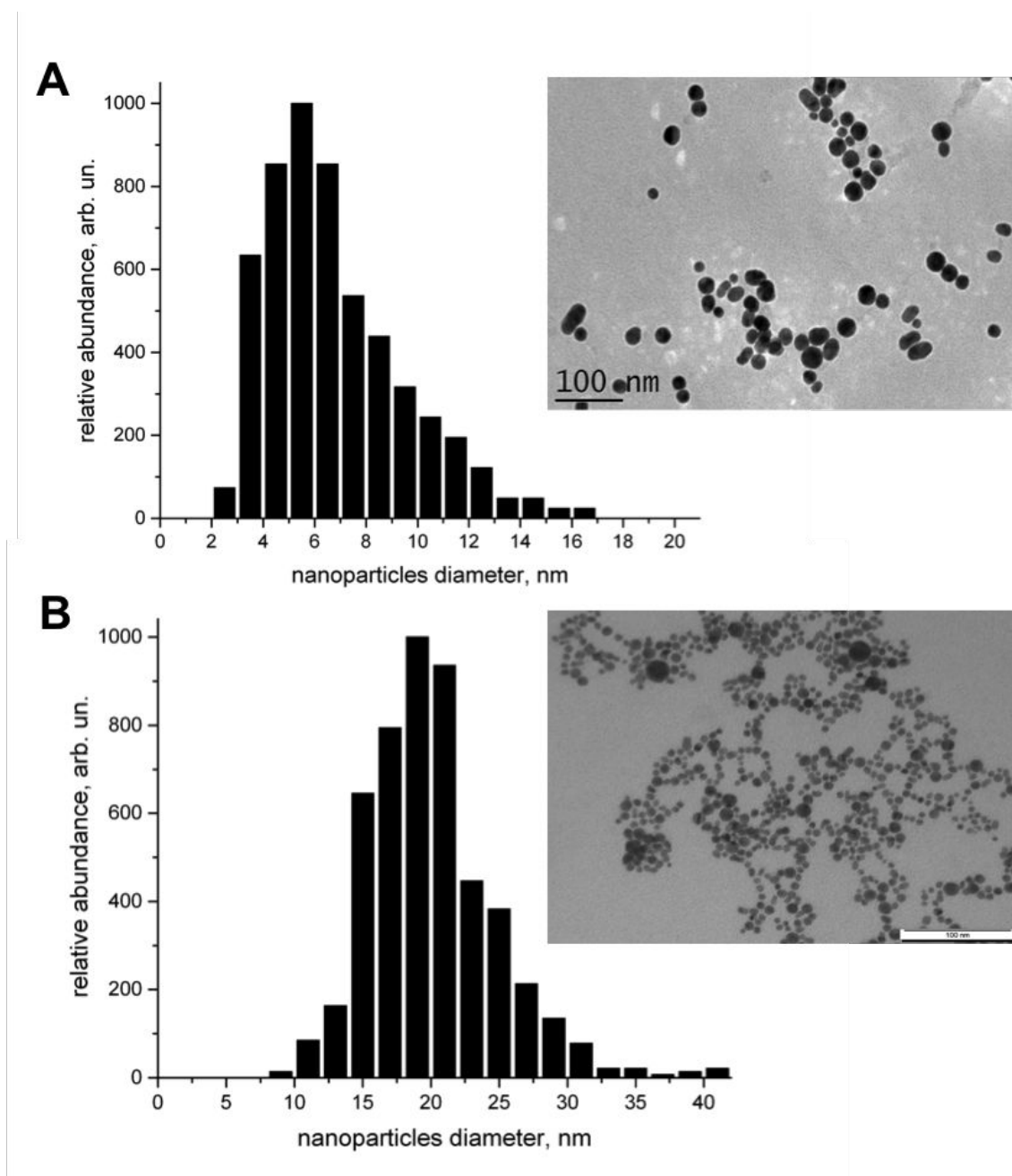


Figure 2.16: TEM microphotographs and corresponding size distributions of the gold nanoparticles obtained in aqueous (A) PEG and (B) dextran solutions.

with hydroxyl groups of PEG and dextran. Non-oxidized gold atoms can bind with OH groups of the polymers through a soft acid – hard base interaction [232].

2.4.3.2 Cyclodextrin-covered gold nanoparticles

The synthesis of the nanoparticles in the presence of cyclodextrins (CD) is another promising approach to control nanoparticles size through their capping with biocompatible molecules. Cyclodextrins are the cyclic oligosaccharides, composed of α -D-glucopyranose bonded together

through 1→4 linkages. In our work we used β -CD, which contains 7 glucose residues forming a toroid structure (Figure 2.17). Cyclodextrins are widely used in pharmaceutical industry and for drug delivery [233, 234]. In particular, β -CD covered gold nanoparticles were employed for the targeted delivery of anti-cancer drugs [235–237].

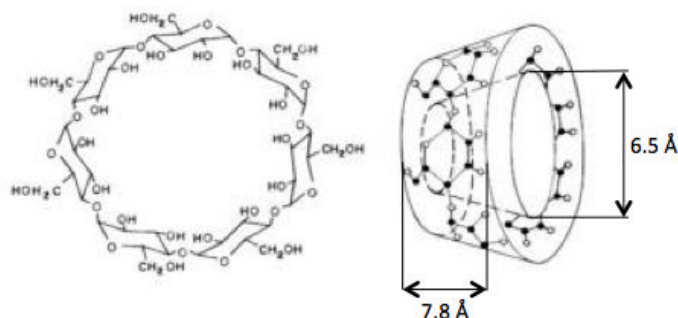


Figure 2.17: Chemical structure of β -CD and a schematic representation of its 3D toroid structure [238].

We performed the ablation of a gold target in 0.1 and 10 mM aqueous solutions of β -CD. The obtained nanoparticles were monodispersed, with relatively narrow size distribution. The mean size of the particles depended on the concentration of the CD. Here, we observed 8 ± 3 nm particles in 0.1 mM solutions, while at higher concentrations of β -CD the particles were smaller, with a mean diameter of 3.5 ± 0.5 nm. TEM images and size distributions of CD-capped Au nanoparticles are shown in Figure 2.18. Notice that the nanoparticles obtained in CD solutions were stable, regardless the concentration of the oligosaccharides implied. These results are consistent with previously reported works by Kabashin *et al.* [64, 207], where the authors managed to tune the size of Au nanoparticles between 2 and 20 nm, while keeping narrow size dispersion, by varying concentration of cyclodextrins between 0.1 and 10 mM. The size reduction in the presence of CD indicates a strong interaction between Au nanoparticles and the CD. The capping of a nucleus during its growth strongly inhibits the seed growth, while higher concentrations of CDs lead to more efficient growth inhibition.

β -CD concentration	0.1 mM	10 mM
Ablation in β -CD solution	8 ± 3 nm	3.5 ± 0.5 nm
Ablation in β -CD solution + fragmentation	9 ± 2 nm	6 ± 2 nm
Ablation in water + fragmentation in β -CD solution	9 ± 4 nm	6 ± 1 nm

Table 2.2: Table of mean nanoparticles diameters after the ablation and/or fragmentation in the presence of β -cyclodextrin.

The colloids obtained by laser ablation in β -CD solutions were then subjected to the laser irradiation for 30 minutes at 85 μ J of the pulse energy. TEM images and corresponding size

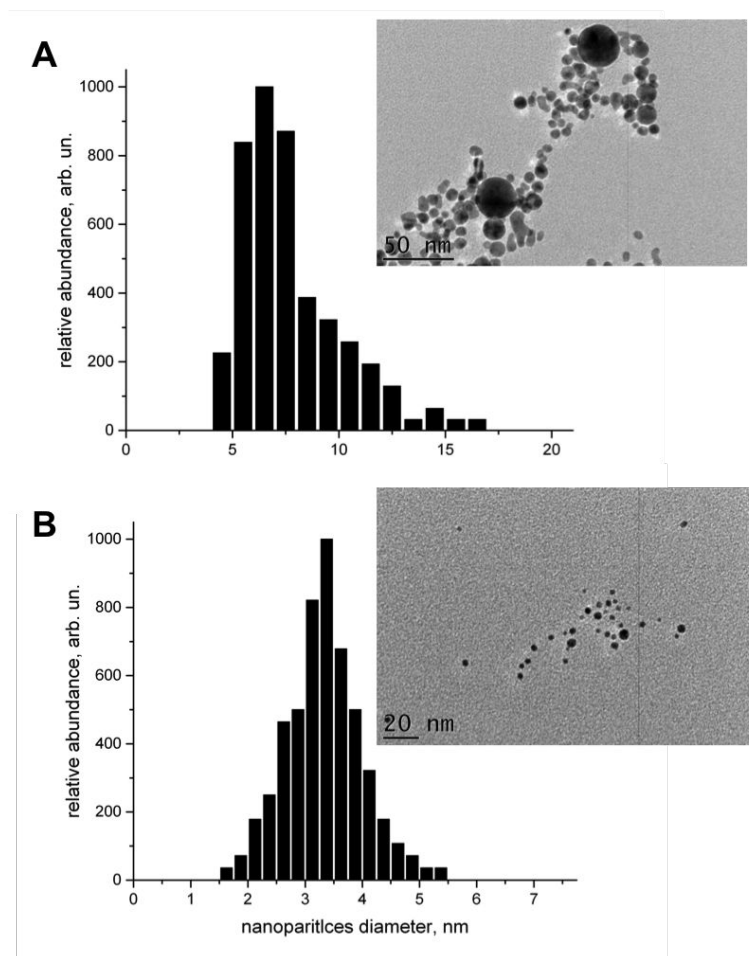


Figure 2.18: TEM images and corresponding size distributions of gold nanoparticles obtained after the ablation of a bulk target in (A) 0.1 mM, (B) 10 mM β -cyclodextrin solution.

distributions of nanoparticles after the fragmentation are shown in Figure 2.19. The mean diameter was 9 ± 2 nm in 0.1 mM solution of β -CD and 6 ± 2 nm in 10 mM β -CD solution, as Figure 2.19 demonstrates. A comparison of nanoparticles parameters before and after the fragmentation is presented in Table 2.2. One can see that for low concentrations of β -CD, the mean nanoparticles size remained almost unchanged, while for more concentrated solutions the mean size of the nanoparticles increased twofold, but still remained slightly lower than in the case of 0.1 mM β -CD solution. To explain the reason of the size increase during the fragmentation in the presence of CD, one has to consider the mechanism of the fragmentation. Mafuné *et al.* [161] supposed that during the laser irradiation of SDS-covered Au nanoparticles, a part of the SDS molecules is detached from the surface in the course of the fragmentation. We believe that the same process could take place in the case of the β -CD covered nanoparticles. On the other hand, the Coulomb explosion is the principal mechanism of the Au nanoparticles fragmentation under the femtosecond laser irradiation, which results in the fission of nanoparticles into smaller fragments. Thus, a certain amount of free CD molecules and gold nanoclusters are formed in the

solution as a result of a laser pulse interaction with β -CD-capped Au nanoparticles. In contrast to laser ablation from the target, the fragmentation deals with ablation and nanoparticles growth in volume. Such process can be accompanied by a quite different ratio between the amount of gold nuclei and β -CD molecules, which affects the equilibrium between the growth of the nuclei and the nanoparticles capping with CD molecules, resulting in different size of formed nanoparticles. At low concentrations of β -CD the same processes take place, but the difference in local Au nuclei/ β -CD ratio for the fragmentation and ablation cases is less dramatic, and therefore the mean size of nanoparticles is less affected.

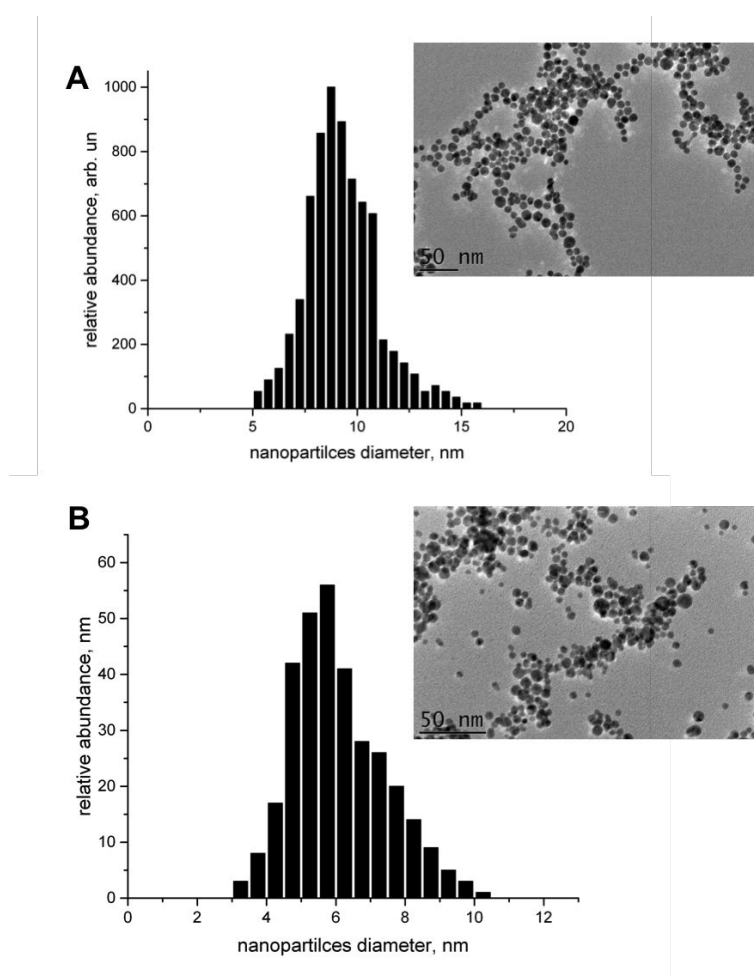


Figure 2.19: TEM images and corresponding size distributions of gold nanoparticles obtained after the ablation and fragmentation in (A) 0.1 mM, (B) 10 mM β -cyclodextrin solution.

We finally studied the effect of the β -CD presence on the nanoparticles prepared in pure water. First, we ablated a gold target in pure water, then we added β -CD at concentration of 0.1 or 10 mM to this primary solution and irradiated them with a femtosecond laser for 30 minutes at the energy of 85 μ J/pulse. Typical TEM images of the obtained nanoparticles are shown in Figure 2.20. As it is summarized in Table 2.2, the formed nanoparticles are almost identical to those produced by the fragmentation of β -CD-capped nanoparticles.

Preliminary prepared gold nanoparticles may form complexes with β -CD after the addition of the oligosaccharides. It should be noted that chemically-synthesized gold nanoparticles typically do not react with unmodified CDs directly [236,237], but this is not the case of laser-synthesized counterparts, as these nanoparticles have quite different surface chemistry [61]. When CDs molecules present in the solution, bound to the nanoparticles or not, one can obtain the same parameters of final Au- β -CD complexes. The latter experimental fact confirms our supposition that the rearrangement of the complexes occurs during the laser fragmentation due to a different ratio between “parent” Au particles and β -CD.

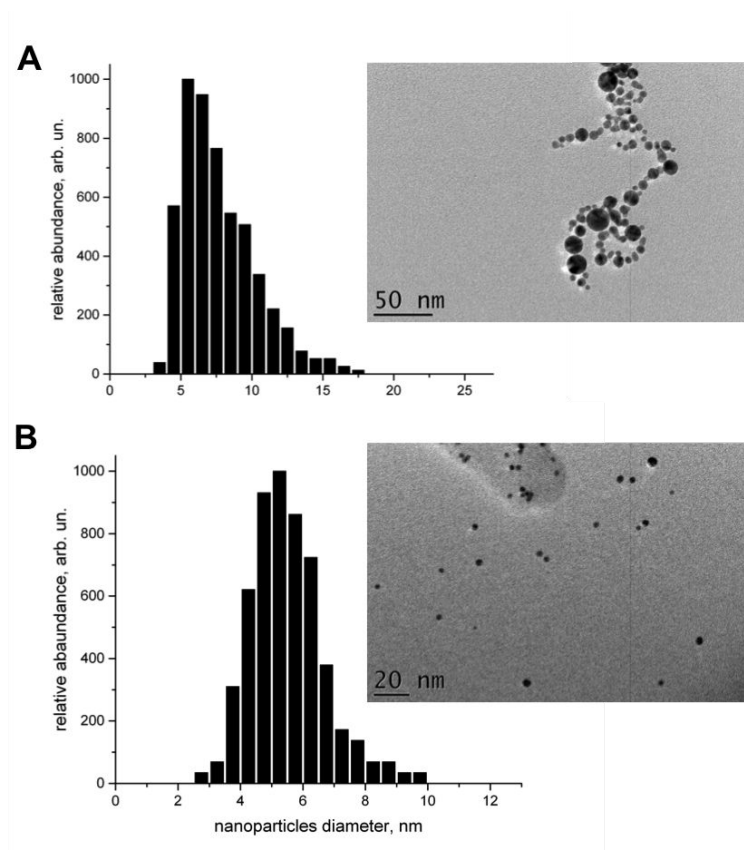


Figure 2.20: TEM images and corresponding size distributions of the gold nanoparticles obtained after the ablation of a bulk target in water followed by the fragmentation in the presence of the β -cyclodextrin; the concentration of the β -cyclodextrin was (A) 0.1 mM, (B) 10 mM.

2.4.4 Alloy nanoparticles

We found that the laser ablation technique can be used for the formation of alloys by a co-fragmentation of the mixture of two types of metallic nanoparticles. Here, the first step was to obtain initial colloids by the laser ablation from the solid target. The fabrication of the gold colloids was performed under the same conditions as described in the Section 2.4.1. To prepare the palladium (Pd) colloids, a bulk metal target was immersed in deionized water and irradiated

with 1025 nm, Yb:KGW femtosecond laser, at 15 J/cm^2 of the laser fluence, similarly to how it was done in the case of gold. The resulting solution of Pd nanoparticles was grey and opaque.

For the co-fragmentation, Au and Pd colloids were mixed at 1:1 molar ratio of Au and Pd atoms and irradiated with 1025-nm femtosecond laser pulses, at the $55 \mu\text{J}$ of the pulse energy. After 45 minutes of laser the fragmentation, the color of the mixture of two types of nanoparticles changed from reddish-grey to light brown, as it is visible in the photo of Figure 2.21.

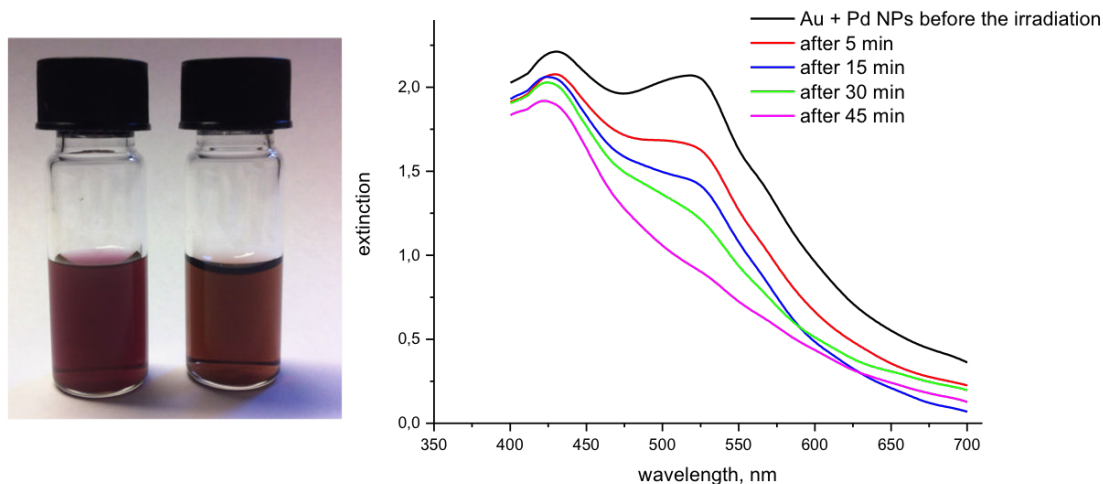


Figure 2.21: Photography of the mixture of Au and Pd nanoparticles before (left) and after 45 min (right) of the irradiation and UV-Vis absorption spectra of the mixture of Au and Pd nanoparticles before and after the irradiation.

Figure 2.21 shows a temporal evolution of UV-Vis absorption spectra of the mixture of Au and Pd nanoparticles under its laser irradiation. One can see that the maximum of absorption at 520 nm, associated with a plasmonic absorption of gold nanoparticles, completely disappears after 45 minutes of the fragmentation. The changes of the color and absorption spectra of the mixture of the nanoparticles are consistent with the alloying of metallic nanoparticles. TEM measurements demonstrated that the mean size of AuPd nanoparticles was $5 \pm 3 \text{ nm}$, while the particles had a spherical shape and were well dispersed, as one can see in Figure 2.22. The mean size of alloy nanoparticles was smaller than the size of the initial particles, which is consistent with the physics of fragmentation phenomenon.

If we take a closer look on the produced AuPd nano-alloys, we can state that the produced nanoparticles are polycrystalline. One can clearly see the fringes on the HRTEM images. Interplanar spacing for adjacent crystal planes was 2.3 \AA . This value corresponds to the (111) plane of face-centered cubic Au and Pd [239]. This value is also the same for the (111) crystal plane of AuPd alloy [239]. Polycrystalline structure of alloy nanoparticles is typical for the ultrashort pulse ablation/fragmentation. This structure arises from the coalescence of small fragments

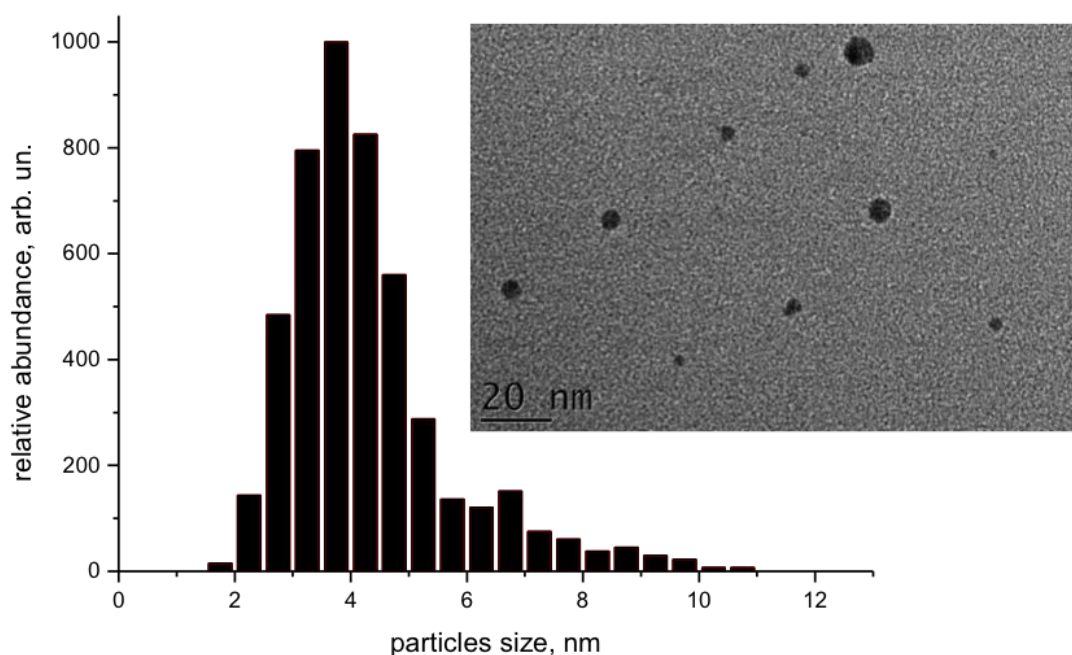


Figure 2.22: TEM image and a corresponding size distribution of AuPd alloy nanoparticles.

formed during the fission of the nanoparticles. Smaller clusters and isolated atoms participate in the smoothing of the nanoparticle surface. During the interaction with a laser pulse both Au and Pd nanoparticles get dispersed at the same rate through the Coulomb explosion mechanism. The produced small fragments, clusters and atoms of both types of metals are mixed together, and they re-aggregate and form bimetallic nanoparticles. Co-fragmentation in the solution provides homogeneous conditions for the formation of uniform bimetallic nanoparticles.

2.4.5 Optical properties

We examined optical properties of three types of nanoparticles: the nanoparticles produced by laser ablation from a bulk target, 25-nm monodispersed particles obtained by the femtosecond fragmentation, and the nano-aggregates obtained by the fragmentation at high fluences. Figure 2.24 shows the absorption, fluorescence and excitation spectra of monodispersed 25-nm gold nanoparticles. Narrow absorption peak is typical for narrow size distribution of gold nanoparticles. Smallest nanoparticles give the absorption shoulder at smaller wavelength. The absorption peak at 241 nm (5.1 eV) is related to the electron work function of gold, *i.e.* this absorption band is due to the interband transition. The extinction in the 400–800 nm region can be well modeled according to the Mie-Gans theory [240], and they are in good consistence with size distribution of gold nanoparticles obtained from TEM measurements.

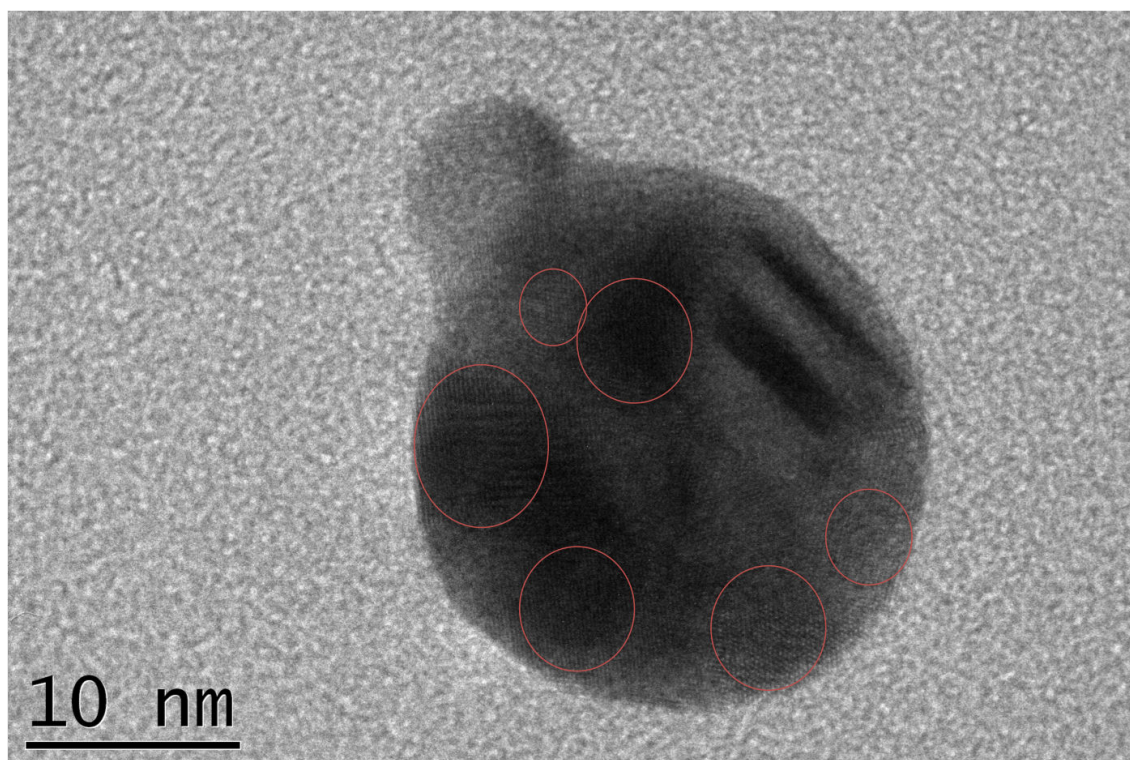


Figure 2.23: HRTEM image of AuPd alloy nanoparticle.

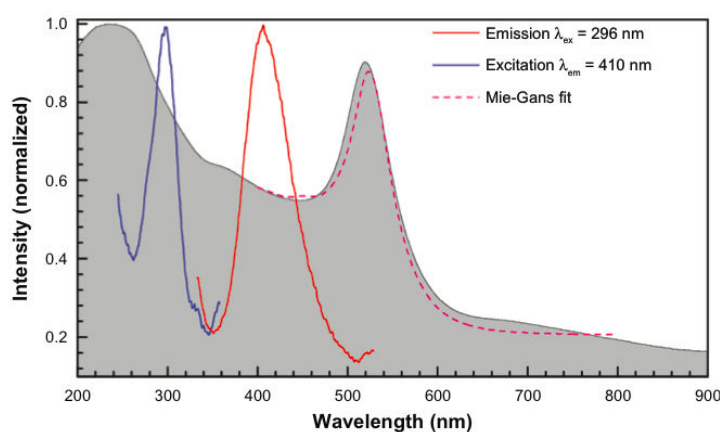


Figure 2.24: Emission and excitation spectra of gold nanoparticles obtained after laser fragmentation, spectra recorded at excitation wavelength $\lambda_{\text{ex}} = 296$ nm and emission wavelength $\lambda_{\text{em}} = 410$ nm respectively; absorption spectrum is shown as gray background; theoretical Mie-Gans fit is shown in red dotted line.

Fluorescence and excitation spectra of gold are governed by the electron transition from Fermi level to d-bands. In particular a mechanism involving $5 d^{10} \rightarrow 6 (sp)^1$ interband transition was suggested [241]. Strong emission at 410 nm was observed when the nanoparticles were excited with 290–300 nm wavelengths with an excitation maximum at 296 nm. The fluorescence properties and a plateau region in the extinction spectrum can be explained by the presence of sub-nanometer size gold particulates. Indeed, when the size of the nanoparticles is smaller than 1–2 nm, the absorption becomes strong and spectrally featureless [242, 243].

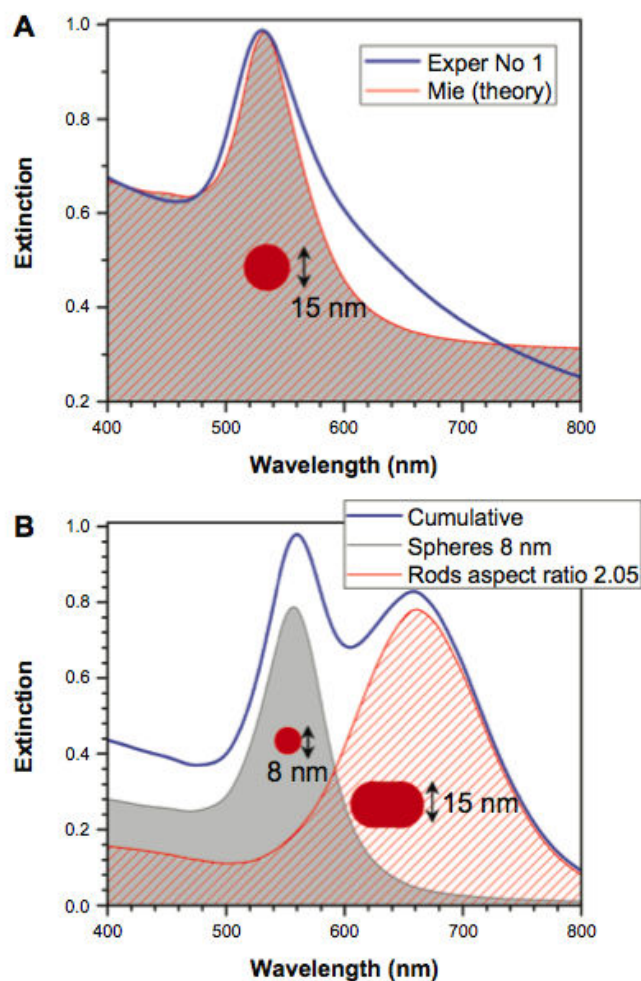


Figure 2.25: Simulated extinction spectra of gold nanoparticles after (A) ablation from a solid target and (B) fragmentation at high laser pulse energies ($120 \mu\text{J}/\text{pulse}$).

Figure 2.25 shows simulated extinction spectra for normally distributed spherical gold nanoparticles using full Mie theory and hemispherically capped cylindrical rods using electrostatically approximated Mie-Gans theory; the mean and standard deviation of radius and aspect ratio are shown in the figure. Sample of the nanoparticles produced by the laser ablation from a solid target is dominated by spherical particles, which have a large size distribution $15 \pm 14 \text{ nm}$ (Figure 2.25(A)). The simulation fit in Figure 2.25(A) was achieved by Mie theory [240]. The double feature in the extinction of nanoparticles obtained after the fragmentation at high fluences is consistent with elliptical particles (rod-shaped were used in modeling) of small aspect ratio ~ 2 recognizable in related TEM images (Figure 2.25(B)). A quantitative match is achievable when the size distribution is extracted from TEM observations. Nanoparticles produced by laser ablation at high fluences have spherical and rod-like shapes of aspect ratio close to 2 (Figure 2.25(B)). The shoulders at the longer wavelengths are due to the presence of elliptical and spherical nanoparticles, while at the shorter wavelength, a contribution of smaller

few-nanometer-diameter nanoparticles is present. The smallest nanoparticles are absorptive and luminescent.

2.5 Conclusion

- We introduced a novel method for size-controllable synthesis of stable aqueous solutions of ultrapure low-size-dispersed Au nanoparticles by femtosecond laser fragmentation from preliminary formed colloids. Such approach makes possible the tuning of mean nanoparticle size between a few nm and several tens of nm under the size dispersion lower than 70% by varying the fluence of pumping radiation during the fragmentation procedure. The efficient size control was explained by 3D geometry of laser fragmentation by femtosecond laser-induced white light supercontinuum and cavitation phenomena. The fabricated nanoparticles have a series of unique properties, which are not reproducible with conventional chemical synthesis pathways. These properties include: (i) pure, uncontaminated surface as a result of nanoparticles synthesis in pure environment (deionized water); (ii) “bare” surface of nanoparticles, which can have different reactivity and surface chemistry constants, compared to conventional colloidal nanomaterials; (iii) strong negative charging of nanoparticles, which appears as a result of particular physicochemical conditions of nanoparticles growth and contributes to a strong electrostatic stabilization of nanoparticles in the solution even in the absence of protective ligands.
- We extended femtosecond laser fragmentation procedure on the fabrication of metal alloy nanoparticles. In particular, we report the fabrication of Au-Pd alloy nanoparticles with the mean size of 5 nm. In this case, two preliminary prepared metal nanoparticles (Au and Pd) are mixed together and irradiated by a femtosecond laser.
- We developed a methodology for laser-ablative synthesis of polymer- and cyclodextrin-capped Au nanoparticles. The polymers and oligosaccharides interact with nanoparticles through hydrogen bonding and a soft acid – hard base interaction, which leads to an efficient size control and stabilization of nanoparticles solutions. The functionalization of nanoparticles with biocompatible molecules enables prospective biomedical applications.
- We characterized the synthesized nanoparticles by a variety of structural (TEM, DLS) and optical methods (optical absorption, fluorescence).

Chapter 3

Laser synthesis of Si nanoparticles

Contents

3.1	Introduction	72
3.2	Context	72
3.3	Materials and methods	74
3.3.1	Synthesis of Si nanoparticles	74
3.3.2	Measurements	75
3.4	Synthesis of Si-based nanoparticles by the fragmentation of Si colloids	75
3.4.1	Fragmentation of Si colloids. Influence of the initial particles concentration	75
3.4.2	Influence of the pH	78
3.4.3	Effect of the dissolved oxygen	81
3.4.4	Optical properties	84
3.5	Conclusion	84

3.1 Introduction

In this Chapter, we will present our results on the development of femtosecond laser fragmentation-based technique for the synthesis of Si nanoparticles. We combined the advantages of ultrashort laser ablation, which is characterized by a high crystallinity and enhanced stability of nanomaterials produced, and a 3D “volume” geometry of the ablation of preliminary prepared Si microcolloids. This technique allows us to overcome the restrictions of “planar” geometry of the ablation from a solid target, which provides a large gradients in the concentration of ablated material, leading to the uncontrolled seed growth.

First, we will review the previous works on the fabrication of Si colloids with laser ablation in liquids. In general, the same rules that we discussed in previous chapter, govern the influence of the experimental parameters on the properties of produced nanoparticles. That is why we will not repeat the basic physics of this phenomenon in present Chapter and we will overview only the recent advances and the challenges in the fabrication of Si nanoparticles by the pulsed laser ablation in liquids.

3.2 Context

Pulsed-laser deposition (PLD) in vacuum [244] or gaseous environment [245–247] are common laser-based techniques of the production of pure Si nanoparticles. However, to further prepare a colloidal solution of Si nanocrystals, one has to mill the deposited layers and disperse them in aqueous solutions. Alternatively, Si nanoparticles can be produced by laser ablation in supercritical CO₂ [248].

Laser ablation in liquids remains a promising technique to the fabrication of stable colloidal solutions of Si nanoparticles with smooth spherical shape. As in the case of metallic nanoparticles, the laser ablation with “long” pulses of a solid Si target in liquid medium results in large (up to 100 nm) and size dispersed nanoparticles [69, 70, 72, 74, 249]. Moreover, the particles are partially amorphous and tend to aggregate forming mixed nanonetworks [69, 70, 249]. The laser fabrication in organic solvents can result in smaller nanoparticles with a narrower size distribution, as it was demonstrated in ablation experiments with ethanol [77, 250]. However, high laser intensities delivered to a limited volume of liquid can induce the pyrolysis of an organic solvent, leading to the formation of SiC inclusions or graphitic multilayer structures [77, 251–253].

In addition, the energy of the laser pulse has a significant effect on the particles size distribution. In particular, under some conditions of “long” ablation, higher laser energies can lead to a decrease of mean nanoparticles size [69, 250], but this phenomenon is often accompanied by a

strong nanoparticles aggregation [69].

Ultrashort laser irradiation is known to result in the formation of the nanoparticles with improved characteristics. Indeed the ablation with femtosecond pulses leads to the formation of nanoparticles with a larger portion of crystalline phase and higher stability towards the aggregation [75–79, 254]. The influence of the pulse duration on the size of the nanoparticles was studied by Kuzmin *et al.* [77]. The mean size of the nanoparticles decreased from ~ 60 to ~ 20 nm as the pulse length decreased from 900 to 35 fs. A significant size decrease was observed for <100 fs pulses, whereas the size remained quasi-constant when the pulses with durations in the range of 200–900 fs were applied [77]. The mechanism of the formation of nanoparticles in the case of the femtosecond ablation is different from the long-pulse ablation. As it is described in the Section 1.2.3, isochoric heating of the lattice results in ultrafast non-thermal heating and the formation of a superheated liquid [255, 256]. This results in a direct ejection of the material in the form nanoclusters [112, 122], while in the case of the nanosecond ablation, the nanoparticles are formed through the vaporization, followed by the condensation during the adiabatic cooling of the expanding plasma plume. Melting and vaporization under the nanosecond ablation regime lead to the formation of micron size particles (“liquid” droplets), which contribute to the broadening of the size distribution. Combined molecular dynamics and direct simulation Monte Carlo calculations demonstrated that two mechanisms of the formation of the nanoparticles under the femtosecond ablation regime can take place: small particles are directly ejected from the target, while larger particles are formed by condensation and evaporation inside the ablated plasma plume [113, 133].

A proper mechanism of the nanoparticles formation under femtosecond ablation regime induces a particular dependence of nanoparticles size on laser fluence. The ablation at low laser intensities typically yields small (2–3 nm) Si nanoparticles with narrow size dispersion, whereas the increase of the laser fluence results in the size increase up to few tens of nm and broadened size distribution [75, 79]. Hence, the size control based on the variation of laser intensity, which was efficient in the case of gold [56, 57], seems to be hardly useful for silicon.

In order to control the size distribution of the nanoparticles, several techniques were proposed. Similar to the case of gold nanoparticles, the nanosecond ablation in the presence of SDS results in 20-nm nanoparticles with relatively narrow size dispersion [71]. *In situ* conjugation with oligonucleotides during the laser ablation allows one to obtain small (3.5 nm) and uniform nanoparticles [78]. However, the treatment of the nanoparticles with stabilizing molecules leads to the loss of the advantages of bare nanoparticles surface and limits the possibilities of their further modification.

Post-ablation manipulations can also reduce the nanoparticles size and size dispersion. Ultrasonic treatment combined with HF etching [74] or filtration [254] results in ultrasmall (1–5.5 nm) monodispersed Si nanocrystals. In addition, it was noticed that increase of irradiation time during the fragmentation procedure led to the narrowing of the size distribution, suggesting strong interaction of the laser beam with the produced nanoparticles [76]. In particular, it was demonstrated the nanosecond laser irradiation of particles prepared by mechanical milling resulted in the formation of regular spherical nanoparticles [73], such homogenization of nanoparticles size confirms the interaction of the laser pulse with colloidal particles. The combination of the advantages of the femtosecond laser ablation and 3D geometry of laser fragmentation offers an efficient way to the facile size-controllable synthesis of pure Si nanoparticles.

3.3 Materials and methods

3.3.1 Synthesis of Si nanoparticles

The first step to the laser-assisted synthesis of Si nanoparticles was the production of the suspension of “parent” particles. First, p-type B-doped silicon wafer with specific resistivity of about 1–10 $\Omega \cdot \text{cm}$ purchased from Siltronix (France) was crashed with a hammer in order to get a powder with particle size ~ 1 mm. The particles were dispersed in deionized water to the concentration 10 g/L. Then the particles suspension was milled in a Fritsch Pulverisette 7 planetary ball mill with 5-mm WC grinding balls. The milling time and rotation speed were 5 minutes and 1000 rpm, respectively. The milled nanoparticles were of irregular form and normally size dispersed between few tens of nm and 1 μm with the mean size around 500 nm, as shown in Figure 3.1. The final Si particles solution was dark grey.

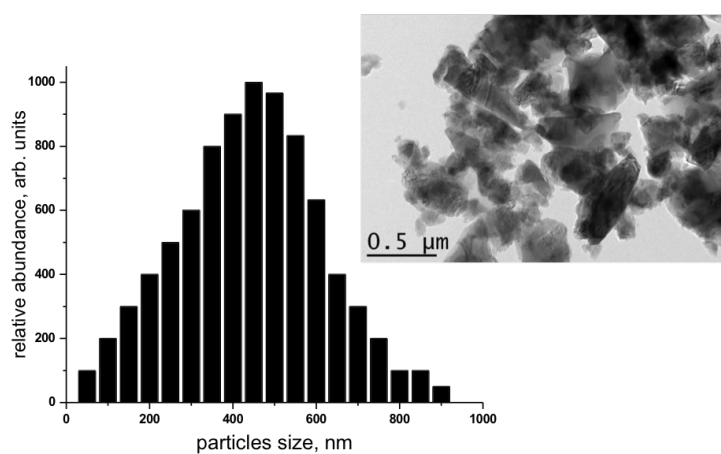


Figure 3.1: TEM image and a size distribution of Si particles after the mechanical milling.

The second step was the femtosecond laser fragmentation of “parent” colloids. The aqueous

suspension of Si particles obtained by mechanical milling were diluted with deionized water to different concentrations from 0.08 to 1 g/L. In some cases the pH of the solutions were adjusted with NaOH or HNO₃. The suspensions were transferred into a glass cuvette and subjected to the laser irradiation with Yb:KGW femtosecond laser (Amplitude Systems, 1025 nm, 480 fs, 1 kHz), the same that we used for the fabrication of Au nanoparticles. The laser beam with initial diameter of 2.3 mm was focused by a 75-mm lens onto the center of the solution, while it was stirred continuously with a magnetic stirrer to homogenize the fragmentation process. The duration of the laser irradiation step was chosen to ensure an equilibrium size distribution of the prepared colloids, which depended on the concentration and varied from 45 minutes for 0.08 g/L to 5 hours for 1 g/L solutions. The experiments were carried out both under the ambient conditions, when water was saturated with air, and in deoxygenated conditions, where a nitrogen was bubbled through the solutions prior and during the laser irradiation.

3.3.2 Measurements

TEM and HRTEM studies were performed using JEOL JEM 3010 system operating at 300 kV in imaging and diffraction modes. The samples for the TEM measurements were prepared as it was described in the Section 2.3.4. X-ray photoelectron spectroscopy (XPS) investigations were carried out in an ultrahigh vacuum system ESCALAB210 (base pressure 1.0×10^{-10} mbar) from Thermo VG Scientific. The colloids were dropped on the Cu substrate prior the measurements. The measurements were taken over an area of 1 mm² of the covered Cu substrate. Photoelectrons were excited by using Mg K α line (1253.6 eV). The photoluminescence spectra were registered for the ~ 0.5 mL of the colloidal solutions transferred into a quartz cuvette under the excitation with continuous wave radiation of an Ar-ion laser (364 nm, 10 mW, spot diameter ~ 1 mm). Photoluminescence signals were recorded using a grating monochromator (MS750, SOLAR TII) equipped with a CCD array. The optical measurements were done at room temperature.

3.4 Synthesis of Si-based nanoparticles by the fragmentation of Si colloids

3.4.1 Fragmentation of Si colloids. Influence of the initial particles concentration

Laser treatment of suspensions of Si particles leads to a significant change in the color of the solutions: from opaque and deep-gray to completely transparent and light-brown (when the solution was preliminary deaerated) or colorless (when water was saturated with air). The solutions

after laser irradiation remained stable without any signs of the precipitation. As Figure 3.2 demonstrates, the irradiation of the suspensions containing relatively low amount of “parent” particles (0.08–0.1 g/L) resulted in small (2–3 nm) nanoparticles (Figure 3.2(A)). The full width at half maximum (FWHM) lower than 2.5 nm evidences a low size dispersion of the formed nanoparticles. However, a 6-times increase of the concentration of initial colloids resulted in nanoparticles with mean size of 20–25 nm and a size dispersion lower than 10 nm FWHM (Figure 3.2(B)). Additionally, we estimated the stability of the colloids produced by the femtosecond fragmentation. Aging for 2 month in sealed glass did not reveal any signs of the precipitation. TEM measurements did not demonstrate the changes in the nanoparticles size distribution nor the agglomeration effects.

We believe that narrow size distributions results from the 3D volume ablation geometry. Under femtosecond irradiation, the silicon particles can absorb both the main radiation harmonics (1025 nm) and white-light radiation from the supercontinuum, leading to their fragmentation and formation of nanoclusters. The nuclei then coalesce forming bigger nanoparticles. The process of the growth is diffusion-limited, and the final size of the particles depends on the concentration of the nuclei in the given volume. In the case of the ablation from the bulk target, the action of a laser pulse leads to the ejection of a considerable amount of Si atoms and clusters into limited volume near the focal spot. This causes a gradient of the nanoclusters concentration and thus different conditions of the nanoparticles growth, even though the seed growth continues for hundreds of nanoseconds after the laser pulse [53, 187]. Significant broadening of the size distribution, observed in many studies [76–79], can originate from the non-homogenous conditions for the nanoparticles formation. In contrast, in the employed “volume” geometry of laser ablation of Si nanoparticles suspended in water, the nanoclusters are quasi-uniformly produced in a relatively large liquid volume, roughly corresponding to the size of the laser caustics (a few tens of microns). This leads to the homogeneous conditions of seed growth and a relatively uniform size of formed nanoparticles. Since the coalescence and size of final nanoparticles depend on the nuclei concentration, the variations of the initial particles concentration allow the size control of the nanoparticles, because of the different amount of the nanoclusters generated per pulse. As shown in Figure 3.3 for the range of the “parent” particles concentration used, the nanoparticles mean size increased linearly as the initial concentration increased, thus allowing us to efficiently tune the size of final nanoparticles from 1–2 to 20–25 nm. The femtosecond irradiation results in the fragmentation of the Si powders, yielding much smaller nanoparticles compared to the nanosecond irradiation case, which is characterized by nanoparticles heating and reshaping, resulting in the formation of sub-micron size Si spheres [73].

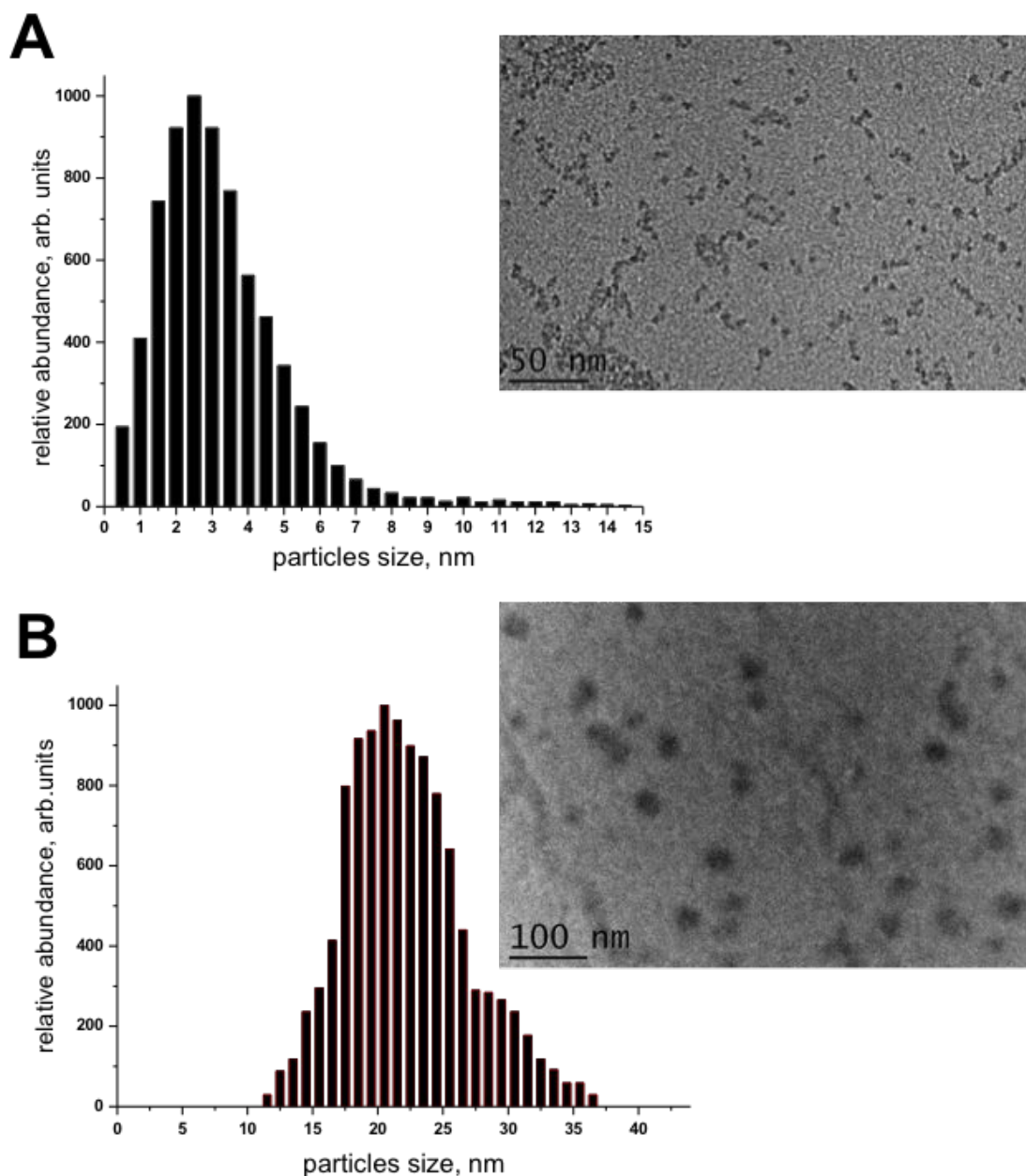


Figure 3.2: TEM images and size distribution of Si nanoparticles after the laser irradiation at (A) low (0.08 g/L) and (B) high (0.5 g/L) concentration of initial Si powder.

As shown in Figures 3.4(A) and (B), characteristic fringes can be easily seen on the high resolution TEM images of both small and large Si nanoparticles. The presence of these fringes indicates high crystallinity of the produced particles. Besides, one can see that large particles obtained by the fragmentation of Si particles at high concentrations are composed of multiple crystalline domains. Such structures are probably formed through to the fragmentation of big crystalline “parent” particles into smaller clusters, that further coalesce to form small nanoparticles. The electron diffraction images confirmed the polycrystalline cubic structure of Si nanopar-

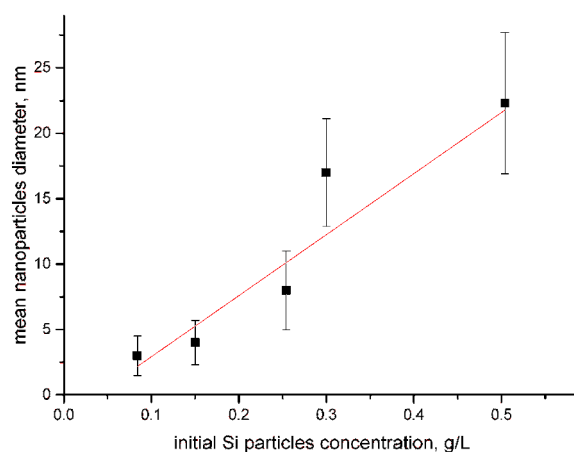


Figure 3.3: Mean nanoparticles size after the after the laser fragmentation as a function of the initial concentration of Si particles suspension. The error bar corresponds to the standard deviation of the nanoparticles diameter.

ticles produced by the laser treatment (Figure 3.4(C)). Here, the observed rings corresponded to the following crystal plane orientations: 2.12 Å for $\langle 111 \rangle$, 1.92 Å for $\langle 200 \rangle$, 1.35 Å for $\langle 220 \rangle$ and 1.16 Å for $\langle 113 \rangle$. Fast Fourier Transform (FFT) images have also confirmed the presence of $\langle 111 \rangle$ crystal planes, with an interplanar distance of 2.1 Å.

3.4.2 Influence of the pH

Laser fragmentation from colloids allows facile control of the size of the produced nanoparticles through varying the parameters of the initial solutions. pH of the solution is another parameter that can be easily varied during the synthesis. We performed the laser fragmentation of Si particles at two concentrations: high (0.5 g/L) and low (0.08 g/L); and at three pH values: acidic (pH 3.0), neutral (pure water, pH 7.4) and alkaline (pH 11.0). TEM images and size distributions of the produced nanoparticles are presented in Figure 3.5. The data of the mean nanoparticles size and size distribution are summarized in the Table 3.1. As one can see, the fragmentation of “parent” Si particles at low concentrations resulted in small nanoparticles of the size about 1.5–5 nm (Figure 3.5(A–C)). The fragmentation in acidic medium yielded slightly bigger particles (~ 5 nm) as compared to the particles obtained in pure water. In contrast, increase of the pH led to smaller nanoparticles. Moreover, the fragmentation in alkaline medium resulted in a significantly narrower size distribution (Figure 3.5(C)). In the case of high concentrations of initial colloids, the mean size of the particles after the fragmentation remained always in the range of 20–25 nm, regardless of the pH of the medium (Figure 3.5(D–F)). The results are summarized in the Table 3.1

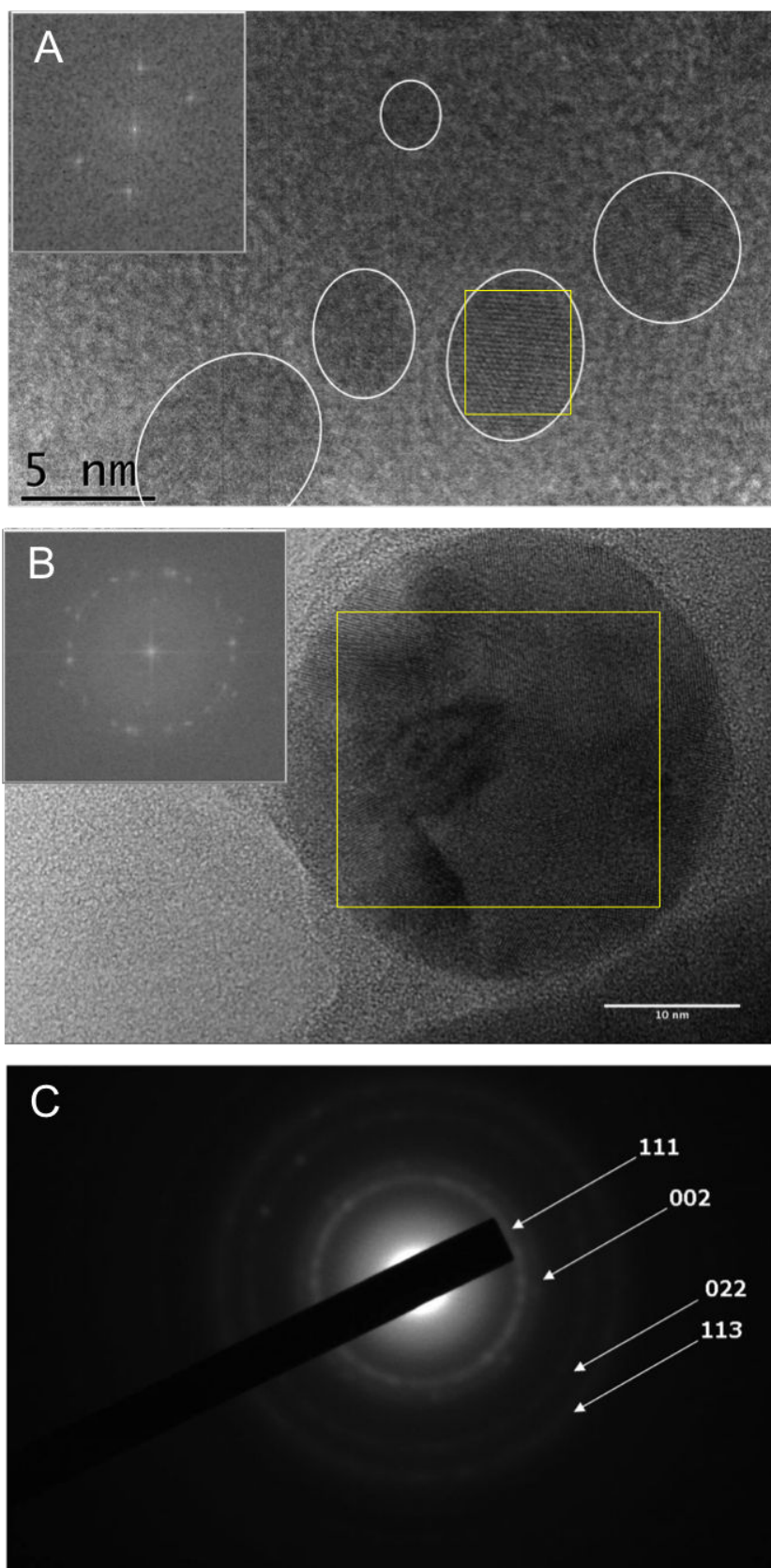


Figure 3.4: HRTEM images of (A) small Si nanoparticles obtained after the fragmentation of 0.08 g/L suspension of Si powder, (B) large Si nanoparticles after the fragmentation of 0.5 g/L suspension; the insets in (A) and (B) represent the FFT images of the selected region. (C) Electron diffraction pattern of Si nanoparticles after the fragmentation.

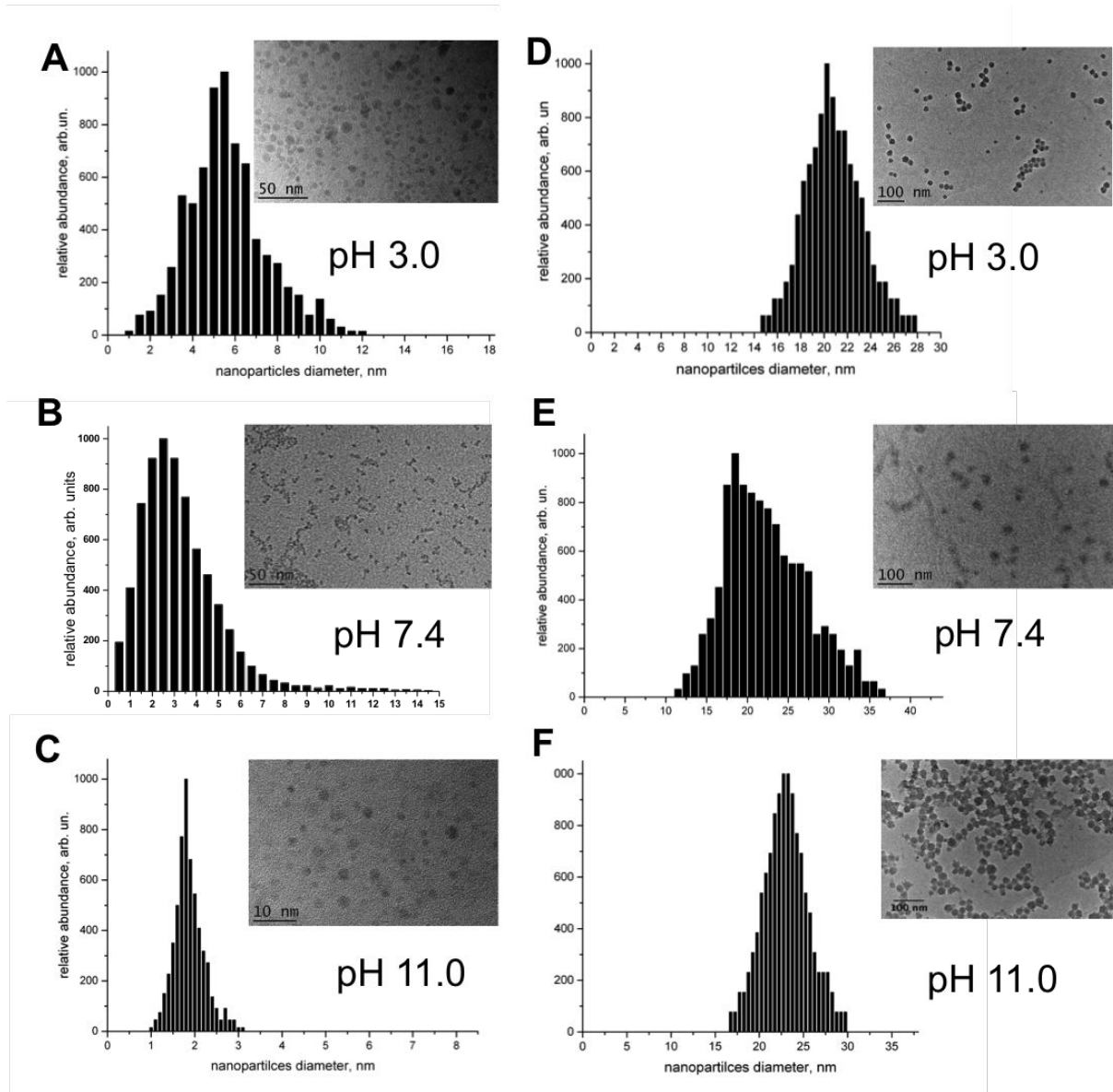


Figure 3.5: TEM images and corresponding size distributions of Si nanoparticles after the laser fragmentation at (A–C) low (0.08 g/L) and (D–F) high (0.5 g/L) concentrations of the initial colloids and (A, D) pH 3.0, (B, E) pH 7.0 and (C, F) pH 11.0.

It was previously demonstrated that the size of the oxide nanoparticles depended strongly on the pH of the solution under the supposition that the nanoparticles growth occurs through the adsorption of the atoms on a nucleus surface [257, 258]. The particles size R is proportional to:

$$R \sim \frac{3C\bar{v}}{F} \left[\frac{\sigma}{10^{(\text{pH}-14)\alpha}} \right], \quad (3.1)$$

where F is the Faraday constant, C is the concentration of the material species (ions or atoms) in the solution, \bar{v} is the molar volume of the oxide, σ is the surface charge density, and $0 < \alpha < 1$ is a coefficient depicting the ability of the interface to extend by adsorption. This dependence was obtained when the nanoparticles are formed in the solution by the precipitation

Si particles concentration	0.08 g/L	0.5 g/L
pH 3.0	5 ± 2 nm	20 ± 3 nm
pH 7.4	3 ± 1.5 nm	22 ± 5 nm
pH 11.0	1.7 ± 0.3 nm	23 ± 4 nm

Table 3.1: Table of mean Si nanoparticles diameters after the laser fragmentation under different pH values. The data are given for initial concentrations of colloids of 0.08 g/L and 0.5 g/L.

from the metal salts [257]. However, under certain assumptions we can apply it for our case of the growth of Si/SiO_x nanoparticles from the fragments obtained by the laser fragmentation of large particles. According to the equation (3.1), alkaline media with higher pH favor the formation of smaller particles. The value of the pH influences significantly on the particles parameters, when it is higher than the point of zero charge (PZC) of the material [257]. PZC for SiO₂ is typically estimated at the level of 2.9–3.5 depending on the phase [259]. Therefore, increasing the pH of the medium above ~ 3 , we can expect the decrease of the size of the Si-based nanoparticles. This is consistent with our results (Table 3.1), when we observed the decrease of the nanoparticles size from 5 to 1.7 nm while the pH was increased from 3.0 to 11.0. Additionally, relation (3.1) predicts a linear dependance of nanoparticle size on concentration of the particle precursors that we observed in our tests (Figure 3.3).

Effect of the pH on the particles formation is significant for the oxide nanoparticles or when the portion of the oxide in the composition of a particle is relatively large. However, as it will be discussed in details in next paragraph, Si nanoparticles produced by the laser fragmentation are composed of a crystalline Si core and a surface oxide layer. For large nanoparticles (produced from more concentrated initial colloids) the ratio between Si⁰ and SiO_x can be larger, compared to the 2–5 nm nanoparticles, just due to a smaller surface area/volume ratio. Therefore, the effect of the pH variations on the concentrated initial solutions should be less significant. Nevertheless, the variations of the pH, at which the fragmentation of Si particles is performed, is a useful tool for fine tuning of the size of small Si-based nanoparticles.

3.4.3 Effect of the dissolved oxygen

We observed a change of color of the solutions during the fragmentation process. Here the final solution color depended if the nitrogen was bubbled through the solution before and during the experiment or not. The solutions were colorless in the case of the fragmentation in aerated water, but they became brown-gray (but more transparent) when the solutions were deoxygenated. XPS revealed a strong influence of the amount of the oxygen dissolved in water on the composition of laser-synthesized nanoparticles. The deconvolution by Gaussian contours of Si 2p XPS spectra

of the solutions before and after the fragmentation in deoxygenated conditions (Figure 3.6(A), black and blue circles respectively) demonstrated the presence of three bands, including a low intensity band at ~ 99.0 eV, an intense band at ~ 101.0 eV, and another intense band at ~ 103.0 eV. These bands correspond to crystalline unoxidized silicon Si^0 , silicon monoxide Si^{2+} (SiO) and completely oxidized silicon Si^{4+} (SiO_2). The peaks assignment is in complete accordance with the data from the literature ($\text{Si}^0 = 98.9$ eV, $\text{Si}^{1+} = 100.0$ eV, $\text{Si}^{2+} = 101.1$ eV, $\text{Si}^{3+} = 102.0$ eV, $\text{Si}^{4+} = 103.2$ eV) [260]. XPS spectrum after the laser fragmentation in air-saturated water (red circles in Figure 3.6(A)) contained only two bands at 101.0 eV (low intensity) and 104.3 eV (high intensity). First low-intensity band can be assigned to Si at Si^{2+} oxidation state. We believe that the second band at 104.3 eV can belong to the completely oxidized silicon in the form of SiO_2 . We suppose that more than 1 eV shift of Si 2p electrons binding energy compared to the literature data ($\text{Si}^{4+} = 103.2$ eV) can be explained by the charging effects, in particular by positive charging of SiO_2 layer as the electrons escape from it. Such charging can lead to the increase of binding energy of Si^{4+} electrons [261–263]. In our case the binding energy difference between Si^{4+} and Si^0 increases from 4.3 eV for the particles produced in deoxygenated water to 5.3 eV for the nanoparticles obtained in ambient conditions. This fact serves the evidence of the formation of much thicker SiO_2 layer around the Si core when the particles are produced in air-saturated water.

To study the nature of the oxide structures, we additionally measured the O 1s XPS spectra (Figure 3.6(B)). The broad and diffused O 1s spectrum of initial Si particles (black line in Figure 3.6(B)) can be assigned to the presence of sub-stoichiometric natural silicon oxides (SiO_x) and possibly to oxygen absorbed on the sample holder (the band near 527 eV). Whereas the O 1s spectra of Si nanoparticles after the fragmentation (red and blue curves in Figure 3.6(B)) reflect an increase in the oxidation degree of the nanoparticle surface with the amount of oxygen dissolved in water. The O 1s spectrum of the nanoparticles produced in deaerated water (blue curve) demonstrates the presence of the peak at 531 eV, which can be assigned to OH^- groups [264, 265]. However, when the nanoparticles are produced in air-saturated water (red curve), the O 1s spectrum is dominated by a peak at 533.6 eV, which corresponds to SiO_2 configuration. Thus, our tests show that the thickness of the SiO_2 layer for the Si nanoparticles can be controlled by varying the concentration of dissolved molecular oxygen in water. We believe that the disappearance of the grey color of the solution during the fragmentation in ambient conditions is related to the oxidation effect.

It should be noted that XPS data are collected only from the superficial layer of the particles, while internal layers are beyond the reach of the method. In our case the inelastic mean-free

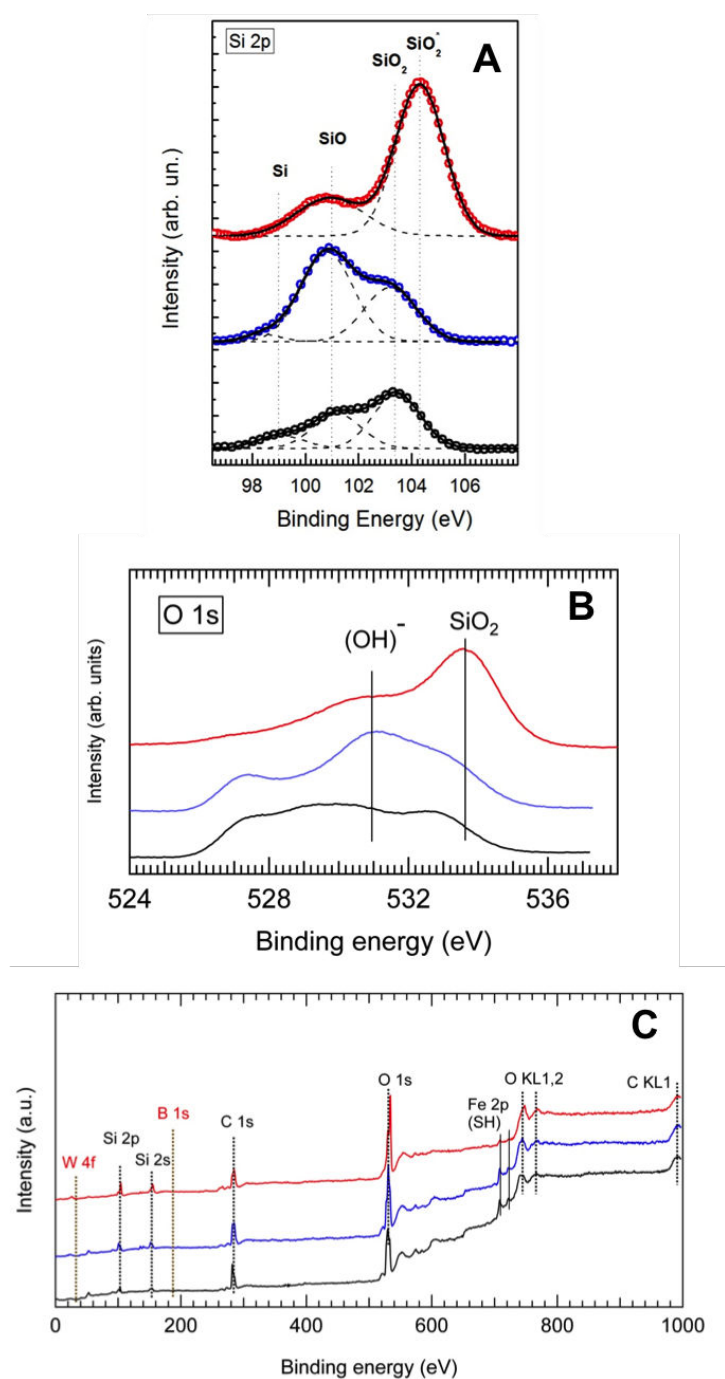


Figure 3.6: (A) Si 2p, (B) O 1s and (C) survey XPS spectra of Si particles before (black) and after the laser fragmentation in deaerated (blue) and air-saturated (red) deionized water. Experimentally measured spectra are fitted by Gaussian curves (dotted lines) whose sum spectra are shown in with black solid lines. The peaks identified on the survey spectra are labeled. The positions of W 4f and B 1s lines, which were not observed in our case, are indicates with red vertical dotted lines. Two Fe 2p lines belong to the sample holder (SH).

path of Si 2p photoelectrons in Si and SiO₂, λ_{Si} and λ_{SiO_2} , are estimated as 0.80 and 0.92 nm respectively [266]. The probe depth in XPS measurements is usually defined as the depth from which 95% of all photoelectrons are scattered by the time they reach the surface, and it is equal to 3λ [266]. Thus, the maximum depth from which XPS can get the signal is 2.40 nm for Si

and 2.76 nm for SiO₂. Since the size of the synthesized nanoparticles was in the range 3–25 nm, therefore the probe depth for Si 2p electrons was not enough to fully characterize the composition of internal nanoparticle layer. However, our electron diffusion studies demonstrated the presence of crystalline Si core even in strongly oxidized nanoparticles.

It is important that XPS measurement did not reveal the traces of the contamination on the surface of the nanoparticles. As Figure 3.6(C) demonstrates, the survey XPS spectra of the nanoparticles do not possess any peaks associated with the presence of W (potential contamination from the mill balls used for the mechanical milling step in the fabrication of the Si nanoparticles), B (a doping element in Si wafers), or other contaminating atoms.

3.4.4 Optical properties

Silicon nanocrystals prepared by the laser ablation in liquid medium were reported to have photoluminescent (PL) properties and emit a strong luminescence signal [69, 70, 72, 267]. In our experiments we also observed remarkable PL signals with two main peaks at about 450 and 900 nm for the nanoparticles prepared by the fragmentation in air-saturated water (red curve in Figure 3.7). However, in the case of the Si particles prepared in liquid, the signal is weaker compared to the electrochemically prepared porous silicon [45], or nanostructures formed by the laser ablation in gaseous environment [268, 269]. In addition, the nanoparticles prepared in deoxygenated solution exhibited much weaker photoluminescence (blue curve in Figure 3.7). It can be explained by an insufficient passivation of the nonradiative surface states of the formed nanoparticles by formed SiO₂. This supposition is confirmed by a much weaker Si⁴⁺ peak in the Si 2p XPS spectrum compared to the case of the laser fragmentation in air-saturated water (Figure 3.6(A)). A certain level of the oxidation is required for efficient PL, as for example it was demonstrated in the case when the aging associated with nanoparticles oxidation in solution significantly enhanced the luminescence signal [71].

3.5 Conclusion

We proposed a new method of the synthesis of pure Si-based nanoparticles, which consists in the femtosecond laser ablation from preliminary water-dispersed micron size particles. This method can provide stable concentrated colloidal solutions of non-agglomerated, spherical and low size-dispersed nanoparticles exhibiting prominent luminescent characteristics. Besides, we can control the size and the surface composition of the nanoparticles by varying several parameters of the system, such as:

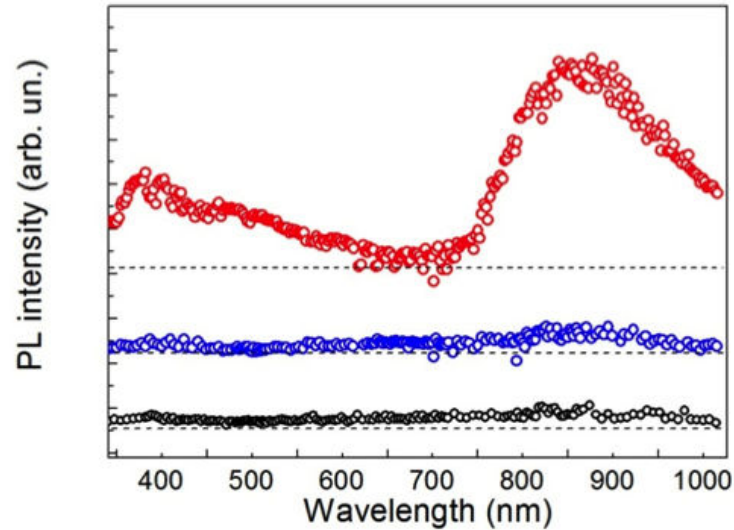


Figure 3.7: Room temperature photoluminescence spectra of Si particles before (black) and after the laser fragmentation in deoxygenated (blue) and air-saturated (red) deionized water.

- The variations of the concentration of the initial colloids allowed us to tune the size of the nanoparticles from 1–2 to 20–25 nm;
- Additionally, changing the pH of the solutions we could perform “fine” tuning of the size of the nanoparticles;
- By performing the fragmentation in ambient or deaerated conditions we managed to alter the depth and the composition of the oxide layer on the surface of the nanoparticles.

Due to exceptional purity, biocompatibility and biodegradability laser-synthesized Si nanoparticles present a unique object for biomedical applications, which cannot be reproduced by conventional chemical or electrochemical pathways.

Chapter 4

Applications of the laser-produced nanoparticles

Contents

4.1	Introduction	88
4.2	Gold nanoparticles for fluorescence quenching and surface-enhanced Raman spectroscopy	88
4.3	Light controlled surface plasmon properties of gold nanoparticles .	91
4.4	Gold nanoparticles for biomedical applications	97
4.5	Si nanoparticles for radio-frequency radiation-induced hyperthermia	100
4.6	Au and AuPd nanoparticles as electro-catalyst	104
4.7	Conclusion	108

4.1 Introduction

Laser-synthesized nanoparticles are unique objects due to their bare surface and the absence of any contamination. These properties are typically not possible with conventional chemically-synthesized nanoparticles, which makes laser-synthesized particles a promising material for multiple applications. For instance, their purity ensures their biocompatibility and opens the way for multiple biological and biomedical applications. Additionally, the bare surface enhances the processes that take place on the interface between the nanoparticle and surrounding medium. Thus, it can promote their catalytic and plasmonic properties.

In this chapter we will demonstrate the potential of the nanoparticles that were designed and synthesized according to the techniques described in Chapters 2 and 3, for the applications in drug delivery, hyperthermia therapy, electro-catalysis and also their plasmon-related properties.

4.2 Gold nanoparticles for fluorescence quenching and surface-enhanced Raman spectroscopy*

Gold nanoparticles exhibit unique optical properties due to the excitations of plasmons. For instance, efficient optical absorption/scattering allows the employment for the optical contrast in biological imaging [12,270]. Besides, strong electric field enhancement near gold nanoparticles is actively used for surface-enhanced Raman spectroscopy to detect and identify biological and chemical species [19,20,271,272]. In the case of the nanoparticles obtained by the laser ablation, pure surface and unique surface chemistry serves a distinct advantage for the applications in SERS and fluorescence microscope and imaging. First, the absence of surface contamination excludes the presence of parasitic signals in Raman spectra. Secondly, bare surface and negative charge on it facilitates the conjugation of gold nanoparticles with molecules of interest and the interaction between the adsorbed molecules and nanoparticles. In frame of our work we examined Raman scattering of gold nanoparticles obtained by femtosecond laser ablation and fluorescence lifetime of dyes in their presence.

In order to prepare SERS samples, laser-synthesized Au nanoparticles were immobilized to the surface of a silicon wafer through a mercaptosilane ((3-mercaptopropyl)trimethoxysilane, 3MPTS) cross linkers. Then the sample was soaked in aqueous solution of rhodamine 6G (Rh6G) and rinsed with water prior to collecting SERS spectra. Thus, immobilized gold nanoparticles are supposed to act as an SERS substrate [273]. The recorded spectrum of the nanoparticles

*This study was done in collaboration with Centre for Micro-Photonics and Industrial Research Institute Swinburne, Swinburne University of Technology, Australia and Laboratory of Biomedical Physics, Vilnius University Institute of Oncology, Lithuania

exposed to the Rh6G solution is shown in Figure 4.1(A). The spectra possess Rh6G signature peaks with a small shift from those in solution [274] at: 611 (614 in solution), 773 (774), 1124 (1129), 1185 (1183), 1312 (1310), 1364 (1363), 1506 (1509), and 1645 (1650) cm^{-1} . Small shifts of spectral positions of the peaks are related to changes in the state of the Rh6G molecules when they are adsorbed on the surface of the substrate. The differential spectrum (Figure 4.1(B)) clearly reveals Rh6G and demonstrates the feasibility of using the Au nanoparticles synthesized by the laser ablation for SERS sensing.

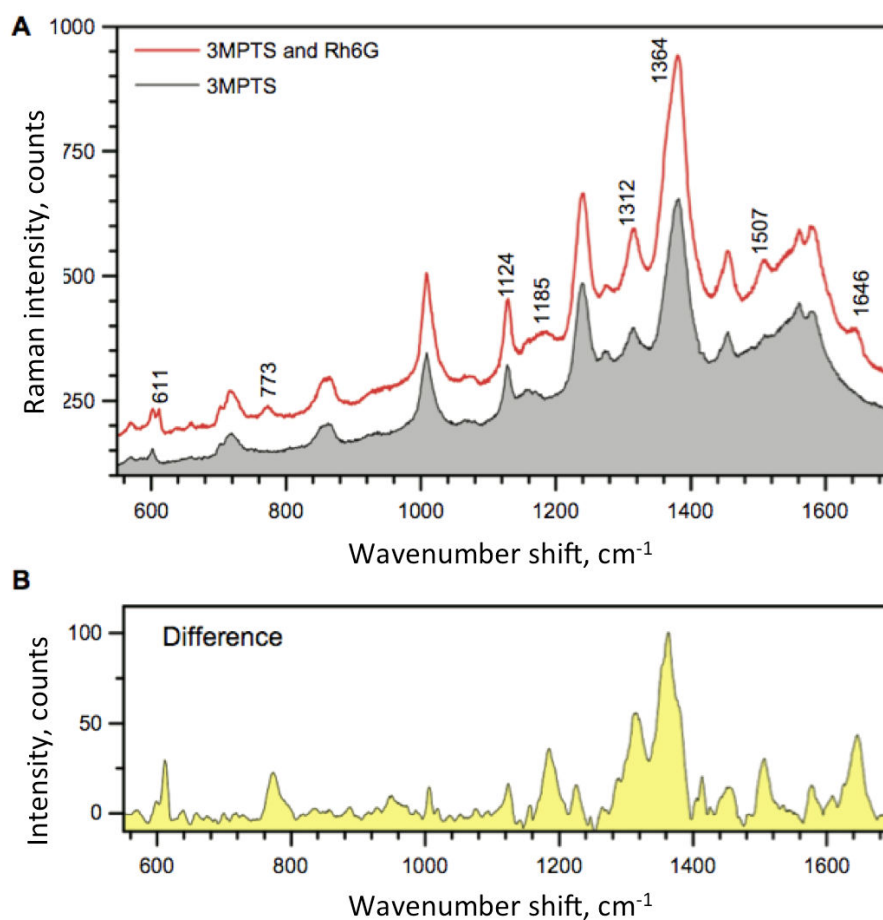


Figure 4.1: (A) Surface-enhance Raman spectra of gold nanoparticles treated with mercaptosilane (3MPTS) and with rhodamine 6G (Rh6G). (B) Raman spectrum of gold nanoparticles treated with Rh6G after subtracting the mercaptosilane background.

We studied the behavior of rhodamine 6G, common fluorescent dye in the presence of laser-synthesized gold nanoparticles. In our tests we used two types of particles: obtained after a simple ablation from a bulk target, and the nanoparticles produced by the two step ablation-fragmentation technique, the second fragmentation step was performed at high laser intensities (120 $\mu\text{J}/\text{pulse}$). Fluorescence lifetime imaging microscopy (FLIM) demonstrated that the fluorescence of Rh6G is quenched in the presence of Au nanoparticles. The calculated lifetimes for Rh6G solution mixed with two types of the nanoparticles are shown in Figure 4.2. In the case

of 20-nm Au nanoparticles obtained after the laser fragmentation (Figure 4.2(A)), the lifetime of 12 nM Rh6G is 4.2 ns and it does not depend on the concentration of gold nanoparticles. In contrast, for 2.5 nM Rh6G the similar lifetime was observed; however, when the concentration of Au nanoparticles exceeds 200 ppm, fluorescence lifetime significantly decreases. It indicates that 20-nm Au nanoparticles can quench the fluorescence of Rh6G in the solution. For the large size-dispersed nanoparticles, produced by simple femtosecond laser ablation from a solid target (Figure 4.2(B)), the fluorescence lifetime of 12.5 nM Rh6G solution remained unchanged while increasing the concentration of the nanoparticles. However, the Rh6G solution is strongly quenched (lifetime ~ 2 ns) by the nanoparticles at all concentrations tested. Fluorescence quenching is consistent with pure-metallic nature of Au nanoparticles [275].

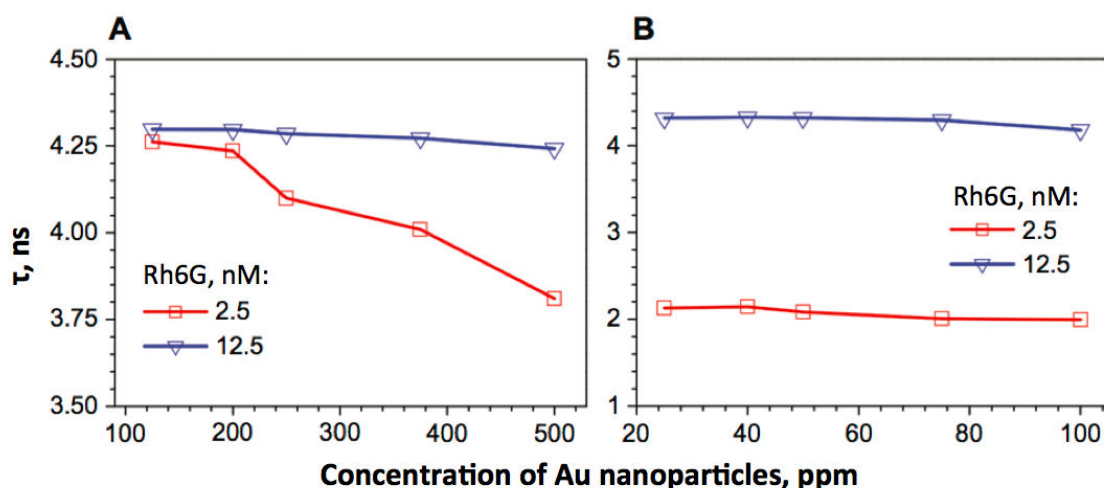


Figure 4.2: Rhodamine 6G fluorescence lifetime vs. concentration of gold nanoparticles, at two dye concentrations for gold nanoparticles prepared by (A) laser ablation followed by the fragmentation at high laser intensities ($120 \mu\text{J}/\text{pulse}$), and (B) laser ablation from a bulk target.

The quenching occurs only at low Rh6G concentrations, when dye molecules form complexes with Au nanoparticles. At higher Rh6G concentrations, the surface of the nanoparticles is saturated, and a portion of free Rh6G, which is not subjected to quenching, increases and dominates the total fluorescence signal. Hence only the fluorophore molecules that are in tight contact with the nanoparticles are quenched, suggesting the short-range mechanism, namely electron transfer [276]. This quenching process is well known for Rh6G and it plays an important role in single molecule spectroscopy [19, 277]. The different behavior of the nanoparticles after the ablation and the fragmentation can be referred to this mechanism by the different surface availabilities for Rh6G.

4.3 Light controlled surface plasmon properties of gold nanoparticles*

Bare negatively-charged surface of laser-synthesized gold nanoparticles opens the way to the multiple post-synthetic modifications in order to impart them additional properties. Besides, full-physical preparation enable the control over the size characteristics without affecting their surface composition. As an interesting example of nanoparticles modification we studied the formation of photo-sensitive complexes of laser-prepared gold nanoparticles linked to cationic surfactant containing azobenzene group. Surfactants containing azobenzene groups attract great interest for the applications in the field of light-controlled transformations of nanoobjects. These surfactants contain a charged head group, hydrophobic tail and a photosensitive azobenzene group, as it is presented in Figure 4.3. Under UV irradiation the azobenzene undergoes photo-isomerization from stable trans-conformation to cis-state. The back isomerization from cis- to trans-form happens spontaneously in darkness by the thermal relaxation, or it can be triggered by the visible light. We studied the formation of the complex between laser-synthesized Au nanoparticles and cationic azobenzene containing surfactant (whose structure is presented in Figure 4.3). Gold nanoparticles synthesized by the laser ablation in liquid are of great interest for this kind of applications, because of their pure negatively-charged surface, which enables the electrostatic interaction with positively charged surfactant and the saturation of the particle surface with surfactants molecules.

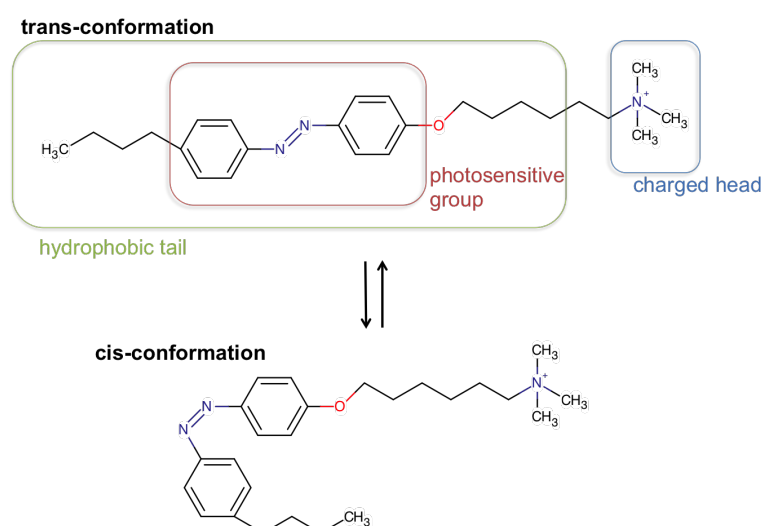


Figure 4.3: Structure of azobenzene-containing photosensitive cationic surfactant and its trans-cis isomerization.

*This study was performed in the collaboration with the research group of Prof. S. Santer, University of Potsdam, Germany.

In our experiments we used 10-nm Au nanoparticles, obtained according to the described in Section 2 femtosecond laser ablation-fragmentation technique. To prepare complexes between Au nanoparticles and azobenzene-containing surfactants, aqueous solutions of both components were mixed and incubated for 30 minutes at room temperature to let them fully react. The maximum of the plasmonic absorption λ_{SP} of the employed pure Au nanoparticles was located at 523 nm (Figure 4.4(A)). The characteristic absorption peaks of trans- and cis-forms of azobenzene-modified surfactants do not overlap with surface plasmon-related absorption peak of Au nanoparticles (Figure 4.4(B)), that allowed us to track the spectral position and intensity of all three peaks: trans-isomer ($\lambda_{trans} = 353$ nm) and cis-isomer ($\lambda_{cis}^1 = 313$ nm and $\lambda_{cis}^2 = 437$ nm) of the surfactant and gold nanoparticles at $\lambda_{SP} = 523$ nm. We used the value of the surfactant loading σ , which designates the number of the surfactant molecules per surface gold atom, and it was calculated as:

$$\sigma = \frac{C_{Azo}}{C_{Au}} \cdot \frac{R}{3d_{Au}} = \frac{C_{Azo}}{C_{Au}} \cdot 5.4,$$

where C_{Azo} and C_{Au} are the molar concentrations of gold atoms and surfactants, R is the radius of a nanoparticle ($R = 5 \pm 1$ nm), and $d_{Au} \approx 0.28$ nm is the diameter of a gold atom. We examined a series of solution with a constant concentration of Au nanoparticles and varying amount of the surfactant, resulting in various σ . At extremely low concentrations of the surfactant ($\sigma = 0.0002$) the plasmon peak of gold nanoparticles remains unaffected. At higher σ values it shifts to the longer wavelengths (from 523 to 527 nm). Surface plasmon effects are extremely sensitive to the refractive index of the local medium. The adsorption of the surfactant on the nanoparticles induces the changes in the refractive index of the medium near the nanoparticles that reflects in the shift of the maximum of the plasmonic absorption. At σ between 0.002 and 0.5, the intensity of the plasmonic peak decreases and a second peak at longer wavelengths (>600 nm) grows with the increasing σ . For even higher concentrations of the surfactant ($\sigma > 0.5$), second absorption peak disappears.

Depending on the ratio between surfactant and Au nanoparticles, the position of the absorption peak and the value of ζ -potential (characterizing the surface charge of the particles) changed (Figure 4.5(A) and (B)). We could identify three regions of the molar ratio, associated to the different complex constitutions. We described the complexes formation with a corresponding phase diagram (Figure 4.5(D)):

- At low surfactant concentrations $\sigma < 0.01$ (region I of the phase diagram in Figure 4.5(D)) gold nanoparticles are still negatively charged, which is illustrated by ζ -potential values. The nanoparticles exist as single specimens and they are only partially covered with surfac-

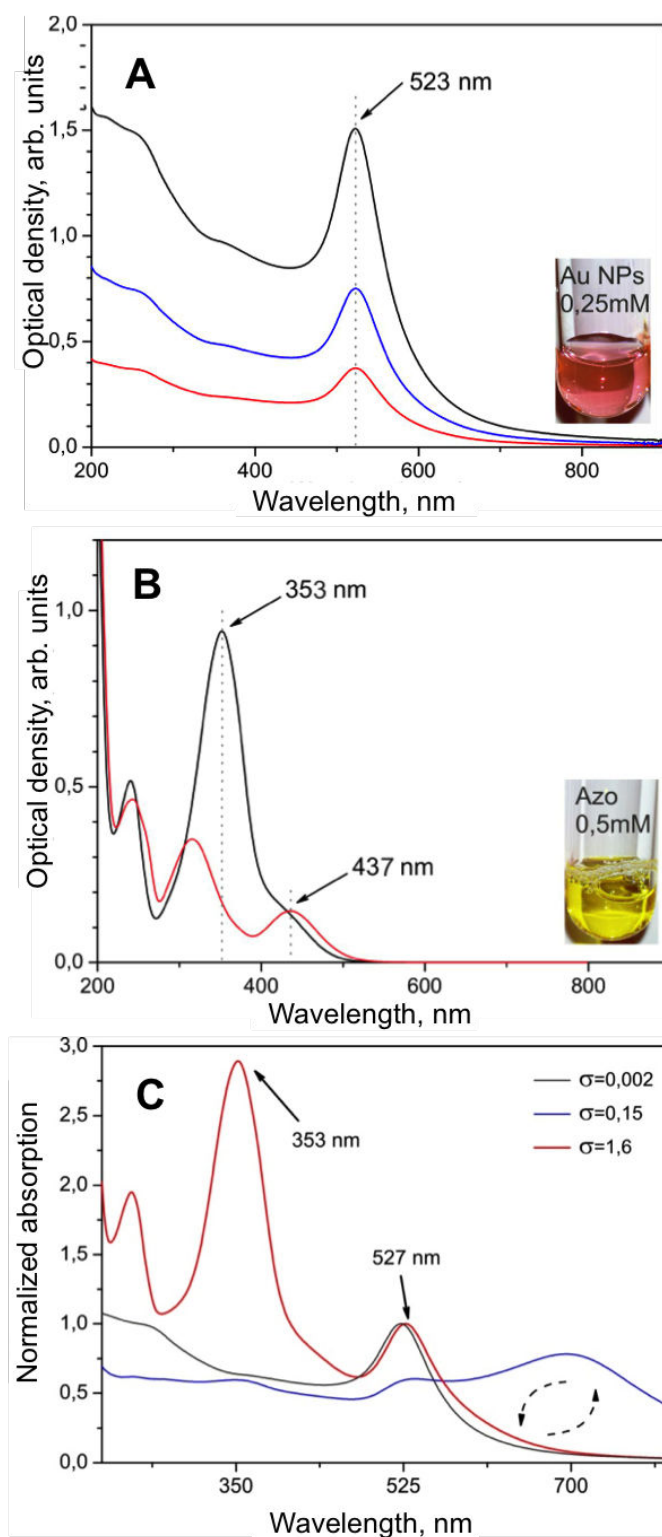


Figure 4.4: UV-Vis absorption spectra of (A) 10-nm laser-synthesized Au nanoparticles at the concentration of gold 0.5 mM (*black*), 0.25 mM (*blue*) and 0.125 mM (*red*), (B) azobenzene containing surfactant at concentration 0.04 mM in trans- (*black*) and cis-conformations (*red*), (C) complexes between 10-nm laser-synthesized Au nanoparticles and azobenzene-containing surfactant at different concentrations of the surfactant (spectra are normalized to the intensity of plasmon peak of the gold at 523 nm). Insets in Figures (A) and (B) show pink color of Au colloids and yellow color of azobenzene-containing surfactant solution.

tant. As one can see on the photographs of the samples (Figure 4.5(C)) at low concentration of the surfactants, the solutions keep the typical pink color of Au nanoparticles.

- On the further addition of the surfactant (region II), the negative charge of the nanoparticles is totally neutralized. We assume that at σ between 0.01 and 0.5 the surface of the particles is saturated with surfactant molecules. The formed complexes are hydrophobic due to the tails of the surfactant that causes the inevitable aggregation of the nanoparticles. It is reflected in the appearance of the second peak in the absorption spectrum at $\lambda > 600$ nm and blue color of the solutions (Figure 4.5(C)), which is often a sign of the formation of large aggregates of gold nanoparticles.
- At high concentrations of the surfactant ($\sigma > 0.5$) the nanoparticles are positively charged. A whole shell of surfactant molecules is assembled and they are situated tail to tail with a cationic group pointing outside (region III of the phase diagram in Figure 4.5(D)). Second absorption peak at long wavelengths disappears, indicating the formation of isolated Au nanoparticles. The color of the solution recovers to initial pink color of Au colloids, and it turns to orange at high σ because of the domination of the color of free azobenzene-containing surfactant. Once the complexes are formed (after a small period of incubation), the binding of the trans-isomer to the gold nanoparticles appears to be rather strong and cannot be reversed by either dilution or change of the net molar ratio of particles and surfactants.

Additionally, we found that the lifetime of the cis-isomer of the azobenzene containing surfactants is significantly changed when it is attached to the gold nanoparticles. The kinetics of the isomerization is shown in Figure 4.6. One can see how the intensity of the peak at $\lambda = 353$ nm, which is characteristic of trans-isomer, increases demonstrating a fast transition of the surfactant back to trans-form in the presence of Au nanoparticles. Upon interaction of the cis-isomers with gold nanoparticles, the thermal relaxation time to the trans-state is less than 2 minutes, while 48 hours is needed for the same process without nanoparticles. This indicates that the surfactant molecules attached to the gold nanoparticles are preferentially all in the trans-conformation.

The surfactants used in our work are photosensitive, thus we can change the structure of the formed complexes and therefore the plasmonic properties of Au nanoparticles. Figure 4.7 shows the absorption spectra of the complexes of Au nanoparticles cis-isomer of azobenzene-containing surfactant before and after UV irradiation. The value of σ in this case was 0.45, that is on the border between regions II and III. The appearance of the peak at 680 nm after 5 minutes of the UV irradiation and change of the color of the solution from pink to blue indicate that our system

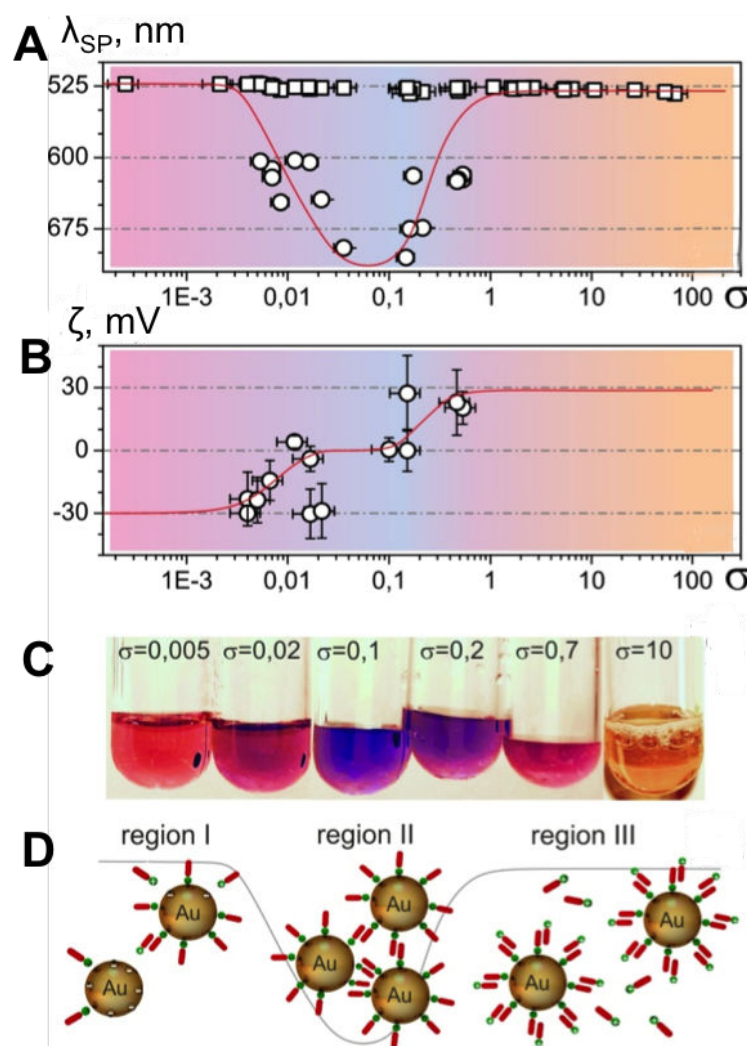


Figure 4.5: (A) Position of the first plasmonic peak at ~ 520 nm (*squares*) and second plasmonic peak at $\lambda > 600$ nm (*circles*), which appears at σ between 0.01 and 0.5, as a function of surfactant loading σ . (B) ζ -Potential of gold-surfactant complexes as a function of surfactant loading σ . (C) Photographs of the solutions of gold-surfactant complexes at various σ . (D) Schematic representation of the configurations of gold-surfactant complexes.

was shifted from region III to region II without altering the total surfactant concentration. We believe that the UV illumination reduces the concentration of the trans-isomers in the surfactant shell covering the nanoparticles, hence the shell around the gold nanoparticles is destabilized. Under the irradiation the trans-isomer turns into the cis-form, which detaches from the stabilizing shell resulting in nanoparticles aggregation.

Thus, we demonstrated that gold nanoparticles produced by the laser ablation can be easily modified with photosensitive polymers, yielding the complexes of various structure, composition and optical properties. The formed complexes can be easily transformed from one into another simply by the irradiation with UV light, that benefits in the perspectives of the creation of light-controlled plasmonic nanosystems.

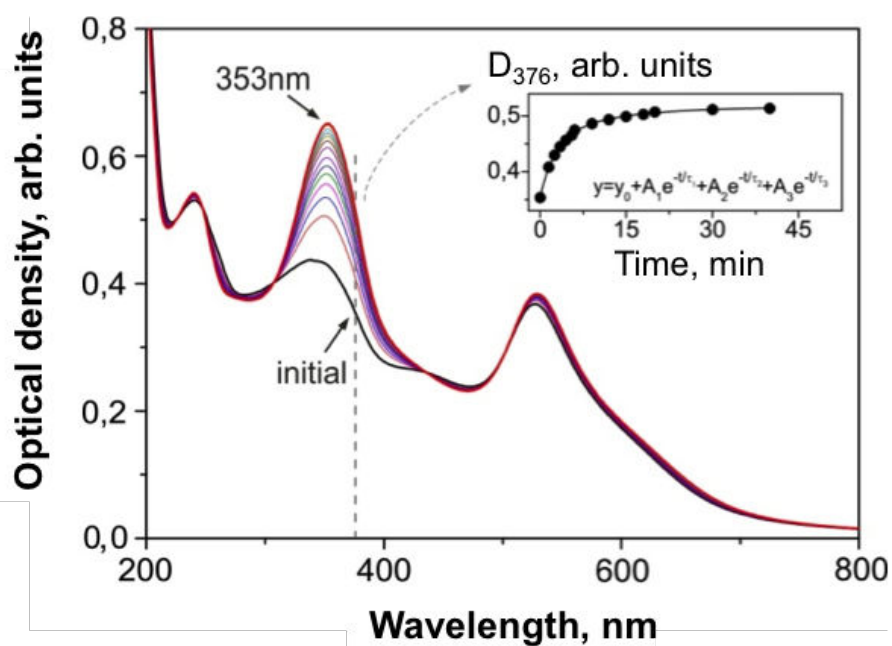


Figure 4.6: Temporal evolution of UV-vis spectra of complexes of gold nanoparticles with cis-isomer of the surfactant. The inset shows the time dependance of the optical density at 376 nm and illustrates fast transition of cis-isomer into trans-form in the presence of Au nanoparticles.

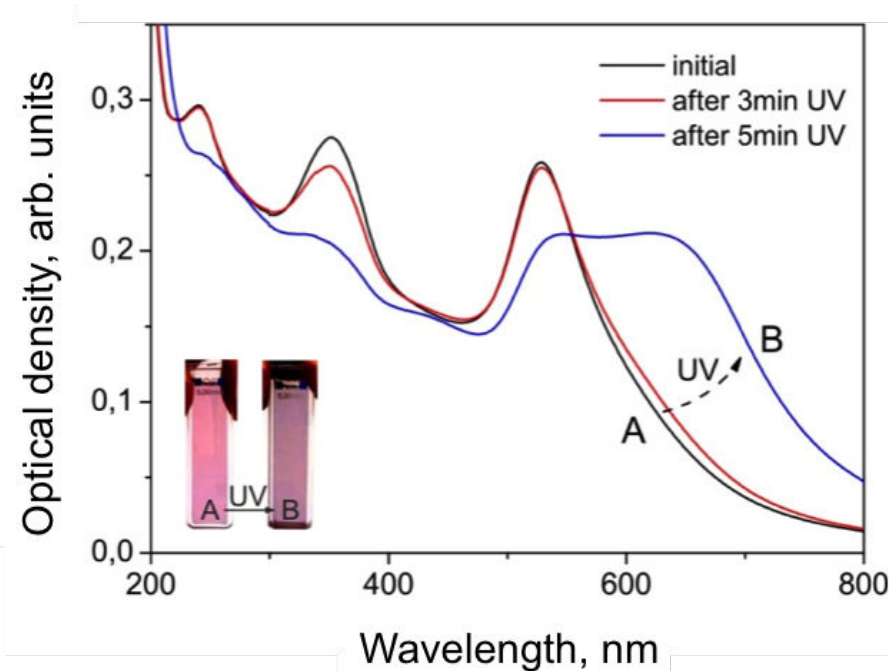


Figure 4.7: UV-Vis absorption spectra of the nanoparticles-surfactant complex at $\sigma = 0.45$ as-prepared (*black*) and after the illumination with UV light (*red* and *blue*). The inset shows change in the color of the nanoparticle-surfactant solution during the UV irradiation.

4.4 Gold nanoparticles for biomedical applications*

Small size, large specific surface area, multiple functionalization possibilities make nanoparticles a promising material for the biomedical applications [278,279], for instance for the vectorization of the molecules (as nanocarriers), for the bioimaging and as terranostic agents [16, 17, 280]. In particular, gold nanoparticles are in the focus of the attention in nanomedicine. Their efficient optical absorption, with typically $\sim 10^5$ -fold higher cross section than absorbing dyes, has been employed for light-induced hyperthermia of solid tumors [270, 281, 282]. Gold nanoparticles can also provide the contrast for cancer imaging through photoacoustic [283] or light scattering [12], as well as mobile surface enhanced Raman scattering-based tags for cancer targeting and diagnostics [272]. However, the issue of the toxicity of employed inorganic nanoparticles always arises [284–286]. The usage of an inappropriate method of synthesis results in the contamination of the nanoparticles with by-products, which in turn causes so-called secondary toxicity of the nanoparticles [48]. Synthesis by the laser ablation can suggest the solution of the problem of the biocompatibility. We examined the toxicological and biological characteristics of Au nanoparticles, prepared by the laser ablation-fragmentation technique. Their potential for the biomedical research was evaluated.

In our test we used three types of gold nanoparticles: monodispersed 20-nm nanoparticles prepared in pure water (Au-NPw), and nanoparticles conjugated with PEG (Au-NPp) and dextran (Au-NPd) according the method described in the Section 2.4. First, the safety of the laser-synthesized gold nanoparticles was verified. The results of the survival of two cancer cell lines (neuroblastoma cell line SK-N-SH and glioblastoma cell line U87-MG) after 72 hours of the incubation with three types of Au nanoparticles are shown in Figure 4.8. All three types of nanoparticles showed no toxicity at all concentrations tested, ranging from 0.1 to 10 000 $\mu\text{g/L}$.

In the terms of future use of Au nanoparticles as drug delivery systems in cancer therapy, we studied the uptake of all three types of laser-produced nanoparticles in living cells. As one can see on TEM images (Figure 4.9(A–C)), Au nanoparticles were internalized in neuroblastoma cells after the incubation for 24 hours independently whether they were covered with a polymer or not. The cell uptake occurs through endocytosis; the TEM micrographs in Figure 4.9(D) and (E) illustrate the moment when the nanoparticles enter a cell inside an endocytotic vesicle. Au nanoparticles could enter both types of cancer cells tested (neuroblastoma and glioblastoma), thus the uptake is not cell type specific. Furthermore, the size of the nanoparticles did not influence the cell uptake neither. We found that all types of laser-synthesized Au nanoparticles

*This study was done in collaboration with research groups of Prof. D. Braguer (CRO2 laboratory, Aix-Marseille University, France) and Prof. M. Gingras (CINaM laboratory, Aix-Marseille University, France). All biological tests were done in CRO2 facilities.

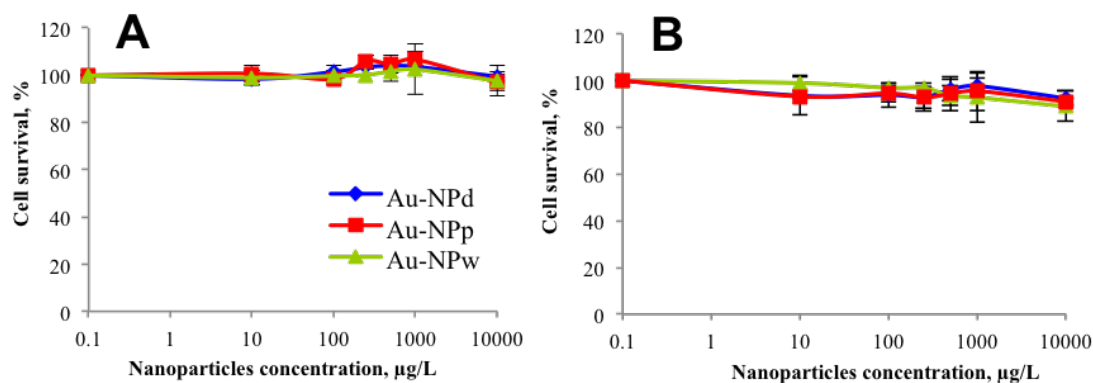


Figure 4.8: Cell survival after 72-h incubation of (A) SK-N-SH neuroblastoma cells and (B) U87-MG glioblastoma cells with Au nanoparticles prepared in pure water (Au-NPw), capped with dextran (Au-NPd) and PEG (Au-NPp).

tested, bare or coupled with dextran or PEG, with size ranging from 5 to 20 nm could enter human cancer cells.

The behavior of the nanoparticles in biological media should be also studied in order to evaluate the feasibility of the usage of the laser-synthesized nanoparticles *in vivo*. When the nanoparticles are incubated in biological fluid, for example in a culture media containing the serum, proteins bind to the nanoparticles surface to make a protein corona. We found that stable protein corona is formed on the surface of all the three types of tested nanoparticles already after 30 minutes of the incubation. We also examined the composition of the protein corona by the mass-spectroscopy. About 100 different proteins were adsorbed on the surface of dextran-coated nanoparticles, against almost 80 for PEGylated and bare nanoparticles (Figure 4.10(A)). The most abundant protein was serum albumin, its content was 25% of the total amount of proteins for Au-NPd and ~10% for Au-NPw and Au-NPp (Figure 4.10(B)). The serum protein is hydrophobic and could facilitate the stability of hydrophobic drug-nanoparticles complex. Moreover, complexation with albumin enables to prolongate the nanoparticles circulation time in blood [287]. In addition to albumin, apolipoproteins (Apo) were bound at the surface of the nanoparticles, especially a higher amount of this kind of proteins was observed in the case of dextran-coated Au particles (Figure 4.10(C)). These proteins are involved in intracellular trafficking and they allow crossing some biological barriers. Apolipoprotein E (ApoE) and apolipoprotein A-I (ApoA-I) bound to a nanoparticle enable their interaction with some brain endothelial cells [288]. Hence the binding with proteins can make the nanoparticles able to cross blood-brain barrier. Together with their ability to enter glioblastoma cells, we can suggest them as good candidates for brain tumor treatment.

Coagulation proteins (*e.g.* fibrinogen, antithrombin III, coagulation factor VIII, hemoglobin) and complement C3 were also found on the surface of all three types of nanoparticles. At the

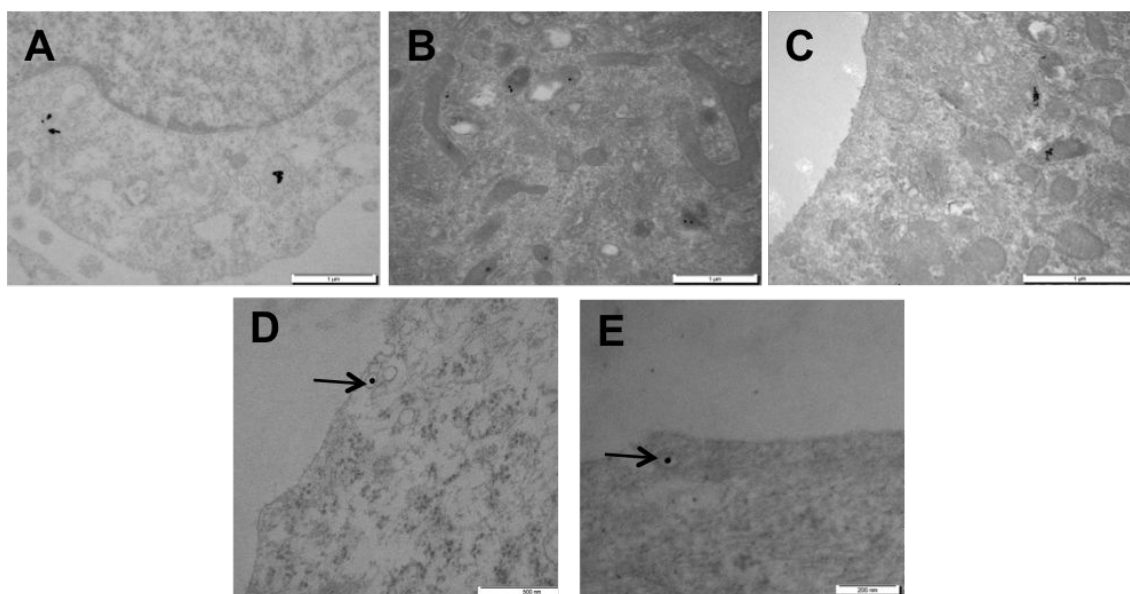


Figure 4.9: TEM images of neuroblastoma cells incubated with different types of laser-synthesized nanoparticles: (A) bare, conjugated with (B) PEG and (C) dextran. TEM images of bare Au nanoparticles enclosed in edocytic vesicles close to the cell membrane in (D) neuroblastoma and (E) glioblastoma cells.

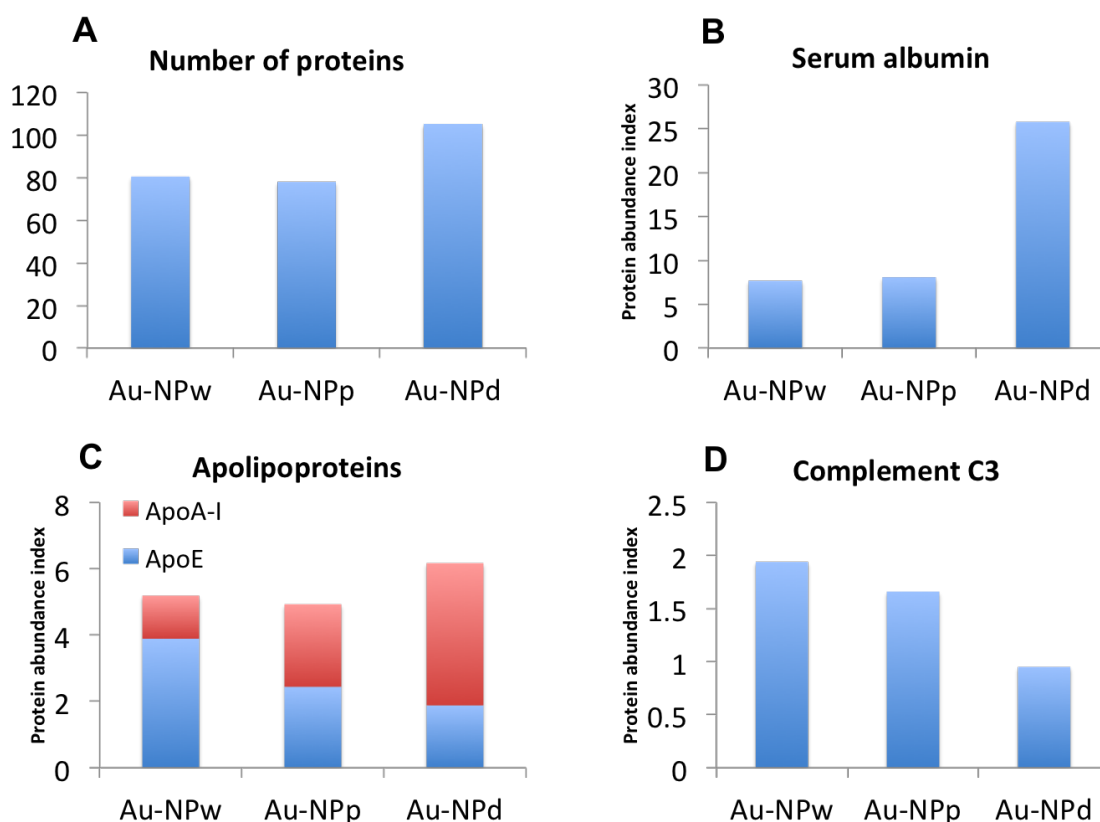


Figure 4.10: Histograms representing the composition of protein corona on the surface of three types of nanoparticles: produced in pure water (Au-NPw), capped with PEG (Au-NPp) and dextran (Au-NPd). (A) Total number of proteins adsorbed of the surface of the nanoparticles. Amount of (B) serum albumin, (C) apolipoprotein A-I (ApoA-I) and apolipoprotein E (ApoE) and (D) complement C adsorbed on different Au nanoparticles.

same time less complement C3 was adsorbed at the surface of dextran-coated nanoparticles, compared to bare and PEGylated particles (Figure 4.10(D)). Binding complement factors and fibrinogen are known to promote the ingestion of the particles by the phagocytes, and the eventual removal of the particles from the systemic circulation by the cells of microphage system. Then particles are rapidly sequestered from this kind of cells and accumulated in liver and spleen [289]. Thus, lower amount of complement C3 adsorbed on the dextran-coated Au nanoparticles make us believe that it might limit the hepatic accumulation of gold and subsequent liver toxicity.

To conclude, gold nanoparticles prepared by femtosecond laser ablation were proven to be biologically safe and biocompatible, and they can be easily internalized inside human cancer cells. The rapid formation of the protein corona on the surface of the nanoparticles plays an important role in the biological behavior of the nanoparticles. Thus, we demonstrated that laser-synthesized nanoparticles, pure and *in situ* modified with biocompatible polymers, can be a promising material for cell targeting and delivery of nanoparticle-drug conjugates to fight cancer with a nanomedicine approach.

4.5 Si nanoparticles for radio-frequency radiation-induced hyperthermia*

An ability of radio frequency (RF) to heat human tissues is known for a long time. The efficiency of RF-based cancer therapy can be enhanced by using sensitizers, specially designed agents, which are targeted into a tumor area, then absorb RF radiation to heat cancer cell and induce their selective destruction. Such effect can be achieved by using electrically-conductive nanoparticles [290, 291]. It is considered that the nanoparticles produce Joule heating through RF-induced generation of local electrical currents over a particle volume [290]. The employment of Si nanoparticles for cancer treatment tasks can bring a number of advantages. Si nanoparticles are known to be biocompatible [292], and besides in biological tissues Si nanoparticles are dissolved to orthosilicic acid $\text{Si}(\text{OH})_4$, which is normally extracted from the body with urine [28]. Second, Si nanoparticles possess a series of unique properties, such as room temperature photoluminescence [28, 292] and singlet oxygen generation [292] under photoexcitation, suggesting the possibility to combine RF hyperthermia with diagnostics and other treatment modalities.

In our work we tested RF-induced properties of 25-nm Si nanoparticles, produced by the laser ablation according the methodology described in Chapter 3, and evaluated the prospects of

*This work was done in collaboration with groups of Prof. V. Timoshenko, Lomonosov Moscow State University, Russia and Prof. A. Ivanov, Blokhin Cancer Research Center, Moscow, Russia. All biological tests were performed in the Blokhin Cancer Research Center.

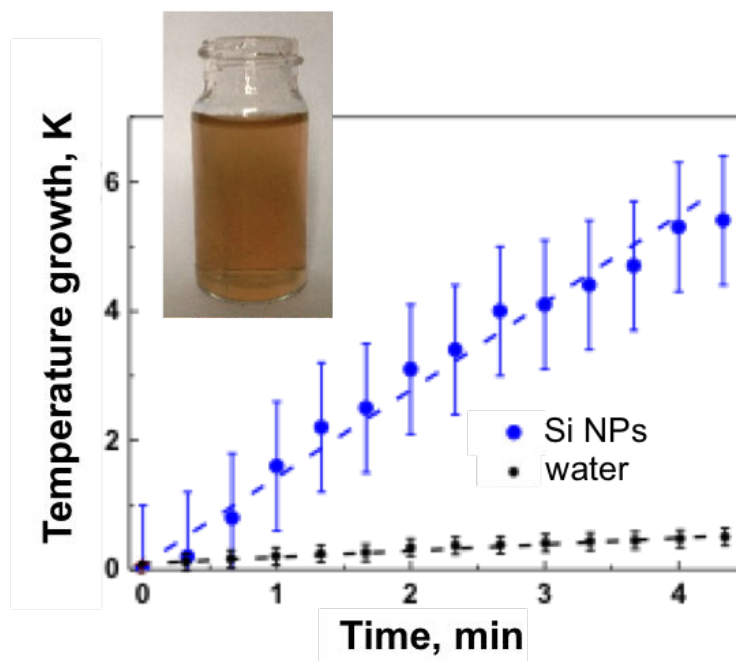


Figure 4.11: Temperature growth of aqueous colloid of laser-synthesized Si nanoparticles at concentration of 12 mg/L (*blue*) and distilled water (*black*) under RF irradiation with intensity 5 W/cm². The inset shows a glass vial with Si nanoparticles produced by the laser fragmentation of Si powder in water.

the application of laser-synthesized Si nanoparticles in RF-induced hyperthermia cancer treatment. Figure 4.11 shows the time dependence of the temperature growth of Si nanoparticles colloids and deionized water for comparison under the exposure to radio frequency irradiation with intensity of 5 W/cm². Estimated heating rate of the Si nanoparticles solution at the concentration of ~12 mg/L was 1.3 K/min, while for deionized water this value was 0.7 K/min. Previously published works on RF radiation-induced heating of gold nanoparticles reported the heating rate ~1.7 K/min for considerably more concentrated solutions (~50 mg/L) [290, 293]. Thus, Si nanoparticles exhibit similar heating rates as gold nanoparticles, which are widely used for hyperthermia applications. However, Si-based nanoparticles are characterized by poor electrical conductivity, compared to Au-based particles. We suppose that Joule heating under RF irradiation occurs because of the local electric currents around the nanoparticles rather than over nanoparticles volume. In the electric field of RF radiation the nanoparticles-solution interface is rapidly polarized and then an electrical double layer around a nanoparticle is formed. This model is independent of bulk electrical conductivity of nanoparticles and it explains effective Joule heating of weakly conductive Si nanoparticles.

As a first step to the application of the nanoparticles *in vivo* we evaluated *in vitro* cytotoxicity of laser-synthesized Si nanoparticles. Human Hep-2 cells were incubated for 24 hours with colloidal solutions of 25-nm Si nanoparticles produced by the laser fragmentation of Si powder in water. As a control we used phosphate buffered saline (PBS), which normally has no effect

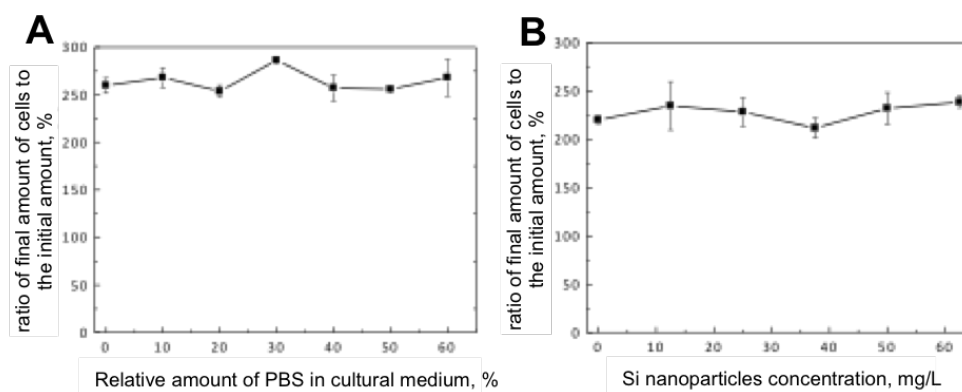


Figure 4.12: Viability of human Hep-2 cells in cultural medium (A) without and (B) with Si nanoparticles.

on the cells viability. The results are shown in Figure 4.12. As one can see, Si nanoparticles do not influence the cells proliferation in the tested range of concentrations. A slight difference in absolute values of the ratio between final and initial amounts of cells in the case of laser synthesized Si nanoparticles and control sample is explained by taking into account that cell cultures for the experiments were taken at different (but close) points of cell proliferation curve. In conclusion, Si nanoparticles produced by laser ablation are safe for human cells, when no additional treatment is employed.

We also studied *in vitro* the cumulated effect of Si nanoparticles and RF radiation on the living cells. Optical image in Figure 4.13(A) demonstrates 3T3 fibroblast cells treated only with RF radiation (1 min, 2 W/cm²). Obviously, radio frequency radiation itself does not harm the cells, just like the nanoparticles, as we showed above. In contrast, the image in Figure 4.13(B) illustrates the effect of RF radiation on the cells incubated with a solution of laser-synthesized Si nanoparticles. After the RF radiation in the presence of Si nanoparticles, only large Si agglomerates with parts of dead cells can be seen. This result demonstrates perfectly the potential of the RF radiation-induced hyperthermia enhanced by the Si nanoparticles produced by laser ablation. Importantly, two components of the hyperthermia therapy (nanoparticles and RF radiation) are harmless for the living cells when they are applied separately, which enables an efficient targeted treatment of a tumor with minimal side effects.

To verify the consistency of the proposed therapy approach we carried out *in vivo* tests of hyperthermia treatment of cancer tumors using small animal model. Aqueous colloids of Si-based nanoparticles or equal volumes of a sterile water (as a control) were injected into the lung carcinoma (3LL) tumors located in the mice. 15 – 20 minutes later the mice were immobilized and subjected to RF radiation for 2 minutes. Just after the RF irradiation the tumors, which were treated beforehand with Si nanoparticles as sensitizers, experienced a disaggregation and

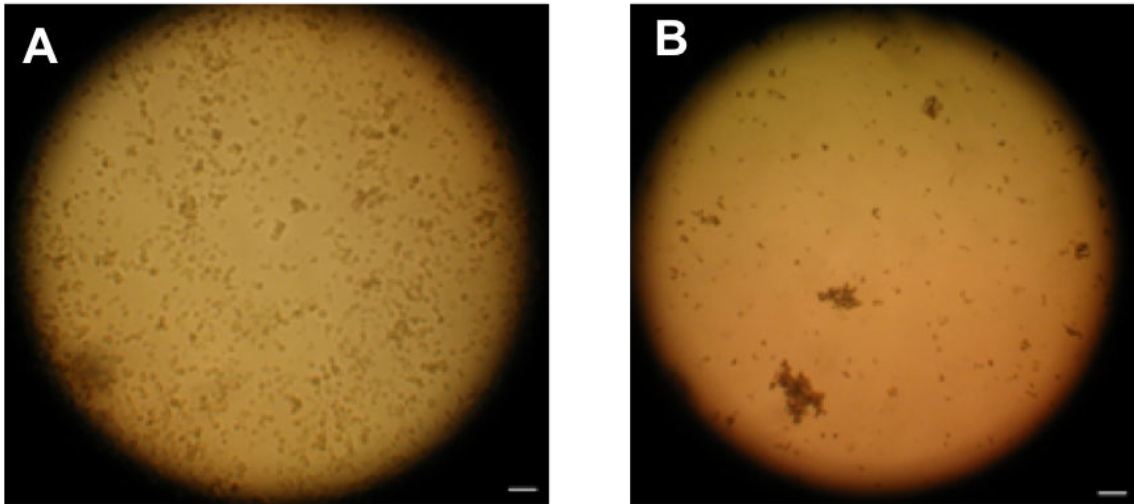


Figure 4.13: Optical large-scale images of 3T3 fibroblast cells (A) after RF irradiation (1 min, 2 W/cm²) and (B) the same after the incubation with laser-synthesized Si nanoparticles followed by the RF irradiation. The scale bars correspond to 100 μ m.

it progressed for next several days after the hyperthermia treatment procedure. The results of the treatment were quantified by the evolution of total volume occupied by tumor cells. The inhibition of tumor growth was calculated as:

$$\text{Inhibition} = \left(1 - \frac{V}{V_0}\right) \cdot 100\%,$$

where V and V_0 are the averaged tumor volumes for the experimental and control groups of mice, respectively. The positive value of inhibition indicates the suppression of tumor growth, while negative one means that the average tumor volume of the exposed mice was bigger than in the control group. For in *in vivo* tests we used two types of Si nanoparticles: 25 nm in diameter, produced by the laser fragmentation of Si powder in water (abl. Si), and nanoparticles obtained by mechanical milling of electrochemically-prepared porous silicon (PSi). Porous Si nanoparticles used in our experiments were larger, with a mean size of ~ 50 nm, wide size-dispersed with a significant fraction of bigger (up to several hundreds of nm) and of irregular shape. As shown in Figure 4.14, PSi nanoparticles can slightly inhibit the tumor growth themselves. This can be explained by the toxic effect of free radicals and residues from the electrochemical etching process, remaining on the surface of the particles. Similar slight inhibition of tumor growth took place under the action of RF radiation alone, which is consistent with previous studies [294–296]. However, the combined action of Si nanoparticles and RF radiation could drastically amplify the effect leading to a much stronger inhibition of the tumor growth. This effect was observed both for laser-synthesized and PSi nanoparticles. Besides, in the case of laser-produced nanoparticles the inhibition of the tumor growth was even more considerable, while the dose and the concentration

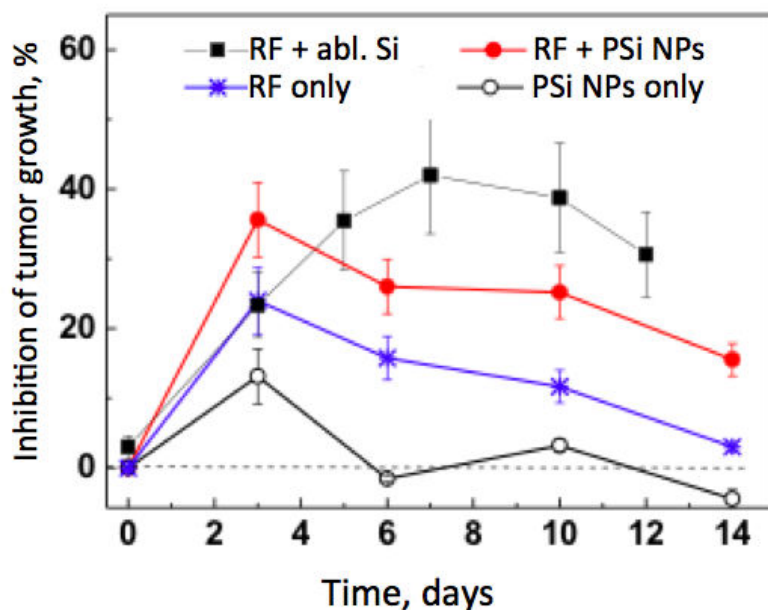


Figure 4.14: Inhibition of the tumor growth after the various treatments: *open circles* – injection of solution of PSi nanoparticles (0.5 mL, concentration 1 g/L); *blue stars* – RF radiation only; *red circles* – injection of solution of PSi nanoparticles (0.5 mL, concentration 1 g/L) followed by RF irradiation; *black squares* – injection of laser-produced Si nanoparticles (0.2 mL, concentration 0.4 g/L) followed by RF irradiation.

of the nanoparticles solutions were lower, compared to those for PSi particles (Figure 4.14).

The obtained results show that Si-based nanoparticles can serve as an efficient sensitizers for the RF-induced cancer therapy. We believe that the observed effect of the suppression of the tumor growth can be attributed to a local hyperthermia-based destruction of cancer cells due to the RF-induced heating sensitized by the Si nanoparticles. Laser-synthesized particles look especially promising for these tasks. First, due to their even higher activity in RF-related tumor suppression, compared to PSi. And second, because they do not contain any residual contaminant on their surface [60], they are characterized with ideal round smooth shape, controlled mean size and low size dispersion that allows their better delivery and uptake *in vivo*.

4.6 Au and AuPd nanoparticles as electro-catalyst*

We studied the potential of the application of laser-synthesized Au and AuPd alloy nanoparticles as an electro-catalyst of glucose oxidation for biofuel cell applications. Typical biofuel cells are designed to convert the chemical energy of biofuels (such as sugars or ethanol) into electrical energy via electrochemical reactions with the help of enzymes [297–299]. A principle scheme of a biofuel cell is shown in Figure 4.15. An anode reaction includes the oxidation of the organic

*This work was done in collaboration with the group of Dr. T.W. Napporn, IC2MP (Institut de Chimie des Millieux et Matériaux de Poitiers), Poitiers University, France. All electrochemical test were done in IC2MP facilities.

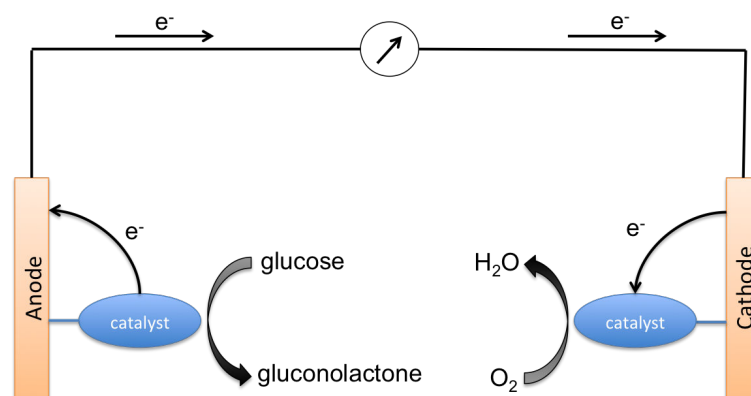


Figure 4.15: Scheme of a biofuel cell based on the glucose oxidation.

fuel (glucose is the most often used one); a cathode reaction implies the reduction of the oxygen to H_2O . Normally enzymes are used for both types of the reaction. However, the employment of the enzymes is related to several difficulties, such as the necessity of the immobilization and stabilization of the enzymes, lower efficiency of the electron transport in comparison to metallic catalysts, and short active lifetime [297]. The alternative to classical enzymatic biofuel cells is hybrid schemes, in which abiotic catalyst is used to oxidize glucose instead of enzymes [300]. The pure noble metal nanoparticles are of particular interest because of their good catalytic activity, which originates from high energy surface states [49,301]. Thus, the performance of nanoparticle-based electrode depends on their surface conditions, namely the purity of the nanoparticles.

We examined the catalytic properties of Au nanoparticles obtained by the laser ablation followed by the femtosecond laser fragmentation (according to the developed method, described in Chapter 2) towards the electrooxidation of glucose using cyclic voltammetry (CV). For the comparison the same tests were made with chemically-synthesized Au nanoparticles (CS-Au NPs). The evolution of the first ten cyclic voltammograms of chemically synthesized nanoparticles and first and second cycles of the nanoparticles prepared by laser ablation (LA-Au NPs) are shown in Figure 4.16. As follows from the Figure 4.16, the chemically synthesized nanoparticles demonstrate a very low electrochemical response for the first CV cycles, which is related to the contamination with organic molecules adsorbed on the surface of the nanoparticles, inevitable during the chemical synthesis. Nevertheless, the current densities corresponding to the oxide formation increase from the first to the tenth cycle showing a gradual cleaning of such nanoparticles. In contrast, laser-ablated nanoparticles (LA-Au NPs) demonstrate excellent electrochemical response starting from 1-2 CV cycles, suggesting an exceptional purity of LA-Au NPs (Figure 4.16). In fact, the tenth cycle of CS-Au NPs is similar to the first-second cycle of nanoparticles prepared by laser ablation. It is important that LA-Au NPs demonstrate excellent oxidation properties from the very first cycles due to their high purity and the absence of

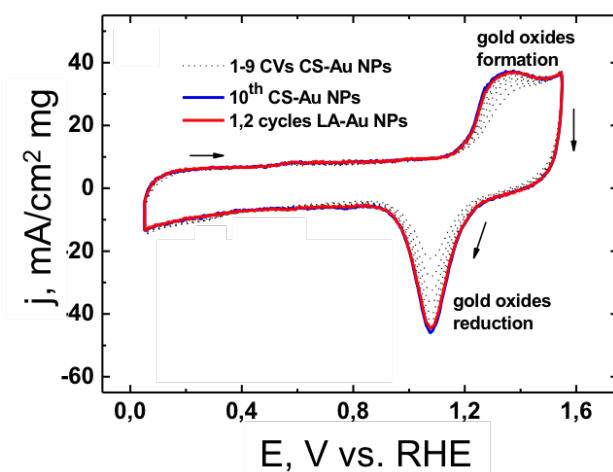


Figure 4.16: Cyclic voltammograms using electrodes formed by laser-ablated (LA-Au NPs, red) and chemically-synthesized (CS-Au NPs, 1-9 cycles indicated by dotted black, 10th cycle by blue) nanoparticles in 0.1 mol/L NaOH recorded at 20 mV/s and at controlled temperature of 25 °C.

chemical species adsorbed on the surface.

Figure 4.17 represents the cyclic voltammogram of the AuNPs electrode in alkaline medium containing glucose. The first peak is associated with the oxidative transformation of glucose to gluconolactone [302, 303]. Then the lactone is successively oxidized in the broad potential from 0.8 to 1.35 V with oxidation maximum at $E_p = 1.2$ V vs. reversible hydrogen electrode (RHE). The corresponding current density is 2.65 A/cm²·mg that equates 65 A/g of mass activity. This value of catalytic activity is 3.3 and 2.6 times higher than those found in the literature for Au/Vulcan and Au₇₀Pt₃₀/Vulcan bimetallic catalyst (the best from these kinds of catalysts) synthesized by chemical method [304] and highly improved compared to others [305, 306].

Other noble metals nanoparticles can also exhibit catalytic properties towards biofuel cell applications. In particular, Pt and Pd are effective in the reaction of the glucose oxidation to gluconolactone due to their dehydrogenating capacity [307–310]. Pd is considered as especially perspective catalytic material, because it is 50 times more abundant on the earth [310] and two times less expensive than Pt, while having similar dehydrogenating properties [307, 308, 310]. The addition of Au to Pd significantly increases the catalytic activity and poisoning tolerance of Pd electrocatalysis [309, 311–313]. In view of the unique catalytic properties of nanoscale gold and the high catalytic hydrogenation/dehydrogenation activity of palladium, Pd-Au bimetallic nanoparticles of controllable composition may serve as a synergetic catalyst system [314–318].

We have synthesized bimetallic AuPd nanoparticles by the co-fragmentation of the colloids prepared by the laser ablation of a solid metallic target. By varying the ratio between initial Au and Pd nanoparticles, we obtained the nanoparticles of various composition, in particular

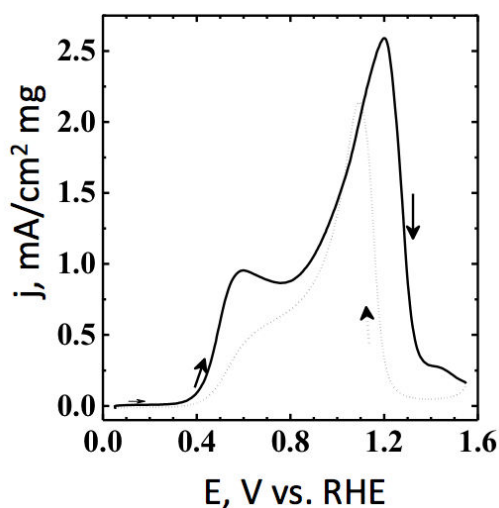


Figure 4.17: Voltammogram of the AuNPs electrode in 0.1 mol/L NaOH recorded at 20 mV/s and at 25 °C in the presence of 10 mmol/L glucose.

Pd₅₀Au₅₀ and Pd₈₀Au₂₀ nanoparticles with the Au:Pd ratio 1:1 and 1:4 respectively. The composition was confirmed by the energy-dispersive spectroscopy (EDS). It should be noticed that no surfactants or other extraneous substance were used during the laser synthesis, ensuring the purity of the nanoparticles surface and that of catalytic sites. Laser-synthesized bimetallic AuPd and pure Pd nanoparticles of various composition were used as an unsupported anode catalyst for the glucose electrooxidation in alkaline medium.

Figure 4.18 shows the voltammograms of Pd and bimetallic catalysts in alkaline glucose solutions. During the positive going sweep rate a shoulder at ~0.6 V is followed by the main oxidation peak centered at 0.8 V vs. RHE. One can see that the current densities increase with the increasing of the Au content in the nanoparticles: 10 A/g on Pd, increases twofold on the Pd₈₀Au₂₀ electrode and reaches ~60 A/g on the Pd₅₀Au₅₀ catalyst. As a result, the Pd₅₀Au₅₀ nanoparticles exhibit the best electroactivity among the anode materials synthesized towards the glucose oxidation. It can be stated that Au content promotes remarkably palladium anodes in the glucose oxidative reaction process when taking into account the current at Pd-only (28 A/g herein at 0.8 V). More importantly, the current densities obtained herein at 0.8 V vs. RHE for Pd₅₀Au₅₀ nanoparticles are 2.4 times higher than those found recently under the same electrochemical conditions on the Au₇₀Pt₃₀/C catalyst prepared from a soft chemical method [304]. Additionally, the dehydrogenating properties of Pd allow performing the oxidation of the glucose at lower potential, compared to pure Au nanoparticles, hence leading to higher voltage in the application in biofuel cells.

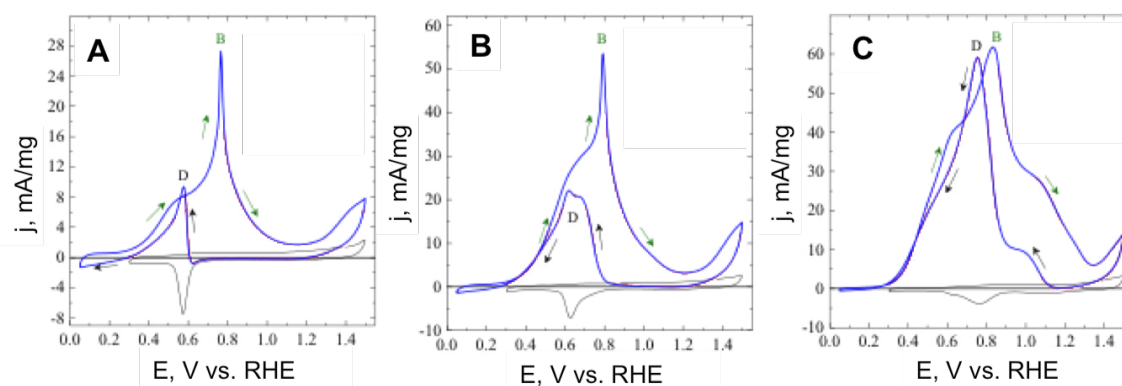


Figure 4.18: Cyclic voltammograms of (A) Pd, (B) Pd₈₀Au₂₀ and (C) Pd₅₀Au₅₀ electrodes recorded at 20 mV/s and at 25 °C in a 0.1 mol/L NaOH solution containing 10 mmol/L glucose.

4.7 Conclusion

We prepared bare and functionalized Au- and Si-based nanoparticles by the femtosecond laser ablation-fragmentation according to the techniques developed in our work, and assessed their potential for important biomedical and electrocatalytic applications. Our tests revealed a series of unique properties of laser-synthesized materials, which include:

- SERS and fluorescence quenching on the surface of Au nanoparticles are improved due to their uncontaminated nature.
- Bare surface of laser-produced Au nanoparticles enables their easy functionalization and complexation with photosensitive surfactants, leading to the formation of light-controlled plasmonic nano-architectures.
- The absence of residual contamination of pure and polymer-protected Au nanoparticles synthesized by the femtosecond laser ablation make them innocuous for human cells. At the same time Au nanoparticles can easily enter the cells. Besides they interact with biological media, forming a protein corona around the nanoparticles, which in its turn may facilitate the internalization into the cells and crossing the physiological barriers. It illustrates the prospects of the utilization of laser-produced Au nanoparticles for biomedicine and as drug-carriers.
- Laser synthesized Si nanoparticles themselves are harmless for the human cells. However, under radio frequency irradiation they exhibit Joule heating, which can induce the inhibition of the tumor growth *in vivo*. Thus, even without any special modification or targeting, Si nanoparticles behave as promising sensitizer for radio-frequency induced hyperthermia therapy.

- Pure surface of Au and AuPd laser-synthesized nanoparticles increase their catalytic activity for the glucose electrooxydation.

Conclusion

The aim of this thesis was the development of novel laser-ablative approaches for the fabrication of Au and Si nanoparticles for biomedical applications. In view of the potential applications, the purity of the obtained nanomaterials and the possibility of controlling their size and composition are of main importance. In our work, we managed to overcome the challenges of the controlled manipulation of the nanoparticles parameters by the using of ultrafast laser ablation.

We used two configurations of laser-ablation synthesis of Au nanoparticles: femtosecond laser ablation from a solid target in aqueous media and femtosecond fragmentation of the colloidal solutions. The first geometry served us to prepare primary solutions of pure Au particles and the second one allowed us to improve size characteristics and stability of the prepared colloids. We elucidated the influence of the experimental parameters, such as focusing conditions and laser pulse energy, on the properties of the obtained nanoparticles. In particular, we demonstrated that the variation of the incident laser energy during the fragmentation step enables an efficient size control of the particles in the range of 7-50 nm in the absence of any ligands. In addition, we applied the femtosecond laser ablation for the synthesis of the complexes of Au nanoparticles with polymers and oligosaccharides and AuPd bimetallic nano-alloys, which are of great interest for catalytic and biomedical applications.

On the other hand, we introduced a new method for a fast synthesis of ultrapure Si-based nanoparticles based on femtosecond laser ablation from preliminary prepared water-dispersed microcolloids. This method yields stable concentrated solutions of spherical and low size-dispersed Si nanoparticles with prominent fluorescence characteristics. Furthermore, this method offers an easy and efficient control of the size and surface composition of the produced nanoparticles by adjusting the conditions of laser ablation. In particular, changing the initial concentration of the microcolloids allowed us to vary the size of the nanoparticles from 1–2 to 30–40 nm. This technique can be combined with the variations of the pH of the solutions in order to achieve more precise tuning of the nanoparticles size. Moreover, by changing the amount of dissolved oxygen, we can vary the depth and the composition of the oxide layer.

Finally, we assessed the potential of laser-synthesized Au and Si nanoparticles for a series of

applications in biomedicine and electrocatalysis. First of all, we demonstrated the innocuity of the produced nanoparticles for living cells. We then showed that in biological media a protein corona is formed around pure and polymer-protected Au nanoparticles, facilitating the internalization of laser-synthesized particles by the cells. Furthermore, Si nanoparticles produced by the laser ablation exhibited excellent sensitizing properties for radio-frequency induced hyperthermia therapy. The range of potential biomedical applications of laser-synthesized was also supplemented by the possibility of using gold nanoparticles for SERS spectroscopy and fluorescence lifetime imaging microscopy. In addition, we demonstrated that bare surface of laser-produced Au nanoparticles allows their easy functionalization with photosensitive surfactants enabling the fabrication of light-controlled plasmonic nano-devices. Finally, we demonstrated that due to the unique bare surface of laser-synthesized Au and AuPd nanoparticles they manifest exceptional catalytic properties for the electrooxidation of glucose, opening the way for the development of efficient biofuel cells.

We believe that the obtained results on the laser synthesis of novel biocompatible nanomaterials and their successful tests in biological models can provide an important basis for future development of laser-ablative nanofabrication methods. It should be noted that our study was mainly focused on the synthesis of Au- and Si-based nanomaterials. However, the general strategies for nanoparticles synthesis proposed in our work can be extended toward the fabrication of other types of metal and oxide nanoparticles. In addition, future works should address the clarification of the following phenomena:

- Physical aspects of inorganic nanoparticle growth are not completely understood. In particular, more data should be obtained on mechanisms of laser ablation and cluster growth, impact of cavitation phenomena, energetic and angular distribution of nanoclusters, *etc.*
- Chemical properties of laser-synthesized nanomaterials are not yet well studied. The uniqueness of laser-ablative synthesis consists in the possibility of achieving “bare” nanoparticle surfaces. Furthermore, the laser-synthesized nanomaterials can have quite different surface chemistry compared to classical chemical counterparts. The chemistry of laser-synthesized inorganic nanomaterials still remains a “white spot” requiring further detailed investigation.
- The interaction of laser-synthesized materials with biological systems should be studied in more detail, although our first results are extremely encouraging.

In general, we anticipate the following directions for the future advancement of laser-ablative approach: (i) synthesis of nanomaterials with unique size and structural characteristics, which

are not reproducible by conventional colloidal chemistry; (ii) “green” synthesis of various nanomaterials; (iii) employment of novel chemical approaches due to different surface chemistry of laser-synthesized nanoparticles compared to chemically-synthesized counterparts. From the application standpoint, the laser-synthesized nanomaterials promise a breakthrough in the solution of toxicity problem in *in vivo* applications of inorganic nanoparticles and a significant advancement of nanoparticle-based modalities of biological imaging and therapy. The laser ablation-based approach is unique in avoiding secondary toxicity arising when chemical synthesis is used to make nanoclusters. Therefore, it is especially effective in the case of nanomaterials, which are biocompatible by their nature. This includes the fabrication of some semiconductor, metal NPs, as well as hybrid structures (alloys, core-shells, organic-inorganic complexes). In addition, the development of biological imaging or treatment methods employing nanoparticles can profit from novel optical, chemical and photochemical properties of the laser-synthesized nanomaterials.

As future trends of laser-ablative nanosynthesis for biomedical applications, we see the following:

- Production of novel non-toxic, biocompatible and biodegradable materials;
- Improvement of optical characteristics (*e.g.*, maximization of quantum yield of fluorescence and singlet oxygen release in photo dynamic therapy, improvement of sensitivity in biosensing relying on refractive index monitoring);
- Exploration of novel optical properties, which could provide contrast in imaging;
- Synthesis of theragnostics agents, capable of simultaneously providing imaging and therapeutic tools;
- Creation of complex biomolecular architectures, providing improved sensitivity (contrast) and novel functionalities (*e.g.*, size selection in sensing, additional channels in sensing and imaging, *etc.*)

Appendix A

Plasmonic properties of Au nanoparticles

The deep-red color of Au nanoparticles in aqueous solutions reflects the surface plasmon band, a broad absorption band in the visible region around 520 nm. The surface plasmon band is related to excitation of the collective oscillations of the electron gas at the surface of the nanoparticles upon to the interaction of Au nanoparticles with the electromagnetic field of light, exhibiting a resonance frequency at 510–550 nm depending on the size of the nanoparticles.

The classical interaction of the nanoparticles with incident light and the resulting optical properties are described by an electromagnetic function ϵ . Often it is represented as a function of the angular frequency of light $\omega = 2\pi c/\lambda$ (where λ is wavelength and c is the speed of light in vacuum). The dielectric function of gold is defined as the sum of the inter band term, $\epsilon_{\text{IB}}(\omega)$, which considers the response of 5d electrons to the 6sp conduction band, and the Drude term, $\epsilon_{\text{D}}(\omega)$ which considers free electrons according to Drude model (6s electrons of the conduction band of gold). Thus, dielectric function can be determined as:

$$\epsilon(\omega) = \epsilon_{\text{IB}}(\omega) + \epsilon_{\text{D}}(\omega) \quad (\text{A.1})$$

The localized surface plasmon resonance, representing the optical properties of gold, originates from the photoexcitation of free electrons, *i.e.* the second term in the equation. Each term of the dielectric function is divided into a real part ($\epsilon_1(\omega) = n^2 - \kappa^2$) and an imaginary part ($\epsilon_2(\omega) = 2n\kappa$), where n represents the refractive index and κ — the extinction coefficient of the metal [160].

Plasmonic nanoparticles with the diameter less than the electron-mean-free path (~ 40 nm for Au) allow the confinement of free electrons. According to the simplest model, the electrons

are damped by a inelastic scattering process at the inner surface of the nanoparticles, resulting in an increased relaxation frequency or a higher damping constant Γ : the relaxation time of the free-electron gas is reduced. Accordingly, the dielectric function of a bulk metal has to be modified, giving rise to a size-dependent dielectric function $\epsilon(\omega, R)$:

$$\epsilon(\omega, R) = \epsilon^{\text{bulk}}(\omega) - \epsilon_{\text{D}}^{\text{bulk}}(\omega) + \epsilon_{\text{D}}(\omega, R) \quad (\text{A.2})$$

In this equation $\epsilon^{\text{bulk}}(\omega)$ describes the dielectric function of bulk gold calculated from n and κ , which can be found experimentally. In order to obtain a size-dependent dielectric function, Drude's dielectric function of a free electron gas of bulk metal ($\epsilon_{\text{D}}^{\text{bulk}}(\omega)$, second term) is replaced by the one for a nanoparticle with radius R ($\epsilon_{\text{D}}(\omega, R)$, third term in the equation). $\epsilon_{\text{D}}^{\text{bulk}}(\omega)$ and $\epsilon_{\text{D}}(\omega, R)$ can be found as:

$$\epsilon_{\text{D}}^{\text{bulk}}(\omega) = 1 - \frac{\omega_p^2}{\omega^2 + i\Gamma\omega} \quad (\text{A.3})$$

$$\epsilon_{\text{D}}(\omega, R) = 1 - \frac{\omega_p^2}{\omega^2 + i\Gamma(R)\omega}, \quad (\text{A.4})$$

where ω_p is the plasma frequency of the free electron gas ($\omega_p = 1.38 \times 10^{16} \text{ s}^{-1}$ for Au). The damping constant Γ is described as $\Gamma = v_F/l$ ($\Gamma = 1.07 \times 10^{14} \text{ s}^{-1}$ for Au) for the bulk metal and $\Gamma(R) = v_F(1/l + A \cdot 1/R)$ for the nanospheres smaller than electron-mean-free path. Here, v_F is the Fermi velocity ($v_F = 1.4 \times 10^6 \text{ m/s}$ for Au), l is electron-mean-free path ($l = 3.8 \times 10^{-8} \text{ m}$ for Au), R is the radius of a nanoparticle, and A is the proportionality constant ($A = 1$ for isotropic electron scattering) [160].

The absorption and scattering properties of spherical metal nanoparticles are described by the Mie theory [319]. The Mie theory provides exact analytical solution to Maxwell's equations for spheres with different diameters. The absorption and scattering features are presented by the cross-sections, C_{abs} and C_{sca} , respectively. The extinction cross-section C_{ext} is a sum of both, absorption and scattering ($C_{\text{ext}} = C_{\text{abs}} + C_{\text{sca}}$). The cross-section C of any optical event is defined as:

$$I = I_0 e^{-N \cdot C \cdot x}, \quad (\text{A.5})$$

where I_0 represents the intensity of incident light, I is the intensity of transmitted light, N is the number density of the particles, and x is the optical pass length. Basically, equation (A.5) expresses the Beer-Lambert law. According to the Mie theory, the absorption and scattering of

light originate from the oscillation of free electrons driven by the oscillating electromagnetic fields of the incident light. For large nanoparticles, the oscillations of higher orders, such as quadrupole and octapole oscillations can occur, as well as dipole mode. However, for nanoparticles significantly smaller than the wavelength of light only dipole oscillations contribute significantly to the extinction cross-section, and the Mie theory in the dipole approximation can be simplified [240, 319]. The input parameters for Mie theory calculations are as follows: the particles dielectric function $\epsilon_1 + i\epsilon_2(\omega)$, composed of real and imaginary refractive indexes, particles radius R and the permittivity of the surrounding medium ϵ_m . Thus, following relationships express the extinction and scattering cross-sections in dipole approximation:

$$C_{\text{ext}} = \frac{12\pi\omega R^3}{c_0} \frac{\epsilon_m^{3/2} \epsilon_2(\omega)}{[\epsilon_1(\omega) + 2\epsilon_m]^2 + \epsilon_2(\omega)^2} \quad (\text{A.6})$$

$$C_{\text{sca}} = \frac{128\pi^5 R^6 \epsilon_m^2}{3\lambda^4} \left[\frac{(\epsilon_1(\omega) - \epsilon_m)^2 + \epsilon_2(\omega)^2}{[\epsilon_1(\omega) + 2\epsilon_m]^2 + \epsilon_2(\omega)^2} \right] \quad (\text{A.7})$$

Here, c is the speed of light in vacuum. The resonance condition is fulfilled when $\epsilon_1(\omega) = -2\epsilon_m$ if ϵ_2 is small or weakly dependent on ω .

Shape effects are significantly pronounced in the optical absorption spectrum of Au nanoparticles. The plasmon resonance absorption band splits into two bands as the particles become more elongated along one axis. The shape of the nanorods or cylindrical nanoparticles is characterized with an aspect ratio value, which is expressed as the length (long axis) divided by the width (short axis) of a nanorod. The high-energy band absorbing at ~ 520 nm corresponds to the oscillations of free electrons perpendicular to long rod axis, and this band is relatively insensitive to the aspect ratio. The other absorption band at lower energies is caused by the oscillations of free electrons along the long axis. This band is typically red-shifted when the aspect ratio increases [240, 319].

The optical absorption spectrum of randomly oriented gold nanorods with aspect ratio K can be modeled using an extension of the Mie theory combined with the dipole approximation according to Gans [240, 319]. The extinction cross-section C_{ext} for elongated ellipsoids is given by the following equation:

$$C_{\text{ext}} = \frac{\omega}{3c} \epsilon_m^{3/2} V \sum_j \frac{(1/P_j^2) \epsilon_2(\omega)}{\{\epsilon_1(\omega) + [(1 - P_j)/P_j] \epsilon_m\}^2 + \epsilon_2(\omega)^2} \quad (\text{A.8})$$

Here, V is the volume of a nanorod and P_j are the depolarization factors along the three axes A , B and C of the nanorod with $A > B = C$. P_j are defined as:

$$P_A = \frac{1 - e^2}{e^2} \left[\frac{1}{2e} \ln \left(\frac{1 + e}{1 - e} \right) - 1 \right] \quad (\text{A.9})$$

$$P_B = P_C = \frac{1 - P_A}{2} \quad (\text{A.10})$$

and the aspect ratio K is included in e as follows:

$$e = \left[1 - \left(\frac{B}{A} \right)^2 \right]^{1/2} = \left(1 - \frac{1}{K^2} \right)^{1/2} \quad (\text{A.11})$$

In addition to strongly enhanced absorption and scattering of the nanoparticles, the excitation of the large optical polarization associated to the localized surface plasmon resonance occurs. It results in the large local electromagnetic field enhancement at the nanoparticles surface [160].

Bibliography

- [1] Guozhong Cao. *Nanostructures and nanomaterials. Synthesis, properties and applications*. Imperial College Press, London, 2004.
- [2] Günter Schmid. *Nanoparticles. From theory to applications*. Willey-VCH, Weinheim, 2004.
- [3] Masatake Haruta. Catalysis: gold rush. *Nature*, 437(7062):1098–1099, October 2005.
- [4] Albert F. Carley, David J. Morgan, Nianxue Song, M. Wyn Roberts, Stuart H. Taylor, Jonathan K. Bartley, David J. Willock, Kara L. Howard, and Graham J. Hutchings. CO bond cleavage on supported nano-gold during low temperature oxidation. *Phys. Chem. Chem. Phys.*, 13(7):2528–2538, February 2011.
- [5] Masatake Haruta. Size- and support-dependency in the catalysis of gold. *Catal. Today*, 36(1):153–166, April 1997.
- [6] Abhijit Biswas, Ilker S. Bayer, Alexandru S. Biris, Tao Wang, Enkeleda Dervishi, and Franz Faupel. Advances in top-down and bottom-up surface nanofabrication: Techniques, applications & future prospects. *Adv. Colloid Interfac.*, 170(1-2):2–27, January 2012.
- [7] Michael Faraday. The Bakerian lecture: Experimental relations of gold (and other metals) to light. *Phil. Trans. R. Soc. Lond.*, 147(January):145–181, January 1857.
- [8] Marie-Christine Daniel and Didier Astruc. Gold nanoparticles: Assembly, supramolecular chemistry, quantum-size-related properties, and applications toward biology, catalysis, and nanotechnology. *Chem. Rev.*, 104(1):293–346, January 2004.
- [9] Elvin. A. Kabat, Dan H. Moore, and Harold Landow. An electroforetic study of the protein components in cerebrospinal fluid and their relationship to the serum proteins. *J. Clin. Invest.*, 21(5):571–577, September 1942.
- [10] William L. Barnes, Alain Dereux, and Thomas W. Ebbesen. Surface plasmon subwavelength optics. *Nature*, 424(6950):824–830, August 2003.
- [11] S. A. Maier, M. L. Brongersma, P. G. Kik, S. Meltzer, A. A. G. Requicha, and H. A. Atwater. Plasmonics — a route to nanoscale optical devices. *Advanced Materials*, 13(19):1501–1505, September 2001.
- [12] Konstantin Sokolov, Michele Follen, Jesse Aaron, Ina Pavlova, Anais Malpica, Reuben Lotan, and Rebecca Richards-Kortum. Real-time vital optical imaging of precancer using anti-epidermal growth factor receptor antibodies conjugated to gold nanoparticles. *Cancer Res.*, 63(9):1999–2004, 2003.
- [13] Catherine J. Murphy, Anand M. Gole, John W. Stone, Patrick N. Sisco, Alaaldin M. Alkilany, Edie C. Goldsmith, and Sarah C. Baxter. Gold nanoparticles in biology: Beyond toxicity to cellular imaging. *Acc. Chem. Res.*, 41(12):1721–1730, December 2008.

- [14] Surbhi Lal, Susan E. Clare, and Naomi J. Halas. Nanoshell-enabled photothermal cancer therapy: impending clinical impact. *Acc. Chem. Res.*, 41(12):1842–1851, December 2008.
- [15] Xiaohua Huang, Prashant K. Jain, Ivan H. El-Sayed, and Mostafa A. El-Sayed. Plasmonic photothermal therapy (PPTT) using gold nanoparticles. *Laser Med. Sci.*, 23(3):217–228, July 2008.
- [16] Paras N. Prasad. *Introduction to Nanomedicine and Nanobioengineering*. John Wiley & Sons, Hoboken, New Jersey, 2012.
- [17] Mrinmoy De, Partha S. Ghosh, and Vincent M. Rotello. Applications of nanoparticles in biology. *Adv. Mater.*, 20(22):4225–4241, November 2008.
- [18] Elodie Boisselier and Didier Astruc. Gold nanoparticles in nanomedicine: Preparations, imaging, diagnostics, therapies and toxicity. *Chem. Soc. Rev.*, 38(6):1759–1782, June 2009.
- [19] Shuming Nie and Steven R. Emory. Probing single molecules and single nanoparticles by surface-enhanced Raman scattering. *Science*, 275(5303):1102–1106, February 1997.
- [20] Katrin Kneipp. Surface-enhanced Raman scattering. *Physics Today*, 60(11):40–46, November 2007.
- [21] Jeffrey N. Anker, W. Paige Hall, Olga Lyandres, Nilam C. Shah, Jing Zhao, and Richard P. Van Duyne. Biosensing with plasmonic nanosensors. *Nature Mater.*, 7(6):442–453, June 2008.
- [22] V. G. Kravets, F. Schedin, R. Jalil, L. Britnell, R. V. Gorbachev, D. Ansell, B. Thackray, K. S. Novoselov, A. K. Geim, Andrei V. Kabashin, and Alexander N. Grigorenko. Singular phase nano-optics in plasmonic metamaterials for label-free single-molecule detection. *Nature Mater.*, 12(4):304–309, April 2013.
- [23] Harry A. Atwater and Albert Polman. Plasmonics for improved photovoltaic devices. *Nature Mater.*, 9(3):205–213, March 2010.
- [24] Shuyan Gao, Kosei Ueno, and Hiroaki Misawa. Plasmonic antenna effects on photochemical reactions. *Acc. Chem. Res.*, 44(4):251–260, April 2011.
- [25] Vincenzo Giannini, Antonio I. Fernández-Domínguez, Susannah C. Heck, and Stefan A. Maier. Plasmonic nanoantennas: Fundamentals and their use in controlling the radiative properties of nanoemitters. *Chem. Rev.*, 111(6):3888–3912, June 2011.
- [26] Royce W. Murray. Nanoelectrochemistry: Metal nanoparticles, nanoelectrodes, and nanopores. *Chem. Rev.*, 108(7):2688–2720, July 2008.
- [27] Jonghoon Choi, Qin Zhang, Vytas Reipa, Nam Sun Wang, Melvin E. Stratmeyer, Victoria M. Hitchins, and Peter L. Goering. Comparison of cytotoxic and inflammatory responses of photoluminescent silicon nanoparticles with silicon micron-sized particles in RAW 264.7 macrophages. *J. Appl. Toxicol.*, 29(1):52–60, January 2009.
- [28] Ji-Ho Park, Luo Gu, Geoffrey von Maltzahn, Erkki Ruoslahti, Sangeeta N. Bhatia, and Michael J. Sailor. Biodegradable luminescent porous silicon nanoparticles for in vivo applications. *Nature Mater.*, 8(4):331–336, April 2009.
- [29] Norah O’Farrell, Andrew Houlton, and Benjamin R. Horrocks. Silicon nanoparticles: Applications in cell biology and medicine. *Int. J. Nanomed.*, 1(4):451–472, January 2006.

- [30] Folarin Erogbogbo, Ken-Tye Yong, Indrajit Roy, Gaixia Xu, Paras N. Prasad, and Mark T. Swihart. Biocompatible luminescent silicon quantum dots for imaging of cancer cells. *ACS Nano*, 2(5):873–878, May 2008.
- [31] Ennio Tasciotti, Xuewu Liu, Rohan Bhavane, Kevin Plant, Ashley D. Leonard, B. Katherine Price, Mark Ming-Cheng Cheng, Paolo Decuzzi, James M. Tour, Fredika Robertson, and Mauro Ferrari. Mesoporous silicon particles as a multistage delivery system for imaging and therapeutic applications. *Nature Nanotechnol.*, 3(3):151–157, March 2008.
- [32] Indrajit Roy, Tymish Y. Ohulchanskyy, Dhruba J. Bharali, Haridas E. Pudavar, Ruth A. Mistretta, Navjot Kaur, and Paras N. Prasad. Optical tracking of organically modified silica nanoparticles as DNA carriers: A nonviral, nanomedicine approach for gene delivery. *P. Natl. Acad. Sci. USA*, 102(2):279–284, January 2005.
- [33] Dmitry Kovalev, E. Gross, N. Künzner, F. Koch, Victor Yu. Timoshenko, and M. Fujii. Resonant electronic energy transfer from excitons confined in silicon nanocrystals to oxygen molecules. *Phys. Rev. Lett.*, 89(13):137401, September 2002.
- [34] Victor Yu. Timoshenko, A. A. Kudryavtsev, L. A. Osminkina, A. S. Vorontsov, Yu. V. Ryabchikov, I. A. Belogorokhov, Dmitry Kovalev, and P. K. Kashkarov. Silicon nanocrystals as photosensitizers of active oxygen for biomedical applications. *JETP Lett.*, 83(9):423–426, July 2006.
- [35] L. A. Osminkina, Maxim B. Gongalsky, A. V. Motuzuk, Victor Yu. Timoshenko, and A. A. Kudryavtsev. Silicon nanocrystals as photo- and sono-sensitizers for biomedical applications. *Appl. Phys. B*, 105(3):665–668, May 2011.
- [36] Chanseok Hong, Jungkeun Lee, Hongmei Zheng, Soon-Sun Hong, and Chongmu Lee. Porous silicon nanoparticles for cancer phototherapy. *Nanoscale Res. Lett.*, 6(1):321, January 2011.
- [37] G. Frens. Controlled nucleation for the regulation of the particle size in monodisperse gold suspensions. *Nature Phys. Sci.*, 241(105):20–22, January 1973.
- [38] J. Kimling, M. Maier, B. Okenve, Vassilios Kotaidis, H. Ballot, and Anton Plech. Turkevich method for gold nanoparticle synthesis revisited. *J. Phys. Chem. B*, 110(32):15700–15707, 2006.
- [39] Suresh K. Balasubramanian, Liming Yang, Lin-Yue L. Yung, Choon-Nam Ong, Wei-Yi Ong, and Liya E. Yu. Characterization, purification, and stability of gold nanoparticles. *Biomaterials*, 31(34):9023–9030, December 2010.
- [40] Priyabrata Mukherjee, Absar Ahmad, Deendayal Mandal, Satyajyoti Senapati, Sudhakar R. Sainkar, Mohammad I. Khan, Renu Parishcha, P. V. Ajaykumar, Mansoor Alam, Rajiv Kumar, and Murali Sastry. Fungus-mediated synthesis of silver nanoparticles and their immobilization in the mycelial matrix: A novel biological approach to nanoparticle synthesis. *Nano Lett.*, 1(10):515–519, October 2001.
- [41] Colby A. Foss, Gabor L. Hornyak, Jon A. Stockert, and Charles R. Martin. Optical properties of composite membranes containing arrays of nanoscopic gold cylinders. *J. Phys. Chem.*, 96(19):7497–7499, September 1992.
- [42] Yu-Ying, Ser-Sing Chang, Chien-Liang Lee, and C. R. Chris Wang. Gold nanorods: Electrochemical synthesis and optical properties. *J. Phys. Chem. B*, 101(34):6661–6664, August 1997.

- [43] Anand M. Gole and Catherine J. Murphy. Seed-mediated synthesis of gold nanorods: Role of the size and nature of the seed. *Chem. Mater.*, 16(19):3633–3640, September 2004.
- [44] Douglas S. English, Lindsay E. Pell, Zhonghua Yu, Paul F. Barbara, and Brian A. Korgel. Size tunable visible luminescence from individual organic monolayer stabilized silicon nanocrystal quantum dots. *Nano Lett.*, 2(7):681–685, July 2002.
- [45] Leigh T. Canham. Silicon quantum wire array fabrication by electrochemical and chemical dissolution of wafers. *Appl. Phys. Lett.*, 57(10):1046–1048, September 1990.
- [46] G. Belomoin, J. Therrien, A. Smith, S. Rao, R. Twesten, S. Chaieb, M. H. Nayfeh, L. Wagner, and L. Mitas. Observation of a magic discrete family of ultrabright Si nanoparticles. *Appl. Phys. Lett.*, 80(5):841–843, February 2002.
- [47] Svetoslav Koynov, Rui N. Pereira, Ivo Crnolatac, Dmitry Kovalev, Ann Huygens, Vladimir S. Chirvony, Martin Stutzmann, and Peter de Witte. Purification of nano-porous silicon for biomedical applications. *Adv. Eng. Mater.*, 13(6):B225–B233, June 2011.
- [48] Alaaldin M. Alkilany, Pratik K. Nagaria, Cole R. Hexel, Timothy J. Shaw, Catherine J. Murphy, and Michael D. Wyatt. Cellular uptake and cytotoxicity of gold nanorods: Molecular origin of cytotoxicity and surface effects. *Small*, 5(6):701–708, 2009.
- [49] Berislav B. Blizanac, Matthias Arenz, Philip N. Ross, and Nenad M. Marković. Surface electrochemistry of CO on reconstructed gold single crystal surfaces studied by infrared reflection absorption spectroscopy and rotating disk electrode. *J. Am. Chem. Soc.*, 126(32):10130–10141, August 2004.
- [50] P. G. Etchegoin and E. C. Le Ru. A perspective on single-molecule SERS: Current status and future challenges. *Phys. Chem. Chem. Phys.*, 10:6079–6089, 2008.
- [51] John Neddersen, George Chumanov, and Therese M. Cotton. Laser ablation of metals: A new method for preparing SERS active colloids. *Appl. Spectrosc.*, 47(12):1959–1964, 1993.
- [52] Ming-Shin Yeh, Yuh-Sheng Yang, Yi-Pei Lee, Hsiu-Fang Lee, Ya-Huey Yeh, and Chen-Sheng Yeh. Formation and characteristics of Cu colloids from CuO powder by laser irradiation in 2-propanol. *J. Phys. Chem. B*, 103(33):6851–6857, August 1999.
- [53] Fumitaka Mafuné, Jun-Ya Kohno, Yoshihiro Takeda, and Tamotsu Kondow. Formation and size control of silver nanoparticles by laser ablation in aqueous solution. *J. Phys. Chem. B*, 104(39):9111–9117, 2000.
- [54] Fumitaka Mafuné, Jun-Ya Kohno, Yoshihiro Takeda, and Tamotsu Kondow. Dissociation and aggregation of gold nanoparticles under laser irradiation. *J. Phys. Chem. B*, 105(38):9050–9056, September 2001.
- [55] A. V. Simakin, V. V. Voronov, Georgy A. Shafeev, R. Brayner, and F. Bozon-Verduraz. Nanodisks of Au and Ag produced by laser ablation in liquid environment. *Chem. Phys. Lett.*, 348(3-4):182–186, 2001.
- [56] Andrei V. Kabashin and Michel M. Meunier. Synthesis of colloidal nanoparticles during femtosecond laser ablation of gold in water. *J. Appl. Phys.*, 94(12):7941–7943, 2003.
- [57] Jean-Philippe Sylvestre, Andrei V. Kabashin, E. Sacher, and Michel M. Meunier. Femtosecond laser ablation of gold in water: Influence of the laser-produced plasma on the nanoparticle size distribution. *Appl. Phys. A*, 80(4):753–758, December 2005.

- [58] Andrei V. Kabashin, Philippe Delaporte, Antonio Pereira, David Grojo, Remi Torres, Thierry Sarnet, and Marc Sentis. Nanofabrication with pulsed lasers. *Nanoscale Res. Lett.*, 5(3):454–463, January 2010.
- [59] Vincenzo Amendola and Moreno Meneghetti. What controls the composition and the structure of nanomaterials generated by laser ablation in liquid solution? *Phys. Chem. Chem. Phys.*, 15(9):3027–3046, March 2013.
- [60] Andrei V. Kabashin and Michel M. Meunier. Femtosecond laser ablation in aqueous solutions: A novel method to synthesize non-toxic metal colloids with controllable size. *J. Phys.: Conf. Ser.*, 59:354–359, April 2007.
- [61] Jean-Philippe Sylvestre, Suzie Poulin, Andrei V. Kabashin, Edward Sacher, Michel M. Meunier, and John H. T. Luong. Surface chemistry of gold nanoparticles produced by laser ablation in aqueous media. *J. Phys. Chem. B*, 108(43):16864–16869, October 2004.
- [62] P. T. Anastas and J. C. Warner. *Green chemistry: Theory and practice*. Oxford University Press, New York, 1998.
- [63] Sébastien Besner, Andrei V. Kabashin, Françoise M. Winnik, and Michel M. Meunier. Synthesis of size-tunable polymer-protected gold nanoparticles by femtosecond laser-based ablation and seed growth. *J. Phys. Chem. C*, 113(22):9526–9531, June 2009.
- [64] Jean-Philippe Sylvestre, Andrei V. Kabashin, Edward Sacher, Michel M. Meunier, and John H. T. Luong. Stabilization and size control of gold nanoparticles during laser ablation in aqueous cyclodextrins. *J. Am. Chem. Soc.*, 126(23):7176–7177, July 2004.
- [65] Vincenzo Amendola and Moreno Meneghetti. Controlled size manipulation of free gold nanoparticles by laser irradiation and their facile bioconjugation. *J. Mater. Chem.*, 17(44):4705–4710, 2007.
- [66] Christoph Rehbock, Vivian Merk, Lisa Gamrad, René Streubel, and Stephan Barcikowski. Size control of laser-fabricated surfactant-free gold nanoparticles with highly diluted electrolytes and their subsequent bioconjugation. *Phys. Chem. Chem. Phys.*, 15(9):3057–3067, March 2013.
- [67] Csaba László Sajti, Ramin Sattari, Boris N. Chichkov, and Stephan Barcikowski. Gram scale synthesis of pure ceramic nanoparticles by laser ablation in liquid. *J. Phys. Chem. C*, 114(6):2421–2427, February 2010.
- [68] S. I. Dolgaev, A. V. Simakin, V. V. Voronov, Georgy A. Shafeev, and F. Bozon-Verduraz. Nanoparticles produced by laser ablation of solids in liquid environment. *Appl. Surf. Sci.*, 186(1-4):546–551, January 2002.
- [69] Vladimir Svrcek, Takeshi Sasaki, Yoshiki Shimizu, and Naoto Koshizaki. Blue luminescent silicon nanocrystals prepared by ns pulsed laser ablation in water. *Appl. Phys. Lett.*, 89(21):213113, November 2006.
- [70] Vladimir Svrcek, Davide Mariotti, and Michio Kondo. Ambient-stable blue luminescent silicon nanocrystals prepared by nanosecond-pulsed laser ablation in water. *Optics express*, 17(2):520–527, January 2009.
- [71] Shikuan Yang, Weiping Cai, Haibo Zeng, and Zhigang Li. Polycrystalline Si nanoparticles and their strong aging enhancement of blue photoluminescence. *J. Appl. Phys.*, 104(2):023516, July 2008.

- [72] I. Umezu, H. Minami, H. Senoo, and A. Sugimura. Synthesis of photoluminescent colloidal silicon nanoparticles by pulsed laser ablation in liquids. *J. Phys.: Conf. Ser.*, 59:392–395, April 2007.
- [73] Xiangyou Li, Alexander Pyatenko, Yoshiki Shimizu, Hongqiang Wang, Kenji Koga, and Naoto Koshizaki. Fabrication of crystalline silicon spheres by selective laser heating in liquid medium. *Langmuir*, 27(8):5076–5080, May 2011.
- [74] Kamal Abderrafi, Raúl García Calzada, Maxim B. Gongalsky, Isaac Suárez, Rafael Abarques, Vladimir S. Chirvony, Victor Yu. Timoshenko, Rafael Ibáñez, and Juan P. Martínez-Pastor. Silicon nanocrystals produced by nanosecond laser ablation in an organic liquid. *J. Phys. Chem. C*, 115(12):5147–5151, March 2011.
- [75] David Rioux, Marie Laferrière, Alexandre Douplik, Duoaud Shah, Lothar Lilge, Andrei V. Kabashin, and Michel M. Meunier. Silicon nanoparticles produced by femtosecond laser ablation in water as novel contamination-free photosensitizers. *J. Biomed. Opt.*, 14(2):021010, January 2009.
- [76] N. G. Semaltianos, S. Logothetidis, W. Perrie, S. Romani, R. J. Potter, S. P. Edwardson, P. French, M. Sharp, G. Dearden, and K. G. Watkins. Silicon nanoparticles generated by femtosecond laser ablation in a liquid environment. *J. Nanopart. Res.*, 12(2):573–580, April 2009.
- [77] Petr G. Kuzmin, Georgy A. Shafeev, Vladimir V. Bukin, Sergei V. Garnov, Cosmin Farcau, Robert Carles, Bénédicte Warot-Fontrose, Valérie Guieu, and Guillaume Viau. Silicon nanoparticles produced by femtosecond laser ablation in ethanol: Size control, structural characterization, and optical properties. *J. Phys. Chem. C*, 114(36):15266–15273, September 2010.
- [78] Romuald Intartaglia, Annette Barchanski, Komal Bagga, Alessandro Genovese, Gobind Das, Philipp Wagener, Enzo Di Fabrizio, Alberto Diaspro, Fernando Brandi, and Stephan Barcikowski. Bioconjugated silicon quantum dots from one-step green synthesis. *Nanoscale*, 4(4):1271–1274, March 2012.
- [79] Romuald Intartaglia, Komal Bagga, Fernando Brandi, Gobind Das, Alessandro Genovese, Enzo Di Fabrizio, and Alberto Diaspro. Optical properties of femtosecond laser-synthesized silicon nanoparticles in deionized water. *J. Phys. Chem. C*, 115(12):5102–5107, March 2011.
- [80] Hideaki Kurita, Akinori Takami, and Seiichiro Koda. Size reduction of gold particles in aqueous solution by pulsed laser irradiation. *Appl. Phys. Lett.*, 72(7):789–791, 1998.
- [81] Sébastien Besner, Andrei V. Kabashin, and Michel M. Meunier. Fragmentation of colloidal nanoparticles by femtosecond laser-induced supercontinuum generation. *Appl. Phys. Lett.*, 89(23):233122, 2006.
- [82] Sébastien Besner, Andrei V. Kabashin, and Michel M. Meunier. Two-step femtosecond laser ablation-based method for the synthesis of stable and ultra-pure gold nanoparticles in water. *Appl. Phys. A*, 88(2):269–272, May 2007.
- [83] Fumitaka Mafuné, Jun-Ya Kohno, Yoshihiro Takeda, and Tamotsu Kondow. Full physical preparation of size-selected gold nanoparticles in solution: Laser ablation and laser-induced size control. *J. Phys. Chem. B*, 106(34):8555–8561, August 2002.
- [84] William T. Nichols, Takeshi Sasaki, and Naoto Koshizaki. Laser ablation of a platinum target in water. III. Laser-induced reactions. *J. Appl. Phys.*, 100(11):114913, 2006.

- [85] L. Berthe, R. Fabbro, P. Peyre, and E. Bartnicki. Wavelength dependent of laser shock-wave generation in the water-confinement regime. *J. Appl. Phys.*, 85(11):7552–7555, 1999.
- [86] W. Liu, O. G. Kosareva, I. S. Golubtsov, A. Iwasaki, A. Becker, V. P. Kandidov, and S. L. Chin. Femtosecond laser pulse filamentation versus optical breakdown in H₂O. *Appl. Phys. B*, 76(3):215–229, March 2003.
- [87] V. P. Kandidov, O. G. Kosareva, I. S. Golubtsov, W. Liu, A. Becker, N. Akozbek, C. M. Bowden, and S. L. Chin. Self-transformation of a powerful femtosecond laser pulse into a white-light laser pulse in bulk optical media (or supercontinuum generation). *Appl. Phys. B*, 77(2-3):149–165, September 2003.
- [88] A. Brodeur and S. L. Chin. Ultrafast white-light continuum generation and self-focusing in transparent condensed media. *J. Opt. Soc. Am. B*, 16(4):637–650, April 1999.
- [89] William T. Nichols, Takeshi Sasaki, and Naoto Koshizaki. Laser ablation of a platinum target in water. II. Ablation rate and nanoparticle size distributions. *J. Appl. Phys.*, 100(11):114912, 2006.
- [90] P. Pronko, P. VanRompay, C. Horvath, F. Loesel, T. Juhasz, X. Liu, and G. Mourou. Avalanche ionization and dielectric breakdown in silicon with ultrafast laser pulses. *Phys. Rev. B*, 58(5):2387–2390, August 1998.
- [91] Klaus Sokolowski-Tinten, J. Bialkowski, and Dietrich von der Linde. Ultrafast laser-induced order-disorder transitions in semiconductors. *Phys. Rev. B*, 51(20):14186–14198, May 1995.
- [92] Klaus Sokolowski-Tinten and Dietrich von der Linde. Generation of dense electron-hole plasmas in silicon. *Phys. Rev. B*, 61(4):2643–2650, 2000.
- [93] S. I. Kudryashov and V. I. Emel’yanov. Band gap collapse and ultrafast “cold” melting of silicon during femtosecond laser pulses. *JETP Lett.*, 73(5):228–231, 2001.
- [94] Hatem Dachraoui and Wolfgang Husinsky. Thresholds of plasma formation in silicon identified by optimizing the ablation laser pulse form. *Phys. Rev. Lett.*, 97(10):107601, September 2006.
- [95] M. I. Kaganov, I. M. Lifshitz, and L. V. Tanatarov. Relaxation between electrons and the crystalline lattice. *Sov. Phys. JETP-USSR*, 4(2):173–178, 1957.
- [96] Sergei I. Anisimov, A. M. Bonch-Bruевич, M. A. Eliashevich, I. Imas, N. A. Pavlenko, and G. S. Romanov. Effect of powerfull light fluxes on metals (Laser radiation effect on metals, noting desintegration mechanism, indentation formation and vapor formation). *Sov. Phys. Tech. Phys.*, 11:945–962, 1967.
- [97] Stefan Nolte, C. Momma, H. Jacobs, A. Tunnermann, Boris N. Chichkov, Bernd Welleghausen, and Herbert Welling. Ablation of metals by ultrashort laser pulses. *J. Opt. Soc. Am. B*, 14(10):2716–2722, 1997.
- [98] Bernd Huttner. Optical properties under exposure to ultrashort laser pulses. *J. Phys.: Condens. Mat.*, 14(26):6689–6700, July 2002.
- [99] Changrui Cheng and Xianfan Xu. Mechanisms of decomposition of metal during femtosecond laser ablation. *Phys. Rev. B*, 72(16):165415, October 2005.
- [100] Dmitriy Ivanov and Leonid V. Zhigilei. Combined atomistic-continuum modeling of short-pulse laser melting and disintegration of metal films. *Phys. Rev. B*, 68(6):064114, August 2003.

- [101] Leonid V. Zhigilei and Dmitriy S. Ivanov. Channels of energy redistribution in short-pulse laser interactions with metal targets. *Appl. Surf. Sci.*, 248(1-4):433–439, July 2005.
- [102] E. Leveugle, Dmitriy S. Ivanov, and Leonid V. Zhigilei. Photomechanical spallation of molecular and metal targets: Molecular dynamics study. *Appl. Phys. A*, 79(7):1643–1655, June 2004.
- [103] Mikhail E. Povarnitsyn, Tatiana E. Itina, Pavel R. Levashov, and Konstantin V. Khishchenko. Mechanisms of nanoparticle formation by ultra-short laser ablation of metals in liquid environment. *Phys. Chem. Chem. Phys.*, 15(9):3108–3114, March 2013.
- [104] Mikhail E. Povarnitsyn, Tatiana E. Itina, Marc Sentis, K. Khishchenko, and P. Levashov. Material decomposition mechanisms in femtosecond laser interactions with metals. *Phys. Rev. B*, 75(23):235414, June 2007.
- [105] S.-S. Wellershoff, J. Hohlfeld, J. Güdde, and E. Matthias. The role of electron–phonon coupling in femtosecond laser damage of metals. *Appl. Phys. A*, 69(S1):S99–S107, December 1999.
- [106] Mischa Bonn, Daniel Denzler, Stephan Funk, Martin Wolf, S.-Svante Wellershoff, and Julius Hohlfeld. Ultrafast electron dynamics at metal surfaces: Competition between electron-phonon coupling and hot-electron transport. *Phys. Rev. B*, 61(2):1101–1105, January 2000.
- [107] Andrew N. Smith and Pamela M. Norris. Influence of intraband transitions on the electron thermoreflectance response of metals. *Appl. Phys. Lett.*, 78(9):1240–1242, 2001.
- [108] Pamela M. Norris, Andrew P. Caffrey, Robert J. Stevens, J. Michael Klopff, James T. McLeskey, and Andrew N. Smith. Femtosecond pump–probe nondestructive examination of materials (invited). *Rev. Sci. Instrum.*, 74(1):400–406, 2003.
- [109] Masaki Hashida, Alexandre F. Semerok, Olivier Gobert, Guillaume Petite, and J.-F. Wagner. Ablation thresholds of metals with femtosecond laser pulses. *Proc. SPIE*, 4423:178–185, June 2001.
- [110] Paul J. Antaki. Importance of nonequilibrium thermal conductivity during short-pulse laser-induced desorption from metals. *Int. J. Heat Mass Tran.*, 45(19):4063–4067, September 2002.
- [111] V. Schmidt, W. Husinsky, and G. Betz. Ultrashort laser ablation of metals: Pump-probe experiments, the role of ballistic electrons and the two-temperature model. *Appl. Surf. Sci.*, 197-198:145–155, September 2002.
- [112] Leonid V. Zhigilei. Dynamics of the plume formation and parameters of the ejected clusters in short-pulse laser ablation. *Appl. Phys. A*, 76(3):339–350, March 2003.
- [113] Tatiana E. Itina, K. Gouriet, Leonid V. Zhigilei, S. Noël, J. Hermann, and Marc Sentis. Mechanisms of small clusters production by short and ultra-short laser ablation. *Appl. Surf. Sci.*, 253(19):7656–7661, 2007.
- [114] E.G. Gamaly, A.V. Rode, B. Luther-Davies, and V.T. Tikhonchuk. Ablation of solids by femtosecond lasers: Ablation mechanism and ablation thresholds for metals and dielectrics. *Phys. Plasmas*, 9(3):949–957, 2002.
- [115] E.G. Gamaly, A.V. Rode, V.T. Tikhonchuk, and B. Luther-Davies. Electrostatic mechanism of ablation by femtosecond lasers. *Appl. Surf. Sci.*, 197-198:699–704, September 2002.

- [116] N. M. Bulgakova, R. Stoian, A. Rosenfeld, I. V. Hertel, W. Marine, and E. E. B. Campbell. A general continuum approach to describe fast electronic transport in pulsed laser irradiated materials: The problem of Coulomb explosion. *Appl. Phys. A*, 81(2):345–356, April 2005.
- [117] R. Stoian, A. Rosenfeld, D. Ashkenasi, I. V. Hertel, N. M. Bulgakova, and E. E. B. Campbell. Surface charging and impulsive ion ejection during ultrashort pulsed laser ablation. *Phys. Rev. Lett.*, 88(9):097603, March 2002.
- [118] S. Eliezer, N. Eliaz, E. Grossman, D. Fisher, I. Gouzman, Z. Henis, S. Pecker, Y. Horovitz, M. Fraenkel, S. Maman, and Y. Lereah. Synthesis of nanoparticles with femtosecond laser pulses. *Phys. Rev. B*, 69(14):144119, April 2004.
- [119] Danny Perez, Laurent Béland, Delphine Deryng, Laurent Lewis, and Michel M. Meunier. Numerical study of the thermal ablation of wet solids by ultrashort laser pulses. *Phys. Rev. B*, 77(1):014108, January 2008.
- [120] K. Eidmann, J. Meyer-ter Vehn, T. Schlegel, and S. Hüller. Hydrodynamic simulation of subpicosecond laser interaction with solid-density matter. *Phys. Rev. E*, 62(1):1202–1214, July 2000.
- [121] Antonio Miotello and Roger Kelly. Laser-induced phase explosion: New physical problems when a condensed phase approaches the thermodynamic critical temperature. *Appl. Phys. A*, 69(S1):S67–S73, December 1999.
- [122] Danny Perez and Laurent Lewis. Molecular-dynamics study of ablation of solids under femtosecond laser pulses. *Phys. Rev. B*, 67(18):184102, May 2003.
- [123] William T. Nichols, Takeshi Sasaki, and Naoto Koshizaki. Laser ablation of a platinum target in water. I. Ablation mechanisms. *J. Appl. Phys.*, 100(11):114911, 2006.
- [124] Patrick Lorazo, Laurent Lewis, and Michel M. Meunier. Thermodynamic pathways to melting, ablation, and solidification in absorbing solids under pulsed laser irradiation. *Phys. Rev. B*, 73(13):134108, April 2006.
- [125] David R. Lide. *CRC Handbook of Chemistry and Physics*. CRC Press, Boca Raton, FL, 2005.
- [126] Dwight E. Grey. *American Institute of Physics Handbook*. McGraw-Hill, New York, 1957.
- [127] A. M. Prokhorov, V. I. Konov, I. Ursu, and I. N. Mikhailescu. *Laser heating of metals*. CRC Press, Boca Raton, FL, 1990.
- [128] B. C. Stuart, M. D. Feit, S. Herman, A. M. Rubenchik, B. W. Shore, and M. D. Perry. Optical ablation by high-power short-pulse lasers. *J. Opt. Soc. Am. B*, 13(2):459–468, February 1996.
- [129] J. Bonse, S. Baudach, J. Krüger, W. Kautek, and M. Lenzner. Femtosecond laser ablation of silicon—modification thresholds and morphology. *Appl. Phys. A*, 74:19–25, February 2002.
- [130] Klaus Sokolowski-Tinten, Joerg Bialkowski, Andrea Cavalleri, Dietrich von der Linde, A. Oparin, J. Meyer-ter Vehn, and S. Anisimov. Transient states of matter during short pulse laser ablation. *Phys. Rev. Lett.*, 81(1):224–227, July 1998.
- [131] R. Fabbro, J. Fournier, P. Ballard, D. Devaux, and J. Virmont. Physical study of laser-produced plasma in confined geometry. *J. Appl. Phys.*, 68(2):775–784, 1990.

- [132] Yuji Sano, Naruhiko Mukai, Koki Okazaki, and Minoru Obata. Residual stress improvement in metal surface by underwater laser irradiation. *Nucl. Instrum. Meth. B*, 121(1-4):432–436, January 1997.
- [133] Tatiana E. Itina. On nanoparticle formation by laser ablation in liquids. *J. Phys. Chem. C*, 115(12):5044–5048, March 2011.
- [134] J. H. Yoo, S. H. Jeong, X. L. Mao, R. Greif, and R. E. Russo. Evidence for phase-explosion and generation of large particles during high power nanosecond laser ablation of silicon. *Appl. Phys. Lett.*, 76(6):783–785, 2000.
- [135] Vincenzo Amendola, Gian Andrea Rizzi, Stefano Polizzi, and Moreno Meneghetti. Synthesis of gold nanoparticles by laser ablation in toluene: Quenching and recovery of the surface plasmon absorption. *J. Phys. Chem. B*, 109(49):23125–23128, December 2005.
- [136] Shyjumon Ibrahimkutty, Philipp Wagener, Andreas Menzel, Anton Plech, and Stephan Barcikowski. Nanoparticle formation in a cavitation bubble after pulsed laser ablation in liquid studied with high time resolution small angle x-ray scattering. *Appl. Phys. Lett.*, 101(10):103104, 2012.
- [137] J. Noack and Alfred Vogel. Laser-induced plasma formation in water at nanosecond to femtosecond time scales: Calculation of thresholds, absorption coefficients, and energy density. *Quantum Electron.*, 35(8):1156–1167, 1999.
- [138] Takeshi Tsuji, D.-H. Thang, Yuuki Okazaki, Masataka Nakanishi, Yasuyuki Tsuboi, and Masaharu Tsuji. Preparation of silver nanoparticles by laser ablation in polyvinylpyrrolidone solutions. *Appl. Surf. Sci.*, 254(16):5224–5230, June 2008.
- [139] A. De Giacomo, M. Dell’Aglia, O. De Pascale, and M. Capitelli. From single pulse to double pulse ns-laser induced breakdown spectroscopy under water: Elemental analysis of aqueous solutions and submerged solid samples. *Spectrochim. Acta B*, 62(8):721–738, August 2007.
- [140] Philipp Wagener, Shyjumon Ibrahimkutty, Andreas Menzel, Anton Plech, and Stephan Barcikowski. Dynamics of silver nanoparticle formation and agglomeration inside the cavitation bubble after pulsed laser ablation in liquid. *Phys. Chem. Chem. Phys.*, 15(9):3068–3074, March 2013.
- [141] Dmitry G. Shchukin and Helmuth Möhwald. Sonochemical nanosynthesis at the engineered interface of a cavitation microbubble. *Phys. Chem. Chem. Phys.*, 8(30):3496–3506, August 2006.
- [142] Rui Zhao, Rong-qing Xu, Zhong-hua Shen, Jian Lu, and Xiao-wu Ni. Experimental investigation of the collapse of laser-generated cavitation bubbles near a solid boundary. *Opt. Laser Technol.*, 39(5):968–972, July 2007.
- [143] Philipp Wagener, Andreas Schwenke, Boris N. Chichkov, and Stephan Barcikowski. Pulsed laser ablation of zinc in tetrahydrofuran: Bypassing the cavitation bubble. *J. Phys. Chem. C*, 114(17):7618–7625, May 2010.
- [144] E. Abraham, K. Minoshima, and Hiroshige Matsumoto. Femtosecond laser-induced breakdown in water: Time-resolved shadow imaging and two-color interferometric imaging. *Opt. Commun.*, 176:441–452, 2000.
- [145] Q. Feng, J. V. Moloney, A. C. Newell, E. M. Wright, K. Cook, Paul K Kennedy, D. X. Hammer, B. A. Rockwell, and C. R. Thompson. Theory and simulation on the threshold

- of water breakdown induced by focused ultrashort laser pulses. *IEEE J. Quantum Elect.*, 33(2):127–137, 1997.
- [146] Paul K. Kennedy, Stephen A. Boppart, Daniel X. Hammer, Benjamin A. Rockwell, Gary D. Noojin, and W. P. Roach. A first-order model for computation of laser-induced breakdown thresholds in ocular and aqueous media: Part II — comparison to experiment. *IEEE J. Quantum Elect.*, 31(12):2250–2257, 1995.
- [147] D. Du, X. Liu, G. Korn, J. Squier, and G. Mourou. Laser-induced breakdown by impact ionization in SiO₂ with pulse widths from 7 ns to 150 fs. *Appl. Phys. Lett.*, 64(23):3071–3073, 1994.
- [148] Chris Schaffer, Nozomi Nishimura, Eli Glezer, Albert Kim, and Eric Mazur. Dynamics of femtosecond laser-induced breakdown in water from femtoseconds to microseconds. *Opt. Express*, 10(3):196–203, February 2002.
- [149] Alfred Vogel, J. Noack, K. Nahen, D. Theisen, S. Busch, U. Parlitz, D. X. Hammer, G. D. Noojin, B. A. Rockwell, and R. Birngruber. Energy balance of optical breakdown in water at nanosecond to femtosecond time scales. *Appl. Phys. B*, 68(2):271–280, February 1999.
- [150] A. Brodeur and S. Chin. Band-gap dependence of the ultrafast white-light continuum. *Phys. Rev. Lett.*, 80(20):4406–4409, May 1998.
- [151] Akinori Takami, Hideaki Kurita, and Seiichiro Koda. Laser-induced size reduction of noble metal particles. *J. Phys. Chem. B*, 103(8):1226–1232, February 1999.
- [152] Stephan Link, Clemens Burda, M. B. Mohamed, B. Nikoobakht, and Mostafa A. El-Sayed. Laser photothermal melting and fragmentation of gold nanorods: Energy and laser pulse-width dependence. *J. Phys. Chem. A*, 103(9):1165–1170, 1999.
- [153] Anna Giusti, Emilia Giorgetti, Simona Laza, Paolo Marsili, and Francesco Giammanco. Multiphoton fragmentation of PAMAM G5-capped gold nanoparticles induced by picosecond laser irradiation at 532 nm. *J. Phys. Chem. C*, 111(41):14984–14991, October 2007.
- [154] Alexander Pyatenko, Munehiro Yamaguchi, and Masaaki Suzuki. Mechanisms of size reduction of colloidal silver and gold nanoparticles irradiated by Nd:YAG laser. *J. Phys. Chem. C*, 113(21):9078–9085, May 2009.
- [155] Stephan Link, Clemens Burda, B. Nikoobakht, and Mostafa A. El-Sayed. Laser-induced shape changes of colloidal gold nanorods using femtosecond and nanosecond laser pulses. *J. Phys. Chem. B*, 104(26):6152–6163, July 2000.
- [156] Peter Zijlstra, James W. M. Chon, and Min Gu. White light scattering spectroscopy and electron microscopy of laser induced melting in single gold nanorods. *Phys. Chem. Chem. Phys.*, 11(28):5915–5921, July 2009.
- [157] Susumu Inasawa, Masakazu Sugiyama, and Yukio Yamaguchi. Bimodal size distribution of gold nanoparticles under picosecond laser pulses. *J. Phys. Chem. B*, 109(19):9404–9410, May 2005.
- [158] Alexander Pyatenko, Hongqiang Wang, Naoto Koshizaki, and Takeshi Tsuji. Mechanism of pulse laser interaction with colloidal nanoparticles. *Laser Photonics Rev.*, 7(4):596–604, 2013.
- [159] Daniel Werner, Shuichi Hashimoto, and Takayuki Uwada. Remarkable photothermal effect of interband excitation on nanosecond laser-induced reshaping and size reduction of pseudospherical gold nanoparticles in aqueous solution. *Langmuir*, 26(12):9956–9963, June 2010.

- [160] Shuichi Hashimoto, Daniel Werner, and Takayuki Uwada. Studies on the interaction of pulsed lasers with plasmonic gold nanoparticles toward light manipulation, heat management, and nanofabrication. *J. Photoch. Photobio. C*, 13(1):28–54, March 2012.
- [161] Fumitaka Mafuné, Jun-ya Kohno, Yoshihiro Takeda, and Tamotsu Kondow. Formation of gold nanonetworks and small gold nanoparticles by irradiation of intense pulsed laser onto gold nanoparticles. *J. Phys. Chem. B*, 107(46):12589–12596, 2003.
- [162] Prashant V. Kamat, Mark Flumiani, and Gregory V. Hartland. Picosecond dynamics of silver nanoclusters. Photoejection of electrons and fragmentation. *J. Phys. Chem. B*, 5647(98):3123–3128, 1998.
- [163] Kunihiro Yamada, Yuki Tokumoto, Takashi Nagata, and Fumitaka Mafuné. Mechanism of laser-induced size-reduction of gold nanoparticles as studied by nanosecond transient absorption spectroscopy. *J. Phys. Chem. B*, 110(24):11751–11756, June 2006.
- [164] Kunihiro Yamada, Ken Miyajima, and Fumitaka Mafuné. Thermionic emission of electrons from gold nanoparticles by nanosecond pulse-laser excitation of interband. *J. Phys. Chem. C*, 111(30):11246–11251, August 2007.
- [165] Daniel Werner and Shuichi Hashimoto. Improved working model for interpreting the excitation wavelength- and fluence-dependent response in pulsed laser-induced size reduction of aqueous gold nanoparticles. *J. Phys. Chem. C*, 115(12):5063–5072, March 2011.
- [166] Daniel Werner, Akihiro Furube, Toshihiro Okamoto, and Shuichi Hashimoto. Femtosecond laser-induced size reduction of aqueous gold nanoparticles: In situ and pump-probe spectroscopy investigations revealing Coulomb explosion. *J. Phys. Chem. C*, 115(17):8503–8512, May 2011.
- [167] Anton Plech, P. Leiderer, and J. Boneberg. Femtosecond laser near field ablation. *Laser Photonics Rev.*, 3(5):435–451, September 2009.
- [168] Anton Plech, Vassilios Kotaidis, Maciej Lorenc, and Johannes Boneberg. Femtosecond laser near-field ablation from gold nanoparticles. *Nature Phys.*, 2(1):44–47, December 2005.
- [169] Stephan Link and Mostafa A. El-Sayed. Spectroscopic determination of the melting energy of a gold nanorod. *J. Chem. Phys.*, 114(5):2362–2368, 2001.
- [170] Vassilios Kotaidis and Anton Plech. Cavitation dynamics on the nanoscale. *Appl. Phys. Lett.*, 87(21):213102, 2005.
- [171] Anton Plech, Vassilios Kotaidis, Maciej Lorenc, and M. Wulff. Thermal dynamics in laser excited metal nanoparticles. *Chem. Phys. Lett.*, 401(4-6):565–569, January 2005.
- [172] Hiroaki Fujiwara, Shozo Yanagida, and Prashant V. Kamat. Visible laser induced fusion and fragmentation of thionicotinamide-capped gold nanoparticles. *J. Phys. Chem. B*, 103(14):2589–2591, April 1999.
- [173] Chil Seong Ah, Hyouk Soo Han, Kwan Kim, and Du-Jeon Jang. Phototransformation of alkanethiol-derivatized noble metal nanoparticles. *Pure Appl. Chem.*, 72(1-2):91–99, 2000.
- [174] Zhangquan Peng, Thomas Walther, and Karl Kleinermanns. Influence of intense pulsed laser irradiation on optical and morphological properties of gold nanoparticle aggregates produced by surface acid-base reactions. *Langmuir*, 21(10):4249–4253, May 2005.
- [175] Hironobu Takahashi, Yasuro Niidome, Takuro Sato, and Sunao Yamada. Effects of capping thiols on the laser-induced fusion of gold nanoparticles and deposition onto glass substrates in cyclohexane. *Colloid. Surface. A*, 247(1-3):105–113, October 2004.

- [176] Daniel Werner, Shuichi Hashimoto, Takuro Tomita, Shigeki Matsuo, and Yoji Makita. In-situ spectroscopic measurements of laser ablation-induced splitting and agglomeration of metal nanoparticles in solution. *J. Phys. Chem. C*, 112(43):16801–16808, October 2008.
- [177] Salvador Pocoví-Martínez, Miriam Parreño Romero, Said Agouram, and Julia Pérez-Prieto. Controlled UV-C light-induced fusion of thiol-passivated gold nanoparticles. *Langmuir*, 27(9):5234–5241, May 2011.
- [178] Pierre Blandin, Ksenia A. Maximova, Maxim B. Gongalsky, Juan F. Sanchez-Royo, Vladimir S. Chirvony, Marc Sentis, Victor Yu. Timoshenko, and Andrei V. Kabashin. Femtosecond laser fragmentation from water-dispersed microcolloids: Toward fast controllable growth of ultrapure Si-based nanomaterials for biological applications. *J. Mater. Chem. B*, 1(19):2489–2495, 2013.
- [179] Leonid V. Zhigilei, Zhibin Lin, and Dmitriy S. Ivanov. Atomistic modeling of short pulse laser ablation of metals: Connections between melting, spallation, and phase explosion. *J. Phys. Chem. C*, 113(27):11892–11906, 2009.
- [180] Giuseppe Compagnini, Elena Messina, Orazio Puglisi, and Valeria Nicolosi. Laser synthesis of Au/Ag colloidal nano-alloys: Optical properties, structure and composition. *Appl. Surf. Sci.*, 254(4):1007–1011, December 2007.
- [181] Giuseppe Compagnini, Alessandro A. Scalisi, and Orazio Puglisi. Production of gold nanoparticles by laser ablation in liquid alkanes. *J. Appl. Phys.*, 94(12):7874–7877, 2003.
- [182] Vincenzo Amendola, Stefano Polizzi, and Moreno Meneghetti. Free silver nanoparticles synthesized by laser ablation in organic solvents and their easy functionalization. *Langmuir*, 23(12):6766–6770, July 2007.
- [183] Vincenzo Amendola and Moreno Meneghetti. Laser ablation synthesis in solution and size manipulation of noble metal nanoparticles. *Phys. Chem. Chem. Phys.*, 11(20):3805–3821, May 2009.
- [184] Stephan Barcikowski, Ana Menéndez-Manjón, Boris N. Chichkov, Marijus Brikas, and Gediminas Račiukaitis. Generation of nanoparticle colloids by picosecond and femtosecond laser ablations in liquid flow. *Appl. Phys. Lett.*, 91(8):083113, 2007.
- [185] Takeshi Tsuji, Kenzo Iryo, Yukio Nishimura, and Masaharu Tsuji. Preparation of metal colloids by a laser ablation technique in solution: influence of laser wavelength on the ablation efficiency (II). *J. Photoch. Photobio. A*, 145(3):201–207, December 2001.
- [186] Mushtaq A. Sobhan, Martin Ams, Michael J. Withford, and Ewa M. Goldys. Ultrafast laser ablative generation of gold nanoparticles: The influence of pulse energy, repetition frequency and spot size. *J. Nanopart. Res.*, 12(8):2831–2842, February 2010.
- [187] Fumitaka Mafuné, Jun-ya Kohno, Yoshihiro Takeda, and Tamotsu Kondow. Formation of gold nanoparticles by laser ablation in aqueous solution of surfactant. *J. Phys. Chem. B*, 105(22):5114–5120, 2001.
- [188] Boris N. Chichkov, C. Momma, Stefan Nolte, F. von Alvensleben, and A. Tunnermann. Femtosecond, picosecond and nanosecond laser ablation of solids. *Appl. Phys. A*, 63:109–115, 1996.
- [189] C. Momma, Boris N. Chichkov, Stefan Nolte, F. von Alvensleben, A. Tunnermann, Herbert Welling, and Bernd Wellegehausen. Short-pulse laser ablation of solid targets. *Opt. Commun.*, 129:134–142, 1996.

- [190] Giuseppe Compagnini, Alessandro A. Scalisi, and Orazio Puglisi. Ablation of noble metals in liquids: A method to obtain nanoparticles in a thin polymeric film. *Phys. Chem. Chem. Phys.*, 4(12):2787–2791, May 2002.
- [191] Khaled A. Elsayed, Hisham Imam, M. A. Ahmed, and Rania Ramadan. Effect of focusing conditions and laser parameters on the fabrication of gold nanoparticles via laser ablation in liquid. *Opt. Laser Technol.*, 45:495–502, February 2013.
- [192] Kuk Ki Kim, Hye Jin Kwon, Seung Keun Shin, Jae Kyu Song, and Seung-Min Park. Stability of uncapped gold nanoparticles produced by laser ablation in deionized water: The effect of post-irradiation. *Chem. Phys. Lett.*, 588:167–173, November 2013.
- [193] Hitomi Muto, Kunihiro Yamada, Ken Miyajima, and Fumitaka Mafuné. Estimation of surface oxide on surfactant-free gold nanoparticles laser-ablated in water. *J. Phys. Chem. C*, 111(46):17221–17226, November 2007.
- [194] Takeshi Tsuji, Tatsuya Yahata, Masato Yasutomo, Kazunobu Igawa, Masaharu Tsuji, Yoshie Ishikawa, and Naoto Koshizaki. Preparation and investigation of the formation mechanism of submicron-sized spherical particles of gold using laser ablation and laser irradiation in liquids. *Phys. Chem. Chem. Phys.*, 15(9):3099–3107, March 2013.
- [195] S. Amoroso, N. N. Nedyalkov, X. Wang, G. Ausanio, R. Bruzzese, and P. A. Atanasov. Ultrafast laser ablation of gold thin film targets. *J. Appl. Phys.*, 110(12):124303, 2011.
- [196] Wei Qian, Makoto Murakami, Yuki Ichikawa, and Yong Che. Highly efficient and controllable PEGylation of gold nanoparticles prepared by femtosecond laser ablation in water. *J. Phys. Chem. C*, 115(47):23293–23298, December 2011.
- [197] Ana Menéndez-Manjón, Boris N. Chichkov, and Stephan Barcikowski. Influence of water temperature on the hydrodynamic diameter of gold nanoparticles from laser ablation. *J. Phys. Chem. C*, 114(6):2499–2504, February 2010.
- [198] Vincenzo Amendola, Stefano Polizzi, and Moreno Meneghetti. Laser ablation synthesis of gold nanoparticles in organic solvents. *J. Phys. Chem. B*, 110(14):7232–7237, May 2006.
- [199] Paul Boyer and Michel M. Meunier. Modeling solvent influence on growth mechanism of nanoparticles (Au, Co) synthesized by surfactant free laser processes. *J. Phys. Chem. C*, 116(14):8014–8019, April 2012.
- [200] Emilia Giorgetti, Maurizio Muniz-Miranda, Paolo Marsili, David Scarpellini, and Francesco Giammanco. Stable gold nanoparticles obtained in pure acetone by laser ablation with different wavelengths. *J. Nanopart. Res.*, 14(1):648, January 2012.
- [201] Zijie Yan, Ruqiang Bao, Yong Huang, A. N. Caruso, Syed B. Qadri, Cerasela Zoica Dinu, and Douglas B. Chrisey. Excimer laser production, assembly, sintering, and fragmentation of novel fullerene-like permalloy particles in liquid. *J. Phys. Chem. C*, 114(9):3869–3873, March 2010.
- [202] Zijie Yan, Ruqiang Bao, Yong Huang, and Douglas B. Chrisey. Hollow particles formed on laser-induced bubbles by excimer laser ablation of Al in liquid. *J. Phys. Chem. C*, 114(26):11370–11374, July 2010.
- [203] Yuen-Yan Fong, Jason R. Gascooke, Bradley R. Visser, Gregory F. Metha, and Mark A. Buntine. Laser-based formation and properties of gold nanoparticles in aqueous solution: Formation kinetics and surfactant-modified particle size distributions. *J. Phys. Chem. C*, 114(38):15931–15940, September 2010.

- [204] Natsumi Matsuo, Hitomi Muto, Ken Miyajima, and Fumitaka Mafuné. Single laser pulse induced aggregation of gold nanoparticles. *Phys. Chem. Chem. Phys.*, 9(45):6027–6031, December 2007.
- [205] Mushtaq A. Sobhan, Michael J. Withford, and Ewa M. Goldys. Enhanced stability of gold colloids produced by femtosecond laser synthesis in aqueous solution of CTAB. *Langmuir*, 26(5):3156–3159, March 2010.
- [206] Yuen-Yan Fong, Jason R. Gascooke, Bradley R. Visser, Hugh H. Harris, Bruce C. C. Cowie, Lars Thomsen, Gregory F. Metha, and Mark A. Buntine. Influence of cationic surfactants on the formation and surface oxidation states of gold nanoparticles produced via laser ablation. *Langmuir*, 29(40):12452–12462, October 2013.
- [207] Andrei V. Kabashin, Michel M. Meunier, Christopher Kingston, and John H. T. Luong. Fabrication and characterization of gold nanoparticles by femtosecond laser ablation in an aqueous solution of cyclodextrins. *J. Phys. Chem. B*, 107(19):4527–4531, May 2003.
- [208] Emilia Giorgetti, Francesco Giammanco, Paolo Marsili, and Anna Giusti. Effect of picosecond postirradiation on colloidal suspensions of differently capped AuNPs. *J. Phys. Chem. C*, 115(12):5011–5020, March 2011.
- [209] Emilia Giorgetti, Anna Giusti, Francesco Giammanco, Paolo Marsili, and Simona Laza. Dendrimer-capped nanoparticles prepared by picosecond laser ablation in liquid environment. *Molecules*, 14(9):3731–3753, January 2009.
- [210] Johanna G. Walter, Svea Petersen, Frank Stahl, Thomas Scheper, and Stephan Barcikowski. Laser ablation-based one-step generation and bio-functionalization of gold nanoparticles conjugated with aptamers. *J. Nanobiotechnol.*, 8:21, January 2010.
- [211] Svea Petersen and Stephan Barcikowski. In situ bioconjugation: Single step approach to tailored nanoparticle-bioconjugates by ultrashort pulsed laser ablation. *Adv. Funct. Mater.*, 19(8):1167–1172, April 2009.
- [212] Svea Petersen, Annette Barchanski, Ulrike Taylor, Sabine Klein, D. Rath, and Stephan Barcikowski. Penetratin-conjugated gold nanoparticles — design of cell-penetrating nanomarkers by femtosecond laser ablation. *J. Phys. Chem. C*, 115:5152–5159, 2011.
- [213] Giuseppe Compagnini, Alessandro A. Scalisi, Orazio Puglisi, and Corrado Spinella. Synthesis of gold colloids by laser ablation in thiol-alkane solutions. *J. Mater. Res.*, 19(10):2795–2798, 2004.
- [214] Susumu Inasawa, Masakazu Sugiyama, and Yukio Yamaguchi. Laser-induced shape transformation of gold nanoparticles below the melting point: The effect of surface melting. *J. Phys. Chem. B*, 109(8):3104–3111, March 2005.
- [215] Ser-Sing Chang, Chao-Wen Shih, Cheng-Dah Chen, Wei-Cheng Lai, and C. R. Chris Wang. The shape transition of gold nanorods. *Langmuir*, 15(3):701–709, 1999.
- [216] Mitsuo Kawasaki and Kazuhisa Masuda. Laser fragmentation of water-suspended gold flakes via spherical submicroparticles to fine nanoparticles. *J. Phys. Chem. B*, 109(19):9379–9388, May 2005.
- [217] Daniel Werner and Shuichi Hashimoto. Controlling the pulsed-laser-induced size reduction of Au and Ag nanoparticles via changes in the external pressure, laser intensity, and excitation wavelength. *Langmuir*, 29(4):1295–1302, January 2013.

- [218] Jie Zheng, Caiwei Zhang, and Robert M. Dickson. Highly fluorescent, water soluble, size tunable gold quantum dots. *Phys. Rev. Lett.*, 93(7):077402, 2004.
- [219] Yu-Hung Chen, Yao-Hung Tseng, and Chen-Sheng Yeh. Laser-induced alloying Au–Pd and Ag–Pd colloidal mixtures: The formation of dispersed Au/Pd and Ag/Pd nanoparticles. *J. Mater. Chem.*, 12(5):1419–1422, April 2002.
- [220] Giuseppe Compagnini, Elena Messina, Orazio Puglisi, Rosario Sergio Cataliotti, and Valeria Nicolosi. Spectroscopic evidence of a core–shell structure in the earlier formation stages of Au–Ag nanoparticles by pulsed laser ablation in water. *Chem. Phys. Lett.*, 457(4-6):386–390, May 2008.
- [221] Jin Zhang, Jessica Worley, Stephane Dénomée, Christopher Kingston, Zygmunt J. Jakubek, Yves Deslandes, Michael Post, Benoit Simard, Nadi Braidy, and Gianluigi A. Botton. Synthesis of metal alloy nanoparticles in solution by laser irradiation of a metal powder suspension. *J. Phys. Chem. B*, 107(29):6920–6923, July 2003.
- [222] P. V. Kazakevich, A. V. Simakin, V. V. Voronov, and Georgy A. Shafeev. Laser induced synthesis of nanoparticles in liquids. *Appl. Surf. Sci.*, 252(13):4373–4380, April 2006.
- [223] David B. Pedersen, Shiliang Wang, E. J. Scott Duncan, and Septimus H. Liang. Adsorbate-induced diffusion of Ag and Au Atoms out of the cores of Ag@Au, Au@Ag, and Ag@AgI core-shell nanoparticles. *J. Phys. Chem. C*, 111(37):13665–13672, 2007.
- [224] Jin Zhang, Michael Post, Teodor Veres, Zygmunt J. Jakubek, Jingwen Guan, Dashan Wang, Francois Normandin, Yves Deslandes, and Benoit Simard. Laser-assisted synthesis of superparamagnetic Fe@Au core-shell nanoparticles. *J. Phys. Chem. B*, 110(14):7122–7128, May 2006.
- [225] Fumitaka Mafuné, Jun-Ya Kohno, Yoshihiro Takeda, and Tamotsu Kondow. Nanoscale soldering of metal nanoparticles for construction of higher-order structures. *J. Am. Chem. Soc.*, 125(7):1686–1687, February 2003.
- [226] A. Semerok, C. Chaleard, V. Detalle, J.-L. Lacour, P. Mauchien, P. Meynadier, C. Nouvelon, B. Salle, P. Palianov, M. Perdrix, and G. Petite. Experimental investigations of laser ablation efficiency of pure metals with femto, pico and nanosecond pulses. *Appl. Surf. Sci.*, 138-139:311–314, 1999.
- [227] Wolfgang Haiss, Nguyen T. K. Thanh, Jenny Aveyard, and David G. Fernig. Determination of size and concentration of gold nanoparticles from UV-vis spectra. *Anal. Chem.*, 79(11):4215–4221, July 2007.
- [228] Stephan Link and Mostafa A. El-Sayed. Size and temperature dependence of the plasmon absorption of colloidal gold nanoparticles. *J. Phys. Chem. B*, 103(21):4212–4217, May 1999.
- [229] F. A. Videla, G. A. Torchia, D. C. Schinca, L. B. Scaffardi, P. Moreno, C. Méndez, L. J. Giovanetti, J. M. Ramallo Lopez, and L. Roso. Analysis of the main optical mechanisms responsible for fragmentation of gold nanoparticles by femtosecond laser radiation. *J. Appl. Phys.*, 107(11):114308, June 2010.
- [230] Jean-Pierre Franc, Francois Avellen, Brahim Belehadji, Jean-Yves Billard, Laurence Briancon-Marjollet, Didier Frechou, Daniel H. Fruman, Ayat Karimi, Jean-Luis Kueny, and Jean-Marie Michel. *La cavitation: Mécanismes physiques et aspects industriels*. Presses Universitaire de Grenoble, Grenoble, 1995.

- [231] Bhupesh Kumar, Dheerendra Yadav, and Raj K. Thareja. Growth dynamics of nanoparticles in laser produced plasma in liquid ambient. *J. Appl. Phys.*, 110(7):074903, 2011.
- [232] B. L. V. Prasad, Savka I. Stoeva, Christopher M. Sorensen, and Kenneth J. Klabunde. Digestive-ripening agents for gold nanoparticles: Alternatives to thiols. *Chem. Mater.*, 15(4):935–942, February 2003.
- [233] Stéphane Menuel, Jean-Pierre Joly, Blandine Courcot, Josias Elysée, Nour-Eddine Ghermani, and Alain Marsura. Synthesis and inclusion ability of a bis- β -cyclodextrin pseudocryptand towards Busulfan anticancer agent. *Tetrahedron*, 63(7):1706–1714, February 2007.
- [234] Thimma R. Thatiparti, Andrew J. Shoffstall, and Horst A. von Recum. Cyclodextrin-based device coatings for affinity-based release of antibiotics. *Biomaterials*, 31(8):2335–2347, March 2010.
- [235] Erem Bilensoy, Oya Gurkaynak, Mevlut Ertan, Murat Sen, and A. Atilla Hincal. Development of nonsurfactant cyclodextrin nanoparticles loaded with anticancer drug Paclitaxel. *J. Pharmaceut. Sci.*, 97(4):1519–1529, 2008.
- [236] Chiyong Park, Hyewon Youn, Hana Kim, Taiho Noh, Yeon Hee Kook, Eun Tax Oh, Heon Joo Park, and Chulhee Kim. Cyclodextrin-covered gold nanoparticles for targeted delivery of an anti-cancer drug. *J. Mater. Chem.*, 19(16):2310–2315, 2009.
- [237] Dong Nyoungh Heo, Dae Hyeok Yang, Ho-Jin Moon, Jung Bok Lee, Min Soo Bae, Sang Cheon Lee, Won Jun Lee, In-Cheol Sun, and Il Keun Kwon. Gold nanoparticles surface-functionalized with paclitaxel drug and biotin receptor as theranostic agents for cancer therapy. *Biomaterials*, 33(3):856–866, January 2012.
- [238] Jerry L Atwood. *Comprehensive supramolecular chemistry. Volume 3 - Cyclodextrins*. Pergamon, Oxford, 1996.
- [239] S.-C. Y. Tsen, P. A. Crozier, and J. Liu. Lattice measurement and alloy compositions in metal and bimetallic nanoparticles. *Ultramicroscopy*, 98(1):63–72, December 2003.
- [240] Stephan Link and Mostafa A. El-Sayed. Shape and size dependence of radiative, non-radiative and photothermal properties of gold nanocrystals. *Int. Rev. Phys. Chem.*, 19(3):409–453, July 2000.
- [241] Young-Nam Hwang, Dae Hong Jeong, Hyun Jong Shin, Dongho Kim, Sae Chae Jeoung, Seon Hee Han, Jae-Suk Lee, and Gyoujin Cho. Femtosecond emission studies on gold nanoparticles. *J. Phys. Chem. B*, 106(31):7581–7584, August 2002.
- [242] G. Boyd, Z. Yu, and Y. Shen. Photoinduced luminescence from the noble metals and its enhancement on roughened surfaces. *Phys. Rev. B*, 33(12):7923–7936, June 1986.
- [243] Michael Ming Yu Chen and Alexander Katz. Steady-state fluorescence-based investigation of the interaction between protected thiols and gold nanoparticles. *Langmuir*, 18(6):2413–2420, March 2002.
- [244] S. Amoruso, R. Bruzzese, N. Spinelli, R. Velotta, M. Vitiello, X. Wang, G. Ausanio, V. Iannotti, and L. Lanotte. Generation of silicon nanoparticles via femtosecond laser ablation in vacuum. *Appl. Phys. Lett.*, 84(22):4502–4504, 2004.
- [245] Wladimir Marine, L. Patrone, Boris Luk'yanchuk, and Marc Sentis. Strategy of nanocluster and nanostructure synthesis by conventional pulsed laser ablation. *Appl. Surf. Sci.*, 154-155:345–352, February 2000.

- [246] L. Patrone, D. Nelson, V. I. Safarov, Marc Sentis, Wladimir Marine, and S. Giorgio. Photoluminescence of silicon nanoclusters with reduced size dispersion produced by laser ablation. *J. Appl. Phys.*, 87(8):3829–3837, 2000.
- [247] Takehito Yoshida, Shigeru Takeyama, Yuka Yamada, and Katsuhiko Mutoh. Nanometer-sized silicon crystallites prepared by excimer laser ablation in constant pressure inert gas. *Appl. Phys. Lett.*, 68(13):1772–1774, 1996.
- [248] Ken-ichi Saitow. Silicon nanoclusters selectively generated by laser ablation in supercritical fluid. *J. Phys. Chem. B*, 109(9):3731–3733, March 2005.
- [249] A. V. Simakin, V. V. Voronov, N.A. Kirichenko, and G.A. Shafeev. Nanoparticles produced by laser ablation of solids in liquid environment. *Appl. Phys. A*, 79(4-6):1127–1132, July 2004.
- [250] Shikuan Yang, Weiping Cai, Hongwen Zhang, Xiaoxia Xu, and Haibo Zeng. Size and structure control of Si nanoparticles by laser ablation in different liquid media and further centrifugation classification. *J. Phys. Chem. C*, 113(44):19091–19095, November 2009.
- [251] Shikuan Yang, Haibo Zeng, Huaping Zhao, Hongwen Zhang, and Weiping Cai. Luminescent hollow carbon shells and fullerene-like carbon spheres produced by laser ablation with toluene. *J. Mater. Chem.*, 21(12):4432–4436, 2011.
- [252] Shikuan Yang, Weiping Cai, Haibo Zeng, and Xiaoxia Xu. Ultra-fine β -SiC quantum dots fabricated by laser ablation in reactive liquid at room temperature and their violet emission. *J. Mater. Chem.*, 19(38):7119–7123, 2009.
- [253] Chih-Chia Huang, Kuei-Yi Chuang, Chin-Jie Huang, Tzu-Ming Liu, and Chen-Sheng Yeh. Graphite-shelled Si nanoparticles and their Au/Si heterodimers: Preparation, photoluminescence, and second harmonic generation. *J. Phys. Chem. C*, 115(20):9952–9960, May 2011.
- [254] Sabri Alkis, Ali K. Okyay, and Bülend Ortaç. Post-treatment of silicon nanocrystals produced by ultra-short pulsed laser ablation in liquid: Toward blue luminescent nanocrystal generation. *J. Phys. Chem. C*, 116(5):3432–3436, February 2012.
- [255] Danny Perez and Laurent Lewis. Ablation of solids under femtosecond laser pulses. *Phys. Rev. Lett.*, 89(25):255504, December 2002.
- [256] Andrea Cavalleri, Klaus Sokolowski-Tinten, Joerg Bialkowski, Michaela Schreiner, and Dietrich von der Linde. Femtosecond melting and ablation of semiconductors studied with time of flight mass spectroscopy. *J. Appl. Phys.*, 85(6):3301–3309, 1999.
- [257] Lionel Vayssieres. On the thermodynamic stability of metal oxide nanoparticles in aqueous solutions. *Int. J. Nanotechnol.*, 2(4):411–439, 2005.
- [258] Lionel Vayssieres. On the effect of nanoparticle size on water-oxide interfacial chemistry. *J. Phys. Chem. C*, 113(12):4733–4736, March 2009.
- [259] Dimitri A Sverjensky. Zero-point-of-charge prediction from crystal chemistry and solvation theory. *Geochim. Cosmochim. Ac.*, 58(14):3123–3129, 1994.
- [260] F. J. Grunthaner, P. J. Grunthaner, R. P. Vasquez, B. F. Lewis, J. Maserjian, and A. Madhukar. Local atomic and electronic structure of oxide/GaAs and SiO₂/Si interfaces using high-resolution XPS. *J. Vac. Sci. Technol.*, 16(5):1443–1453, September 1979.

- [261] Hikaru Kobayashi, Tomohiro Kubota, Hidefumi Kawa, Yoshihiro Nakato, and Masayoshi Nishiyama. Oxide thickness dependence of energy shifts in the Si 2p levels for the SiO₂/Si structure, and its elimination by a palladium overlayer. *Appl. Phys. Lett.*, 73(7):933–935, August 1998.
- [262] Seiichi Iwata and Akitoshi Ishizaka. Electron spectroscopic analysis of the SiO₂/Si system and correlation with metal–oxide–semiconductor device characteristics. *J. Appl. Phys.*, 79(9):6653–6713, May 1996.
- [263] Burak Ulgut and Sefik Suzer. XPS studies of SiO₂/Si system under external bias. *J. Phys. Chem. B*, 107(13):2939–2943, April 2003.
- [264] Chan-Cheng. Su and J. W. Faller. Application of electron spectroscopy for chemical analysis to the study of ambidentate binding in sulfoxide complexes. *Inorg. Chem.*, 13(7):1734–1736, July 1974.
- [265] B.V.R. Chowdari, K.F. Mok, J.M. Xie, and R. Gopalakrishnan. Spectroscopic and electrical studies of silver sulfophosphate glasses. *J. Non-Cryst. Solids*, 160(1-2):73–81, July 1993.
- [266] O. Renault, R. Marlier, N. T. Barrett, E. Martinez, T. Baron, M. Gely, and B. De Salvo. Modeling the XPS Si 2p core-level intensities of silicon nanocrystals for determination of oxide shell thickness. *Surf. Interface Anal.*, 38(4):486–488, April 2006.
- [267] Daria Riabinina, Christophe Durand, Mohamed Chaker, and Federico Rosei. Photoluminescent silicon nanocrystals synthesized by reactive laser ablation. *Appl. Phys. Lett.*, 88(7):073105, 2006.
- [268] Andrei V. Kabashin, Michel M. Meunier, and R. Leonelli. Photoluminescence characterization of Si-based nanostructured films produced by pulsed laser ablation. *J. Vac. Sci. Technol. B*, 19(6):2217–2222, November 2001.
- [269] Andrei V. Kabashin and Michel M. Meunier. Laser-induced treatment of silicon in air and formation of Si/SiO_x photoluminescent nanostructured layers. *Mater. Sci. Eng.: B*, 101(1-3):60–64, August 2003.
- [270] L. R. Hirsch, R. J. Stafford, J. A. Bankson, S. R. Sershen, B. Rivera, R. E. Price, J. D. Hazle, Naomi J. Halas, and J. L. West. Nanoshell-mediated near-infrared thermal therapy of tumors under magnetic resonance guidance. *P. Natl. Acad. Sci. USA*, 100(23):13549–13554, November 2003.
- [271] Ian M. White, Soroush H. Yazdi, and Wei W. Yu. Optofluidic SERS: Synergizing photonics and microfluidics for chemical and biological analysis. *Microfluid. Nanofluid.*, 13(2):205–216, March 2012.
- [272] Ximei Qian, Xiang-Hong Peng, Dominic O. Ansari, Qiqin Yin-Goen, Georgia Z. Chen, Dong M. Shin, Lily Yang, Andrew N. Young, May D. Wang, and Shuming Nie. In vivo tumor targeting and spectroscopic detection with surface-enhanced Raman nanoparticle tags. *Nature Biotechnol.*, 26(1):83–90, January 2008.
- [273] Ewan Polwart, Ruth L. Keir, Christine M. Davidson, W. Ewen Smith, and Daran A. Sadler. Novel SERS-active optical fibers prepared by the immobilization of silver colloidal particles. *Appl. Spectrosc.*, 54(4):522–527, 2000.
- [274] Peter Hildebrandt and Manfred Stockburger. Surface-enhanced resonance Raman spectroscopy of Rhodamine 6G adsorbed on colloidal silver. *J. Phys. Chem.*, 88(24):5935–5944, November 1984.

- [275] Kevin M. Cook and Gregory S. Ferguson. Relative lability of gold-oxide thin films in contact with air, solvents, or electrolyte solutions. *J. Vac. Sci. Technol. A*, 31(2):021508, 2013.
- [276] K. George Thomas and Prashant V. Kamat. Chromophore-functionalized gold nanoparticles. *Acc. Chem. Res.*, 36(12):888–898, December 2003.
- [277] Katrin Kneipp, Harald Kneipp, Ramasamy Manoharan, Eugene B. Hanlon, Irving Itzkan, Ramachandra R. Dasari, and Michael S. Feld. Extremely large enhancement factors in surface-enhanced Raman scattering for molecules on colloidal gold clusters. *Appl. Spectrosc.*, 52(12):1493–1497, 1998.
- [278] Betty Y. S. Kim, James T. Rutka, and Warren C. W. Chan. Nanomedicine. *New Engl. J. Med.*, 363(25):2434–2443, December 2010.
- [279] Kristina Riehemann, Stefan W. Schneider, Thomas A. Luger, Biana Godin, Mauro Ferrari, and Harald Fuchs. Nanomedicine — challenge and perspectives. *Angew. Chem. Int. Edit.*, 48(5):872–897, January 2009.
- [280] Dan Peer, Jeffrey M. Karp, Seungpyo Hong, Omid C. Farokhzad, Rimona Margalit, and Robert Langer. Nanocarriers as an emerging platform for cancer therapy. *Nature Nanotechnol.*, 2(12):751–760, December 2007.
- [281] Xiaohua Huang, Ivan H. El-Sayed, Wei Qian, and Mostafa A. El-Sayed. Cancer cell imaging and photothermal therapy in the near-infrared region by using gold nanorods. *J. Am. Chem. Soc.*, 128(6):2115–2120, February 2006.
- [282] André M Gobin, Min Ho Lee, Naomi J. Halas, William D. James, Rebekah A. Drezek, and Jennifer L. West. Near-infrared resonant nanoshells for combined optical imaging and photothermal cancer therapy. *Nano Lett.*, 7(7):1929–1934, July 2007.
- [283] Yiwen Wang, Xueyi Xie, Xueding Wang, Geng Ku, Kelly L. Gill, D. Patrick O’Neal, George Stoica, and Lihong V. Wang. Photoacoustic tomography of a nanoshell contrast agent in the in vivo rat brain. *Nano Lett.*, 4(9):1689–1692, September 2004.
- [284] Bengt Fadeel and Alfonso E. Garcia-Bennett. Better safe than sorry: Understanding the toxicological properties of inorganic nanoparticles manufactured for biomedical applications. *Adv. Drug Deliver. Rev.*, 62(3):362–374, March 2010.
- [285] Nikolai Khlebtsov and Lev Dykman. Biodistribution and toxicity of engineered gold nanoparticles: A review of in vitro and in vivo studies. *Chem. Soc. Rev.*, 40(3):1647–1671, March 2011.
- [286] Alaaldin M. Alkilany and Catherine J. Murphy. Toxicity and cellular uptake of gold nanoparticles: What we have learned so far? *J. Nanopart. Res.*, 12(7):2313–2333, September 2010.
- [287] Ken-ichi Ogawara, Kentaro Furumoto, Susumu Nagayama, Keiko Minato, Kazutaka Higaki, Toshiya Kai, and Toshikiro Kimura. Pre-coating with serum albumin reduces receptor-mediated hepatic disposition of polystyrene nanosphere: Implications for rational design of nanoparticles. *J. Control. Release*, 100(3):451–455, December 2004.
- [288] Jörg Kreuter, Dmitry Shamenkov, Valery Petrov, Peter Ramge, Klaus Cychutek, Claudia Koch-Brandt, and Renad Alyautdin. Apolipoprotein-mediated transport of nanoparticle-bound drugs across the blood-brain barrier. *J. Drug. Target.*, 10(4):317–325, June 2002.

- [289] Martin Schäffler, Manuela Semmler-Behnke, Hakan Sarioglu, Shinji Takenaka, Alexander Wenk, Carsten Schleh, Stefanie M. Hauck, Blair D. Johnston, and Wolfgang G. Kreyling. Serum protein identification and quantification of the corona of 5, 15 and 80 nm gold nanoparticles. *Nanotechnology*, 24(26):265103, July 2013.
- [290] Christine H. Moran, Sean M. Wainerdi, Tonya K. Cherukuri, Carter Kittrell, Benjamin J. Wiley, Nolan W. Nicholas, Steven A. Curley, John S. Kanzius, and Paul Cherukuri. Size-dependent joule heating of gold nanoparticles using capacitively coupled radiofrequency fields. *Nano Res.*, 2(5):400–405, March 2010.
- [291] Christopher J. Gannon, Paul Cherukuri, Boris I. Yakobson, Laurent Cognet, John S. Kanzius, Carter Kittrell, R. Bruce Weisman, Matteo Pasquali, Howard K. Schmidt, Richard E. Smalley, and Steven A. Curley. Carbon nanotube-enhanced thermal destruction of cancer cells in a noninvasive radiofrequency field. *Cancer*, 110(12):2654–2665, December 2007.
- [292] Leigh T. Canham. Bioactive silicon structure fabrication through nanoetching techniques. *Adv. Mater.*, 7(12):1033–1037, December 1995.
- [293] Paul Cherukuri, Evan S. Glazer, and Steven A. Curley. Targeted hyperthermia using metal nanoparticles. *Adv. Drug Deliver. Rev.*, 62(3):339–345, March 2010.
- [294] A. N. Mirza, B. D. Fornage, N. Sneige, H. M. Kuerer, L. A. Newman, F. C. Ames, and S. E. Singletary. Radiofrequency ablation of solid tumors. *Cancer J.*, 7(2):95–102, 2001.
- [295] Yulian Wu, Zhe Tang, Heqing Fang, Shunliang Gao, Jian Chen, Yong Wang, and Haichao Yan. High operative risk of cool-tip radiofrequency ablation for unresectable pancreatic head cancer. *J. Surg. Oncol.*, 94(5):392–395, October 2006.
- [296] Christopher J. Gannon and Steven A. Curley. The role of focal liver ablation in the treatment of unresectable primary and secondary malignant liver tumors. *Semin. Radiat. Oncol.*, 15(4):265–272, October 2005.
- [297] Plamen Atanassov, Chris Apblett, Scott Banta, Susan Brozik, Scott Calabrese Barton, Michael Cooney, Bor Yann Liaw, Sanjeev Mukerjee, and Shelley D. Minter. Enzymatic biofuel cells. *Interface*, 16(2):28–31, 2007.
- [298] Scott Calabrese Barton, Josh Gallaway, and Plamen Atanassov. Enzymatic biofuel cells for implantable and microscale devices. *Chem. Rev.*, 104(10):4867–4886, October 2004.
- [299] Ting Chen, Scott Calabrese Barton, Gary Binyamin, Zhiqiang Gao, Yongchao Zhang, Hyug-Han Kim, and Adam Heller. A miniature biofuel cell. *J. Am. Chem. Soc.*, 123(35):8630–8631, September 2001.
- [300] A. Habrioux, K. Servat, S. Tingry, and Boniface K. Kokoh. Enhancement of the performances of a single concentric glucose/O₂ biofuel cell by combination of bilirubin oxidase/Nafion cathode and Au–Pt anode. *Electrochem. Commun.*, 11(1):111–113, January 2009.
- [301] Seydou Hebie, Lucile Cornu, Teko W. Napporn, Julie Rousseau, and Boniface K. Kokoh. Insight on the surface structure effect of free gold nanorods on glucose electrooxidation. *J. Phys. Chem. C*, 117(19):9872–9880, May 2013.
- [302] Boniface K. Kokoh, J.-M. Léger, B. Beden, and C. Lamy. “On line” chromatographic analysis of the products resulting from the electrocatalytic oxidation of D-glucose on Pt, Au and adatoms modified Pt electrodes — Part I. Acid and neutral media. *Electrochim. Acta*, 37(8):1333–1342, June 1992.

- [303] R. R. Adzic, M. W. Hsiao, and E. B. Yeager. Electrochemical oxidation of glucose on single crystal gold surfaces. *J. Electroanal. Chem.*, 260(2):475–485, March 1989.
- [304] P. Tonda-Mikiela, T. W. Napporn, C. Morais, K. Servat, A. Chen, and Boniface K. Kokoh. Synthesis of gold-platinum nanomaterials using bromide anion exchange-synergistic electroactivity toward CO and glucose oxidation. *J. Electrochem. Soc.*, 159(11):H828–H833, August 2012.
- [305] Qianqian Li, Songzhi Cui, and Xiuling Yan. Electrocatalytic oxidation of glucose on nanoporous gold membranes. *J. Solid State Electrochem.*, 16(3):1099–1104, July 2011.
- [306] Debika Basu and Suddhasatwa Basu. Synthesis and characterization of Pt–Au/C catalyst for glucose electro-oxidation for the application in direct glucose fuel cell. *Int. J. Hydrogen Energ.*, 36(22):14923–14929, November 2011.
- [307] Margarita A. Ryashentseva. Dehydrogenating properties of supported low-percentage palladium-containing catalysts. *Russ. Chem. Rev.*, 64(10):967–983, October 1995.
- [308] Paolo Tripodi, Nicolas Armanet, Vincenzo Asarisi, Alessandro Avveduto, Alessandro Marmigi, Jenny Darja Vinko, and Jean-Paul Biberian. The effect of hydrogenation/dehydrogenation cycles on palladium physical properties. *Phys. Lett. A*, 373(35):3101–3108, August 2009.
- [309] Changwei Xu, Zhiqun Tian, Zhaochen Chen, and San Ping Jiang. Pd/C promoted by Au for 2-propanol electrooxidation in alkaline media. *Electrochem. Commun.*, 10(2):246–249, February 2008.
- [310] Changwei Xu, Pei kang Shen, and Yingliang Liu. Ethanol electrooxidation on Pt/C and Pd/C catalysts promoted with oxide. *J. Power Sources*, 164(2):527–531, February 2007.
- [311] Graham J. Hutchings and Christopher J. Kiely. Strategies for the synthesis of supported gold palladium nanoparticles with controlled morphology and composition. *Acc. Chem. Res.*, 46(8):1759–1772, August 2013.
- [312] Alexander N. Simonov, Pavel E. Plyusnin, Yury V. Shubin, Ren I. Kvon, Sergey V. Korenev, and Valentin N. Parmon. Hydrogen electrooxidation over palladium–gold alloy: Effect of pretreatment in ethylene on catalytic activity and CO tolerance. *Electrochim. Acta*, 76:344–353, August 2012.
- [313] Alexander N. Simonov, Pavel A. Pyrjaev, Boris L. Moroz, Valery I. Bukhtiyarov, and Valentin N. Parmon. Electrodispersed Pd sub-monolayers on carbon-supported Au particles of few nanometers in size: Electrocatalytic activity for hydrogen oxidation and CO tolerance vs. Pd coverage. *Electrocatal.*, 3(2):119–131, 2012.
- [314] G. Mazzone, I. Rivalta, N. Russo, and E. Sicilia. Interaction of CO with PdAu(111) and PdAu(100) bimetallic surfaces: A theoretical cluster model study. *J. Phys. Chem. C*, 112(15):6073–6081, April 2008.
- [315] Robert W. J. Scott, Chinta Sivadinarayana, Orla M. Wilson, Zhen Yan, D. Wayne Goodman, and Richard M. Crooks. Titania-supported PdAu bimetallic catalysts prepared from dendrimer-encapsulated nanoparticle precursors. *J. Am. Chem. Soc.*, 127(5):1380–1381, February 2005.
- [316] Min Tian, Monika Malig, Shuai Chen, and Aicheng Chen. Synthesis and electrochemical study of TiO₂-supported PdAu nanoparticles. *Electrochem. Commun.*, 13(4):370–373, April 2011.

-
- [317] M. Mougnot, A. Caillard, M. Simoes, S. Baranton, C. Coutanceau, and P. Brault. PdAu/C catalysts prepared by plasma sputtering for the electro-oxidation of glycerol. *Appl. Cat. B: Environ.*, 107(3-4):372–379, September 2011.
- [318] Lei Shang, Faqiong Zhao, and Baizhao Zeng. Electrodeposition of PdAu alloy nanoparticles on ionic liquid functionalized graphene film for the voltammetric determination of oxalic acid. *Electroanal.*, 25(2):453–459, February 2013.
- [319] Craig F. Bohren and Donald R. Huffman. *Absorbtion and scattering of light on small particles*. John Wiley & Sons, New York, 1983.

List of abbreviations

3MPTS	(3-mercaptopropyl)trimethoxysilane
Apo	apolipoprotein
CD	cyclodextrin
CS	chemically synthesized
CTAB	cetyltrimethylammonium bromide
CV	cyclic voltammetry
DLS	dynamic light scattering
DMSO	dimethylsulfoxide
EDS	energy-dispersive spectroscopy
FFT	fast Fourier transform
FLIM	fluorescence-lifetime imaging microscopy
FWHM	full width at half maximum
HRTEM	high resolution transmission electron microscopy
LA	laser ablation
Nd:YAG	neodymium-doped yttrium aluminum garnet
NIR	near-infrared
NP	nanoparticle
PAMAM	poly(amidoamine)
PBS	phosphate buffered saline
PEG	poly(ethylene glycol)
PL	photoluminescence
PLD	pulsed laser deposition
PSi	porous silicon
PZC	point of zero charge
RF	radio frequency
Rh6G	rhodamine 6G
RHE	reversible hydrogen electrode
SDS	sodium dodecyl sulfate
SERS	surface-enhanced Raman scattering
SPR	surface plasmon resonance
TEM	transmission electron microscopy
THF	tetrahydrofuran
UV	ultraviolet
XPS	X-ray photoelectron spectroscopy
Yb:KGW	ytterbium-doped potassium-gadolinium tungstate

Publications

The results of the current work were published in the following papers:

- o **K. Maximova**, A. Aristov, M. Sentis, A.V. Kabashin
Size-controllable synthesis of bare gold nanoparticles by femtosecond laser fragmentation in water
submitted to *Nanotechnology*
- o S. Hebié, Y. Hollande, **K. Maximova**, M. Sentis, P. Delaporte, K.B. Kokoh, T.W. Napporn, A.V. Kabashin
Bare gold nanoparticles synthesized by laser ablation in pure water as novel highly efficient electro-catalyst for biofuel cell applications
submitted to *Advanced Materials*
- o K.P. Tamarov, L.A. Osminkina, S.V. Zinovyev, **K. Maximova**, J.V. Kargina, A.P. Sviridov, M. Sentis, A.V. Ivanov, V.N. Nikiforov, A.V. Kabashin, V.Yu. Timoshenko
Radio frequency radiation-induced hyperthermia using biodegradable Si-based nanosensitizers for biomedical applications
Scientific Reports, in press
- o F. Correard, **K. Maximova**, M.-A. Estève, C. Villard, A. Al-Kattan, M. Sentis, M. Roy, M. Gingras, A.V. Kabashin, D. Braguer
Gold nanoparticles prepared by laser ablation in aqueous biocompatible solutions: Assessment of safety and biological identity for nanomedicine applications
International Journal of Nanomedicine, in press
- o P. Blandin, **K. Maximova**, M. Gongalsky, J.F. Sanchez-Royo, V.F. Chirvony, M. Sentis, V.Yu. Timoshenko, A.V. Kabashin
Femtosecond laser fragmentation from water-dispersed microcolloids: Toward fast controllable growth of ultrapure Si-based nanomaterials for biological applications
Journal of Materials Chemistry B, 1(19): 2489–2495, 2013
<http://dx.doi.org/10.1039/c3tb20285b>
- o R. Kubiliūtė, **K. Maximova**, A. Lajevardipour, J. Yong, J.S. Hartley, A.S.M. Mohsin, P. Blandin, J.W.M. Chon, M.Sentis, P.R. Stoddart, A.V. Kabashin, R. Rotomskis, A.H.A. Clayton, S. Juodkazis
Ultra-pure, water-dispersed Au nanoparticles produced by femtosecond laser ablation and fragmentation
International Journal of Nanomedicine, 8: 2601–2611, 2013
<http://dx.doi.org/10.2147/IJN.S44163>

-
- o L. Lysyakova, N. Lomadze, D. Neher, **K. Maximova**, A.V. Kabashin, S. Santer
Light controlled surface plasmon properties of gold nanoparticles
to be submitted

 - o S. Hebié, **K. Maximova**, Y. Hollande, M. Sentis, K.B. Kokoh, T.W. Napporn, A.V.
Kabashin
Tailoring of Pd-Au nanoalloys from laser ablation process: On the aspect of their activity
towards glucose electrooxidation
to be submitted

Abstract

Synthesis of novel nanomaterials for biomedical applications by ultrashort laser ablation in liquids

Inorganic nanomaterials are of a major interest for numerous applications, specifically bioimaging, biomedicine, catalysis, and also surface enhanced-Raman scattering spectroscopy. In most cases, the purity of the employed material is a key factor. Often the conventional chemical ways of synthesis cannot provide the desirable cleanliness. The aim of this thesis is to investigate and develop a laser-based synthetic concept for the fabrication of Au and Si-based nanoparticles with controlled parameters, free of surfactants and toxic by-products. The engaged approach includes two steps: 1) the generation of a raw suspension of micro- and nanoparticles by either mechanical milling or preliminary ablation of a target; 2) ultrafast laser-induced fragmentation from the suspended colloids leading to the formation of stable, non-aggregated, low-size dispersed and crystalline nanoparticles. In particular, we focus on the technique of the synthesis of bare Au nanoparticles with tunable size between 7 and 50 nm in the absence of any ligands. Moreover, this technique allows performing the *in situ* coupling of the Au nanoparticles with organic molecules and alloying at the nanoscale. Furthermore, we show the possibility of tuning the mean size and the thickness of the oxide shell of Si nanoparticles by varying the initial concentration of microparticles, the pH and the amount of dissolved oxygen. Finally, we demonstrate the optic and plasmonic properties of the nanoparticles synthesized by the techniques established in our work and their potential for the applications in catalysis and biomedicine.

Keywords: nanoparticles, femtosecond laser, laser ablation in liquids, green chemistry, biomedical applications

Résumé

Synthèse de nouveaux nanomatériaux par ablation laser ultra-brève en milieu liquide pour des applications biomédicales

De nos jours, les nanomatériaux inorganiques sont devenus des objets importants pour de nombreuses applications, particulièrement dans des domaines comme la bioimagerie, la biomédecine, la catalyse, ou encore la spectroscopie de diffusion Raman exaltée par effet de surface. La pureté du matériau employé est le facteur clé, et souvent les méthodes de synthèse chimiques ne peuvent assurer l'absence d'une contamination résiduelle. Dans ce contexte, nous avons investigué et développé la synthèse par laser de nanoparticules d'or et de silicium en contrôlant la composition et de nombreux paramètres. Exemptes d'agents tensioactifs et de sous-produits toxiques, cette technique se révèle être une approche entièrement physique de la fabrication des nanoparticules pures. L'approche engagée comprend deux étapes : 1) la génération de la suspension brute de micro- et nanoparticules par broyage mécanique, et par ablation préliminaire d'une cible solide dans un liquide ; 2) la fragmentation laser ultra-rapide de colloïdes en suspension qui aboutit à la formation de nanoparticules stables, non agrégées, cristallines et avec une faible dispersion de taille. Ce travail se concentre particulièrement sur la synthèse de nanoparticules d'or pures de taille contrôlable entre 7 et 50 nm en absence de ligands. De plus, cette technique nous permet d'obtenir des nano-alliages bimétalliques et d'effectuer un couplage *in situ* de nanoparticules d'or avec des molécules organiques. Ensuite nous montrons la possibilité d'ajuster la taille moyenne et l'épaisseur de la couche d'oxyde des nanoparticules de Si en variant la concentration des particules initiale, le pH et la quantité d'oxygène dissoutes. Enfin, nous démontrons les propriétés optiques et plasmoniques des nanoparticules synthétisées selon les techniques établies au cours de ce travail et leur potentiel pour les applications catalytiques et biomédicales.

Mots-clés : nanoparticules, laser femtoseconde, ablation en milieu liquide, chimie verte, applications biomédicales